


12-2014

Early-age hydration studies of Portland cement

Fengjuan Liu
University of Louisville

Follow this and additional works at: <https://ir.library.louisville.edu/etd>

 Part of the [Civil Engineering Commons](#), [Construction Engineering and Management Commons](#), [Other Materials Science and Engineering Commons](#), and the [Structural Materials Commons](#)

Recommended Citation

Liu, Fengjuan, "Early-age hydration studies of Portland cement" (2014). *Electronic Theses and Dissertations*. Paper 1753.
<https://doi.org/10.18297/etd/1753>

This Doctoral Dissertation is brought to you for free and open access by ThinkIR: The University of Louisville's Institutional Repository. It has been accepted for inclusion in Electronic Theses and Dissertations by an authorized administrator of ThinkIR: The University of Louisville's Institutional Repository. This title appears here courtesy of the author, who has retained all other copyrights. For more information, please contact thinkir@louisville.edu.

EARLY-AGE HYDRATION STUDIES OF PORTLAND CEMENT

By
Fengjuan Liu
B.S., Hohai University, China, 2009
M.S., Dundee University, Scotland, 2010

A Dissertation
Submitted to the Faculty of the
J.B. Speed School of Engineering of the University of Louisville
In Partial Fulfillment of the Requirements
for the Degree of

Doctor of Philosophy

Department of Civil and Environmental Engineering
University of Louisville
Louisville, Kentucky

December, 2014

Copyright 2014 by Fengjuan Liu

All rights reserved

EARLY-AGE HYDRATION STUDIES OF PORTLAND
CEMENT

By

Fengjuan Liu
B.S., Hohai University, China, 2009
M.S., Dundee University, Scotland, 2010

A Dissertation Approved on
October 27, 2014

By the following Dissertation Committee

Dr. Zihui Sun (Dissertation Director)

Dr. J.P. Mohsen

Dr. Young Hoon Kim

Dr. Mahendra Sunkara

Dr. Gamini Sumanasekera

DEDICATION

This dissertation is dedicated to my parents

Mr. Jianming Liu

and

Mrs. Yunying Shi

For their love, support, and encouragement

ACKNOWLEDGEMENTS

First of all, I would like to express my deepest gratitude to my advisor, Professor Zhihui Sun, who gave me the chance to work on this project. She guided me throughout the whole program with great patience, inspiring discussions, excellent insights, and supportive encouragement. I especially appreciate her professional training in research implementation and academic writing. Without her guidance and training, I would not obtain such a progress from my Ph.D. study.

I would also like to express my heartiest appreciation to Dr. Chengqing Qi in the CEMEX technical center. He provided XRF analysis on the compositions of all the raw materials that I used in this research, which has been very important in exploring the hydration mechanisms of these materials. In addition, his information regarding the gypsum dehydration during the cement manufacturing process is also invaluable for this project.

Special appreciations are also given to Professor Mahendra Sunkara for providing the access to Raman spectrometer and other instruments used in my research. Without his supports, the experiment work could never be conducted.

I also want to thank Professor J.P. Mohsen, Professor Young Hoon Kim, and Professor Gamini Sumanasekera for serving on my dissertation committee.

Many thanks also go to lab managers, Dr. Tatiana Krentsel and Ms. Rodica McCoy for their helps and training in thermal gravimetric analysis and scanning electron microscopy.

The staff of the department deserves my special gratitude for creating a friendly and productive work environment. I especially would like to thank Mr. Bernie Miles, and Ms. Gail Graves.

I appreciate my friends, Zhenzhen Xie, Ying Zhang, Xiaohui Zhang, Yibo Zhang, Minqi Zhu, Bin Li, Tanvir Bhuiyan, Jinyoung Hyun, Shanshan Li, Li Yang, Jeffrey Kiesel, and Jeongwon Park. Their friendships are an important part of my life in the University of Louisville.

This work has been supported by National Science Foundation (NSF) under the grant CMMI-1265983, Department of Civil and Environmental Engineering and the Graduate School Diversity Grant for Graduate Students (CODRE) at the University of Louisville. I appreciate their supports for this research.

Finally, I would like to thank my parents, Jianming Liu and Yunying Shi, and my young brother, Wenbiao Liu, for their love and support, without which I could not finish this work.

ABSTRACT

EARLY-AGE HYDRATION STUDIES OF PORTLAND CEMENT

Fengjuan Liu

October 27, 2014

Our current knowledge on cement hydration during setting is based on the discrete observation of hydrated paste. An advanced micro/nano-level technique which can perform the in-situ observation on the continuous hydration of cement paste is demanded. In this study, Raman spectroscopy (RS) was chosen as such a method to continuously investigate wet pastes. The objective of this research is to explore the hydration process and microstructural development of fresh pastes with this technique.

This research was conducted in three phases. First, the RS analysis was used to continuously observe the cement hydration from 20 minutes after mixing to 9 hours. Based on the analysis, it was found that RS was able to characterize both the cement ingredient (C_3S , C_2S , C_3A , and gypsum) and hydration products (C-S-H gel, CH, ettringite, and monosulfate). The evolution of these components during the setting period was also detected by RS. The obtained Raman signals can indicate the end of the dormant period and initial setting in the cement paste.

The RS was then expanded to study the differences in the hydration mechanisms of hardened ordinary cement paste and ultra-high performance concrete (UHPC). The silica fume included into the UHPC was found to react quickly during the first two weeks. The content changes of calcium silicates, calcium hydroxide (CH), and ettringite were different in the ordinary paste and UHPC.

In the third phase, Raman chemical mapping was implemented on the hardened cement paste to explore the microstructure developments during the hydration process. A mapping protocol was developed. The obtained maps were able to correctly reflect the distributions and connections of the different paste components. From the mapping study on the cement paste, it was found that ettringite tended to locate on the surface of calcium silicates, while CH was apt to concentrate and localize in the pores as big crystals.

TABLE OF CONTENT

ACKNOWLEDGEMENTS.....	iv
ABSTRACT.....	vi
LIST OF TABLES.....	xiv
LIST OF FIGURES.....	xv
CHAPTER 1 INTRODUCTION.....	1
1.1 Concrete Setting.....	1
1.2 Macro and Micro-level Techniques on Studying Concrete Setting.....	2
1.3 Research Significance and Objectives.....	3
1.4 Structures of This Dissertation.....	5
CHAPTER 2 HYDRATION PROCESS AND MICROSTRUCTURAL DEVELOPMENT OF PORTLAND CEMENT.....	7
2.1 Introduction.....	7
2.2 Hydration Process of Portland Cement.....	7
2.2.1 Compositions of Portland Cement.....	7
2.2.2 Chemical Reactions of Portland Cement after Mixing.....	9
2.2.3 Hydration Process and Microstructure Development.....	14

2.3 Commonly Used Micro-level Methods to Study Hydration and Microstructure of Hydrating Cement Paste.....	19
2.3.1 X-ray Diffraction (XRD).....	19
2.3.2 Infrared Spectroscopy (IR).....	22
2.3.3 Scanning Electron Microscopy (SEM).....	23
2.4 Summary	24
CHAPTER 3 RAMAN SPECTROSCOPY IN CEMENT CHEMISTRY	26
3.1 Introduction	26
3.2 Raman Scattering Theory.....	26
3.2.1 Raman Effect	26
3.2.2 Raman Shift	29
3.3 Raman Spectroscopy in Cement Chemistry.....	30
3.3.1 Characterization of Cement Clinker Phases	30
3.3.2 Characterization on Cement Hydration	31
3.3.2 Sulfate Attack and Carbonation.....	33
3.4 RS Peak Assignments.....	34
3.5 Summary	35
CHAPTER 4 SPECTRAL ANALYSIS ON THE HYDRATION PROCESS OF PORTLAND CEMENT PASTE DURING SETTING	36
4.1 Introduction	36

5.1 Background and Introduction.....	64
5.2 Materials and Sample Preparation.....	65
5.2.1 Raw Materials.....	65
5.2.2 Sample Preparation.....	67
5.3 Raman Measuring Procedures.....	68
5.4 Results and Discussion.....	69
5.4.1 Comparison between Spectra for Type I and Class H cement	69
5.4.2 Characterization of Silica Components in UHPC	70
5.4.3 Portland Cement Paste at 3-28 days	71
5.4.4 UHPC at 3-28 days.....	73
5.4.5 Quantitative Analysis of Ordinary Portland Cement Paste	74
5.4.6 Quantitative Analysis of UHPC	77
5.5 Conclusions	81
 CHAPTER 6 DEVELOPING A PROTOCOL FOR CHEMICAL MAPPING STUDY ON HARDENED PASTE.....	
6.1 Introduction	82
6.2 Raman Measuring Procedures.....	83
6.3 Chemical Mapping Methodologies	84
6.3.1 Mapping with Peak Intensity	85
6.3.2 Mapping with Peak Area	92

6.3.3 Mapping with Components Method	99
6.4 Composite Maps.....	102
6.5 Summary	103
CHAPTER 7 RAMAN CHEMICAL MAPPING STUDY ON PORTLAND CEMENT	
PASTE	105
7.1 Introduction	105
7.2 Experimental Procedures.....	106
7.2.1 Materials and Sample Preparation	106
7.2.2 Raman Chemical Mapping Configuration.....	107
7.2.3 Mapping Creation.....	108
7.3 Chemical Mapping Analysis for Cement Paste.....	109
7.3.1 Chemical Maps for Calcium Silicates	109
7.3.2 Chemical Maps for Calcium Hydroxide.....	111
7.3.3 Chemical Maps for Ettringite	114
7.3.4 Composite Maps for Cement Pastes	115
7.4 Quantitative Analysis on Cement Hydration	118
7.4.1 Quantitative analysis on Fraction Change of Calcium Silicates.....	118
7.4.2 Quantitative Analysis on Fraction Change of CH.....	121
7.5 Conclusions	124
CHAPTER 8 CONCLUSIONS AND FUTURE WORK.....	126

8.1 Conclusions	126
8.1.1 Fresh Cement Paste during Setting.....	127
8.1.2 Hydration Mechanisms of Ordinary Pastes and UHPC.....	128
8.1.3 Chemical Mapping Analysis on Pastes Microstructure.....	129
8.2 Future Work	131
REFERENCES	133
CURRICULUM VITA	147

LIST OF TABLES

Table 3.1 Characteristic Raman peaks for cement ingredients and hydration products summarized from pioneering researches	35
Table 4.1 Chemical compositions of type I Portland cement used	37
Table 4.2 Mineral compositions of type I Portland cement used.....	38
Table 4.3 Transition points and duration of the accelerating period of ettringite formation in all the cement pastes	57
Table 4.4 Summarized critical time points of setting time, heat signature, and Raman signals with unit of minute.....	59
Table 5.1 Chemical compositions of Class H cement, silica sand, silica flour, and silica fume	66
Table 5.2 Mineral compositions of Class H cement	67
Table 5.3 UHPC mix composition (Williams et al., 2009).....	68

LIST OF FIGURES

Fig. 2.1. Secondary SEM image of a porous area on a fracture surface of hydrated cement paste (Stutzman, 2001).....	10
Fig. 2.2. Secondary electron image showing the hexagonal habit of CH and needle-like habit of ettringite (Stutzman, 2001).....	11
Fig. 2.3. High resolution cryo-SEM image of cement paste hydrated for 6 minutes (Zingg et al., 2008)	12
Fig. 2.4. SEM graph of typical hexagonal crystals of monosulfate and needle-like crystals of ettringite formed by mixing calcium aluminate and calcium sulfate solutions (Mehta and Monteiro, 2005).....	13
Fig. 2.5. Rate of heat evolution during the hydration of Portland cement (Mindness et al., 2003)	18
Fig. 2.6. Development of microstructure during the hydration of Portland cement (Scrivener, 1989).....	18
Fig. 2.7. A typical XRD pattern for cement paste with a w/c ratio of 0.40 hydrated for 28 days (Trezza, 2007).....	20
Fig. 2.8. BSE imaging of hardened cement paste at 1 day (Stutzman, 2001)	23
Fig. 3.1. Raman transitional schemes	27
Fig. 3.2. Spectrum for silicon wafer used for calibration	29
Fig. 4.1. Cement powder (a) and paste (b) samples prepared for RS measurement.....	39

Fig. 4.2. Configuration of the measuring area	41
Fig. 4.3. Gained (a) and background subtracted (b) spectra from one position in the cement paste with a w/c ratio of 0.50 at the hydration age of 330 minutes.....	42
Fig. 4.4. Raman Pattern (A) for Portland cement powder and Pattern (B) for cement paste with a w/c ratio of 0.40 hydrating for 20 minutes.....	44
Fig. 4.5. Averaged spectra from the three positions at different hydrating ages in the paste with a w/c ratio of 0.50	46
Fig. 4.6. RS patterns for the pure (a) sodium hydroxide; (b) potassium hydroxide; and (c) calcium hydroxide.....	48
Fig. 4.7. Enlarged region of 1400 to 2000 cm^{-1} in the patterns of pure CH and cement paste with a w/c ratio of 0.40 at the hydration age of 20 minutes	48
Fig. 4.8. Spectra of cement paste with a w/c of 0.60 hydrated for 30 to 510 minutes	49
Fig. 4.9. Spectrum for cement paste with a w/c ratio of 0.40 at the hydration age of 180 minutes.....	51
Fig. 4.10. Spectrum for paste with a w/c ratio of 0.40 hydrated for 360 minutes	53
Fig. 4.11. Evolution of sulfate peak positions in the cement pastes during setting: (a) w/c = 0.35; (b) w/c = 0.40; (c) w/c = 0.50; and (d) w/c = 0.60	54
Fig. 4.12. Intensity changes of ettringite peak in the cement pastes with w/c ratios of: (a) 0.35; (b) 0.40; (c) 0.50; and (d) 0.60.....	56
Fig. 4.13. Vicat needle penetration curves for the cement pastes with four different w/c ratios.....	58
Fig. 4.14. Heat evolution for cement paste with a w/c ratio of 0.60 during the first 10 hours after mixing.....	59

Fig. 5.1. Raman spectra for Class H and Type I cements.....	70
Fig. 5.2. Raman spectra for silica components in UHPC: (a) silica flour; (b) silica sand; (c) silica fume.....	71
Fig. 5.3. Stacked spectra for ordinary paste with a w/c ratio of 0.60 at the hydration ages from 3 to 28 days	72
Fig. 5.4. Spectra comparison between UHPC and ordinary paste hydrated for 3 days....	73
Fig. 5.5. Stacked spectra for UHPC at the hydration ages from 3 to 28 days	74
Fig. 5.6. Evolution of peak area for calcium silicates in the ordinary paste at the hydration ages from 3 to 28 days	75
Fig. 5.7. Evolution of peak area for calcium hydroxide in the cement paste hydrated for 3 to 28 days.....	76
Fig. 5.8. Evolution of peak area for ettringite in the cement paste hydrated for 3 to 28 days	77
Fig. 5.9. Evolution of peak area for silica fume in UHPC at the hydration age from 3 to 28 days.....	78
Fig. 5.10. Evolution of peak area for calcium silicates in UHPC.....	79
Fig. 5.11. Evolution of peak area for CH in UHPC.....	79
Fig. 5.12. Evolution of peak area for ettringite in UHPC.....	80
Fig. 6.1. Mapping setup for analyzing an area on the sample surface.....	84
Fig. 6.2. Chemical map for C-S-H gel gained by mapping the intensity at 465 cm^{-1}	86
Fig. 6.3. Raman spectra gained from point (a) # 36 and (b) #52.....	87
Fig. 6.4. Spectra after normalized to the same intensity range of 0 to 6000: (a) #36; (b) #52.....	88

Fig. 6.5. Chemical map for C-S-H gel gained after the Raman data normalized to the same intensity range of 0 to 6000	88
Fig. 6.6. Spectra from point #99 in the mapped area: (a) acquired; (b) normalized to have the intensity range of 0 to 6000.....	89
Fig. 6.7. Chemical map for calcium silicates gained after the Raman data normalized to have the same integrated signal of 10000	90
Fig. 6.8. Spectra after normalized to the same integrated signal: (a) #72; (b) #58.....	90
Fig. 6.9. Chemical map for calcium silicates gained after the Raman data normalized to have the mean of 0 and variance of 1	92
Fig. 6.10. Chemical map for CH gained by mapping the peak area at the shift of 1467 to 1670 cm^{-1}	93
Fig. 6.11. Raman spectrum acquired for point #38	94
Fig. 6.12. Acquired Raman spectra from point (a) #17 and (b) #44.....	94
Fig. 6.13. Chemical maps for CH gained by mapping the peak area at the shift of 1467 to 1670 cm^{-1} after: (a) normalizing the spectra to the same intensity range; (b) normalizing the spectra to have the same integrated signal; (c) standardizing the spectra.....	95
Fig. 6.14. Acquired Raman spectrum from point #6	96
Fig. 6.15. CH chemical maps after setting threshold value for peak area: (a) Raman data normalized to the same intensity range; (b) Raman spectra normalized to the same integrated signal; (c) standardized Raman spectra.....	97
Fig. 6.16. Acquired Raman spectra from point (a) #21 and (b) #55.....	97
Fig. 6.17. Chemical map concentrated with CH.....	98
Fig. 6.18. Chemical maps for (a) C-S-H gel and (b) calcium silicates.....	99

Fig. 6.19. Reference spectrums used in mapping with the components method.....	100
Fig. 6.20. Chemical map for C-S-H gel gained by the components method on the background subtracted Raman data	101
Fig. 6.21. Chemical maps for C ₃ S and C ₂ S with the components method: (a) Raman data normalized to the same intensity range; (b) Raman spectra normalized to the same integrated signal; (c) standardized Raman spectra.....	102
Fig. 6.22. Composite maps gained from two measured areas	103
Fig. 7.1. Mapping setup for analyzing an area on the sample surface.....	107
Fig. 7.2. Chemical maps for calcium silicates in the paste with a w/c ratio of 0.35 at the hydration ages from 12 hours to 28 days	110
Fig. 7.3. Calcium silicates maps for cement pastes with four different w/c ratios at the hydration ages of (a) 12 hours and (b) 28 days.....	111
Fig. 7.4. Chemical maps for CH in the paste with a w/c ratio of 0.35 at the hydration ages from 12 hours to 28 days	112
Fig. 7.5. CH maps for cement pastes with four different w/c ratios at the hydration ages of (a) 12 hours and (b) 28 days	113
Fig. 7.6. Chemical maps for ettringite in the paste with a w/c ratio of 0.35 at the hydration ages from 12 hours to 28 days	114
Fig. 7.7. Area fraction changes of ettringite in the cement pastes with w/c ratios of: (a) 0.35; (b) 0.40; (c) 0.50; and (d) 0.60.....	115
Fig. 7.8. Composite maps for the paste with a w/c ratio of 0.35 during hydration	116
Fig. 7.9. Composite maps for the paste with a w/c ratio of 0.40 during hydration	117
Fig. 7.10. Composite maps for the paste with a w/c ratio of 0.50 during hydration	117

Fig. 7.11. Composite maps for the paste with a w/c ratio of 0.60 during hydration	117
Fig. 7.12. Schematic diagrams for the distributions and connections of the unreacted cement grains, CH, and ettringite in the paste during the hydration process.....	117
Fig. 7.13. Area fraction changes of calcium silicates in the cement pastes with w/c ratios of: (a) 0.35; (b) 0.40; (c) 0.50; and (d) 0.60.....	120
Fig. 7.14. Curves for the fraction changes of calcium silicates in the pastes with four different w/c ratios	121
Fig. 7.15. Area fraction changes of CH in the cement pastes with w/c ratios of: (a) 0.35; (b) 0.40; (c) 0.50; and (d) 0.60.....	122
Fig. 7.16. Area fraction changes of CH for the cement pastes with four different w/c ratios.....	124

CHAPTER 1

INTRODUCTION

1.1 Concrete Setting

Concrete is the most widely used construction material all over the world. In the United States alone, concrete production is a \$30 billion per year industry, considering only the value of the ready-mixed concrete sold each year (NRMCA, 2013). This amount is twice as much as the combination of steel, wood, plastics, and aluminum. With the better understanding of its properties, the concrete production is expected to increase.

Concrete is a composite materials consisting of cement, water, coarse and fine aggregates, and various mineral and chemical admixtures. During its service life, the physical, chemical, and mechanical properties of concrete undergo dramatic changes. These changes are mainly governed by the hydration process of cement paste in the concrete. Hydration is defined as the reaction between cement and water, the mixture of which is called cement paste. Paste works as a “glue” to bind aggregates together to form the concrete matrix. Upon cement mixed with water, hydration occurs and produces a variety of hydration products. With ongoing hydration, these products are able to grow, leading to the contact of each individual cement grains. During this process, cement paste

evolves from a suspension-like mixture to a solid matrix. This phenomenon is called setting.

Setting happens in the first few hours after concrete mixing. Compared to the other stages of concrete's service life, cement is more reactive and the hydration rate is much faster during the setting period. The microstructure formed during this period would lay a good foundation for concrete performance throughout its service life. In terms of the early-age properties, a proper setting can provide the concrete with sufficient consistency, cohesiveness, and initial strength for implementing the subsequent construction process. In terms of the late-age performance, proper setting will lead to a sound microstructural formation, which in turn provides concrete with desired macrostructural properties, such as strength and durability. Therefore, setting behavior of concrete plays an essential role in the life-time performance of concrete.

1.2 Macro and Micro-level Techniques on Studying Concrete Setting

Because setting is important, engineers and researchers have developed various methods to investigate setting behaviors of concrete. Among those methods, Vicat needle test and isothermal calorimetric measurement are the two most commonly used macro-level techniques. The former is often utilized to determine the initial and final setting of cement paste (Chen and Odler, 1992; Nonat et al., 1997), while the calorimetric technique is used to classify the hydration stages of paste based on the measured heat signature (Gu and Beaudoin, 1997; Snelson et al., 2008). Since these methods measure the macro-level properties during setting, i.e., mechanical property (penetration resistance)

or physical property (heat signature), the results normally indirectly reflect different aspects of hydration and microstructure evolution during the setting period. Therefore, methods that can directly detect cement hydration and microstructure development during setting are needed. Spectroscopic and imaging techniques, such as X-ray diffraction (XRD) (Scrivener et al., 2004; Korpa et al., 2009), infrared spectroscopy (IR) (Mollah et al., 2000; Ylmen et al., 2009), and scanning electron microscopy (SEM) (Scrivener, 2004; Kjellsen and Lagerblad, 2007), are commonly used by researchers to study microstructural evolution during setting. Although these methods are efficient in investigating the hydration process (IR and XRD) and microstructure (SEM) in the cement paste, all of them require sophisticated sample preparation processes. During the preparation processes, the microstructure of the cement paste can be destroyed and the samples prepared in these ways are not reusable. Therefore, our current knowledge on setting behavior is based on discrete observation. Real-time and continuous investigation of concrete microstructure during setting is needed.

1.3 Research Significance and Objectives

The microstructure of the paste matrix formed during setting period determines the strength and durability of the concrete at late age. Therefore, to obtain a concrete with good properties at both the early and late ages, an appropriate setting should be achieved. Given this background, the availability of information about cement hydration process during setting is critical. The current available techniques applied to study fresh paste require sophisticated sample preparations, which bring difficulties in continuous

investigation on real-time hydration of fresh cement paste. Thus our current knowledge on cement hydration during setting is based on discrete observation. The in-situ and continuous study of the fresh paste is missing. With these techniques, how the chemical changes influence the distributions and connections of the components in the cement paste also remains unknown. Regarding these two aspects, Raman spectroscopy (RS) is chosen to continuously observe the hydration of fresh paste during setting, and also to chemically map the paste microstructure during hydration process. RS does not require complex sample preparation, and water does not disturb the analysis of other components mixed in it. These make it a suitable method for observing wet cement paste. Combining with confocal microscopy, RS chemical mapping can reveal the relationships between the chemical and physical changes in the cement paste.

The goal of this research is to explore microstructural development of paste by in-situ observations with advanced physical and chemical methods on micro-scales. This goal is accomplished by a series of research tasks that can be divided into several stages. First, to provide solid understanding of hydration mechanism, continuous in-situ observations on real-time hydration have been carried out with RS on the cement pastes with various water to cement (w/c) ratios during the setting period. Second, RS results on hydration progress have been correlated to paste setting behaviors (setting time and hydration heat) measured with techniques on macrostructural level. This can provide theoretical supports for the occurrence of setting. Third, the chemical mapping feature of the RS system has been applied to explore the components distributions and connections in the paste microstructure. This microstructural exploration can be used to evaluate the effect of paste hydration behavior on the microstructure formation after setting.

The research activities will improve the current understanding of cement hydration mechanisms. The research can also be greatly helpful to the fundamental understanding of setting behavior, so that the construction process can be controlled. The research findings will provide cement and admixture manufacturers and researchers with information they need to improve their products and simulations. The presented research will also provide the cement industry and local and federal agencies with insights into improving current or creating new formulations of concrete and concrete admixtures.

1.4 Structures of This Dissertation

This dissertation consists of three parts. Part one provides a general introduction of the motivation and objectives of this research project (Chapter 1), and a review on the cement hydration process and microstructural development of Portland cement paste (Chapter 2). The micro-level techniques applied to study the cement hydration are also introduced in Chapter 2. Chapter 3 discusses the theoretical background and spectral analyzing procedures of RS. A detailed review of the application of RS in cement chemistry is also provided.

The second part of the dissertation consists of the application of RS spectral analysis on the hydration process of cement paste at the early age. Chapter 4 focuses on the use of the RS to continuously detect the real-time cement hydration process during setting period. The relationships between the detected Raman signals and setting time/heat evolution are also explored in this chapter. The extension of RS analysis to study the hydration process of hardened cement paste and ultra-high performance

concrete (UHPC) is elaborated in Chapter 5. The differences regarding the hydration mechanisms in the two types of materials are illustrated.

The third part of this thesis focuses on the application of RS to chemically map the paste microstructure at the early ages. Chapter 6 discusses the preliminary studies of using RS chemical mapping on the components distributions and connections in the paste matrix. The detailed results gained by chemical mapping in cement paste with various w/c ratios at different hydration ages are described in Chapter 7. Finally, conclusions and future work are given in Chapter 8.

CHAPTER 2

HYDRATION PROCESS AND MICROSTRUCTURAL DEVELOPMENT OF PORTLAND CEMENT

2.1 Introduction

Hydration of cement occurs instantly after mixing. During the hydration process, the cement particles are able to react with water to form various hydration products. With the hydration progress, the products tend to grow and connect the unreacted cement grains to form the microstructure of cement paste. The formed paste microstructure directly determines the strength and durability of concrete. In this chapter, the hydration mechanisms and microstructure evolution of Portland cement paste are reviewed.

2.2 Hydration Process of Portland Cement

2.2.1 Compositions of Portland Cement

Portland cement clinker is typically made by heating a mixture of limestone and clay to a temperature of about 1400 to 1600 °C. The main compounds in the clinker are CaO, SiO₂, Al₂O₃, and Fe₂O₃, which typically accounts for 61-67%, 19-23%, 2.5-6% and 0-6% of the clinker mass, respectively (Neville, 2010). After being processed at the high

temperature, these oxides are normally present in the form of mineral composites, which are alite ($3\text{CaO}\cdot\text{SiO}_2$, C_3S), belite ($2\text{CaO}\cdot\text{SiO}_2$, C_2S), celite ($3\text{CaO}\cdot\text{Al}_2\text{O}_3$, C_3A), and felite ($4\text{CaO}\cdot\text{Al}_2\text{O}_3\cdot\text{Fe}_2\text{O}_3$, C_4AF). These mineral phases are also called “clinker phases” in cement chemistry. The clinkers are mixed with a few amount of gypsum (1.5-4.5%) and finely ground to give Portland cement. Gypsum is added to cement to control the paste setting. Without gypsum, C_3A will react quickly with water, causing the flash set of concrete, which may prevent proper concrete mixing, transportation, and placement.

In Portland cement, C_3S and C_2S are the two major clinker phases, which take up around 60 to 80% of the total mass of cement. These two compounds will hydrate to give the main binding material that provides concrete strength. Compared to calcium silicates, C_3A and C_4AF are minor clinker phases, typically accounting for 0 to 13% and 0 to 18% of the cement, respectively. The amount of these clinker phases can be estimated by using Bogue’s equations as follows (Neville, 2010). The terms in brackets represent the percentage of the oxides in the total mass of cement.

$$C_3S = 4.07(\text{CaO}) - 7.60(\text{SiO}_2) - 6.72(\text{Al}_2\text{O}_3) - 1.43(\text{Fe}_2\text{O}_3) - 2.85(\text{SO}_3) \quad (2.1)$$

$$C_2S = 2.87(\text{SiO}_2) - 0.75(C_3S) \quad (2.2)$$

$$C_3A = 2.65(\text{Al}_2\text{O}_3) - 1.69(\text{Fe}_2\text{O}_3) \quad (2.3)$$

$$C_4AF = 3.04(\text{Fe}_2\text{O}_3) \quad (2.4)$$

The oxides compositions need to be known for using these equations, which can be obtained by X-ray fluorescence (XRF) (Lothenbach et al., 2007; Deschner et al., 2012; Garcia-mate et al., 2013), XRD (Cuberos et al., 2009; Saoût et al., 2011; Jansen et al.,

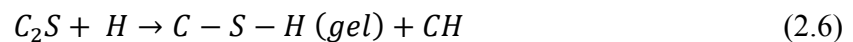
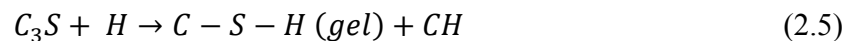
2012), and energy dispersive spectroscopy (EDS) (Kalliopi et al., 2000; Taylor et al., 2010).

2.2.2 Chemical Reactions of Portland Cement after Mixing

All the four clinker phases are able to react with water after mixing. Their reactions generate different types of hydration products that can influence the concrete properties. These reactions are illustrated as follows:

(1) Hydration of C_3S and C_2S

Both C_3S and C_2S react with water to produce calcium silicate hydrate (C-S-H gel) and calcium hydroxide (CH). The equations are shown in Eqs (2.5) and (2.6).



C-S-H gel is the principal hydration product from cement hydration and it occupies around 50 to 60% of the solid volume of the hydrated cement paste. This compound is the major binding material that gives concrete strength. It does not have a well-defined composition because of its amorphous structure. The C/S ratio varies between 1.5 and 2.0. In the fully hydrated cement paste, the average C/S ratio is normally taken as 1.7 (Richardson and Groves, 1993; Taylor et al., 2010; Myers et al., 2014). Besides its composition, the morphology of the C-S-H gel is also changing during the hydration process. In first few days, C-S-H gel is found to have acicular and honeycomb morphologies (Diamond and Lachowski, 1983; Thomas et al., 1998; Kjellsen and Justnes, 2004; Diamond and Kjellsen, 2006). After several days, small disks or spheres are

observed (Stutzman, 2001). Another type of C-S-H gel with a very dense structure is also found as the “inner” hydration product in the cement paste at late age (Kjellsen and Lagerblad, 1997). Fig. 2.1 shows an example of C-S-H gel with fine-bundles and platy morphologies observed under the SEM investigation. Other SEM images showing the various morphologies of C-S-H gel can also be found in many studies (e.g., Peethamparan et al., 2008; Gualtieri and Boccaletti, 2011).

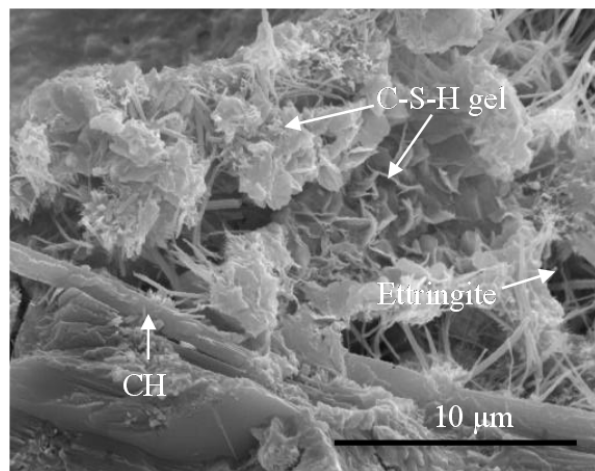


Fig. 2.1. Secondary SEM image of a porous area on a fracture surface of hydrated cement paste (Stutzman, 2001)

CH is another product formed from the calcium silicates hydration and it occupies around 20 to 25% of the solid volume in the hydrated cement paste. Different from the C-S-H gel, this hydration product is detrimental to the concrete strength because it is brittle in nature. It has definite stoichiometry and morphology and tends to crystallize in empty pores as large crystals (10 μm or larger) that exhibit hexagonal plate-like shape (Fig. 2.2). It can also be seen as elongated crystals which are the cross-sections of the hexagonal plates (Fig. 2.1).

From Eqs. (2.5) and (2.6), the hydration of C_3S and C_2S produces the same hydration products (C-S-H gel and CH). But the amounts of C-S-H gel and CH produced by C_2S are much less than C_3S due to its lower content in the Portland cement (61-67% C_3S and 19-23% C_2S). The chemical reactivity of C_3S and C_2S are also different. C_3S is more reactive and able to react with water in the first few hours after mixing. Its hydration is able to cause the paste setting and determines the early-age strength of the concrete. On the contrary, C_2S starts to hydrate at late age (normally after 7 days). Therefore, the reaction of C_2S mainly increases late-age strength.

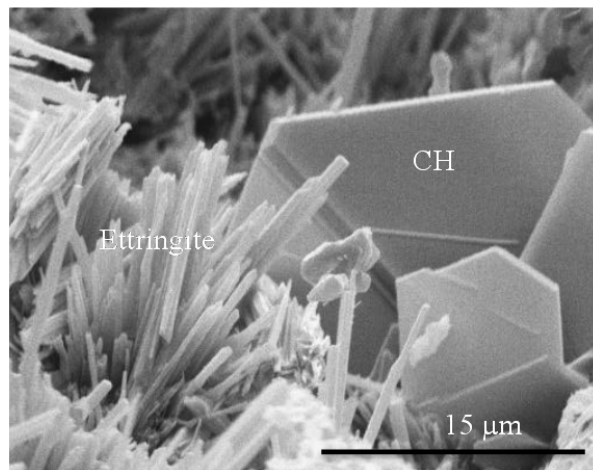
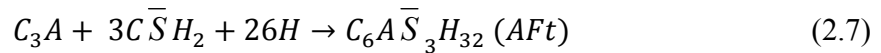


Fig. 2.2. Secondary electron image showing the hexagonal habit of CH and needle-like habit of ettringite (Stutzman, 2001)

(2) Hydration of C_3A

Besides the C_3S and C_2S , the hydration of C_3A is also important to the concrete properties. The reaction between C_3A and gypsum (shown in Eq. (2.7)) produces ettringite (AFt) in the presence of water:



This reaction starts earlier in the cement paste than the calcium silicates reactions (Eqs. (2.5) and (2.6)). As mentioned previously, gypsum is added into the cement to prevent cement flash set after mixing. The hydration product, ettringite, does not contribute significantly to the concrete strength in long term. However, the formation of ettringite influences the setting of the cement paste. This is because ettringite is formed as the needle-like structure (Figs. 2.1 and 2.2) at the early age. These needles interlock with each other, which can accelerate the setting of the cement paste. It is also found that the needle-like ettringite have different dimensions at the different hydration ages. In the first few minutes after mixing, ettringite is produced as hexagonal rods with the lateral length of 100-200 nm (Fig. 2.3). With hydration progress, the relatively slender ettringite rods are observed, typically having the size of $10 \times 0.5 \mu\text{m}$ (Figs 2.1 and 2.2).

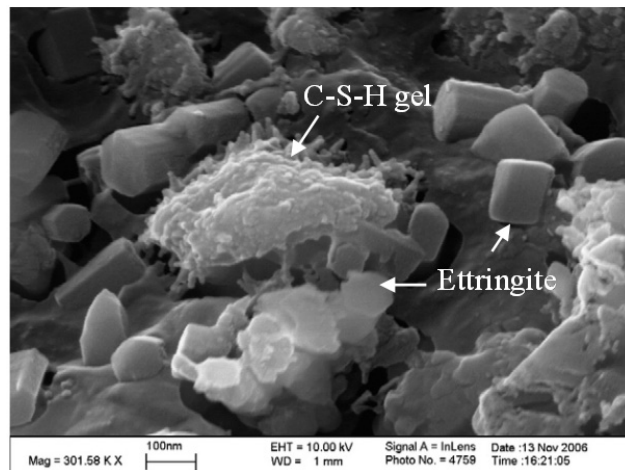
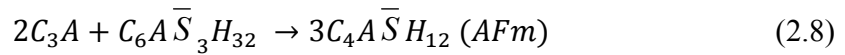


Fig. 2.3. High resolution cryo-SEM image of cement paste hydrated for 6 minutes (Zingg et al., 2008)

When gypsum depletes and C_3A remains, C_3A can react with the previously formed ettringite to generate monosulfate (AFm) (shown in Eq. (2.8)).



Monosulfate (AFm), together with ettringite, comprises 15 to 20% of the solid volume of the hydrated cement paste. Similarly to ettringite, monosulfate does not contribute much to the concrete strength. This compound is formed as hexagonal plate morphology arranged in “rosettes” during early hydration (Fig. 2.4). The well-crystallized AFm morphology shown in this figure was gained from the pure system of C_3A and gypsum. In Portland cement paste, the incorporation of other components decreases the degree of crystallinity to some extent. When hydration continues, the hexagonal plate becomes thinner and more “platy” with a typical size of $1 \times 1 \times 0.1 \mu\text{m}$.

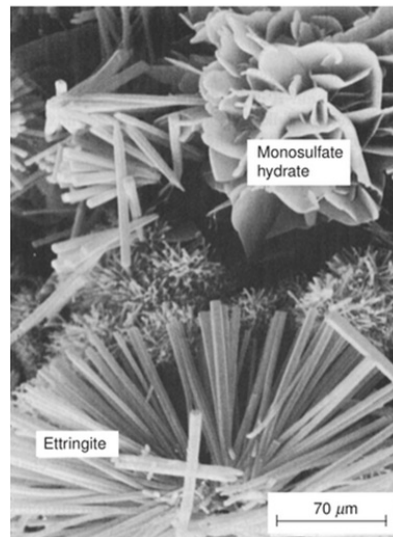
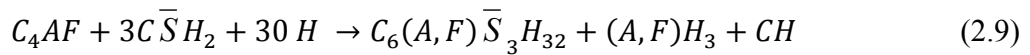


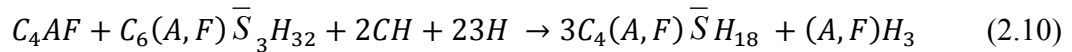
Fig. 2.4. SEM graph of typical hexagonal crystals of monosulfate and needle-like crystals of ettringite formed by mixing calcium aluminate and calcium sulfate solutions (Mehta and Monteiro, 2005)

(3) Hydration of C₄AF

The last clinker phase introduced in this section is C₄AF. It has two subsequent reactions with gypsum: firstly, it reacts with gypsum and water to form ettringite, aluminum hydroxide and calcium hydroxide:



Then, C₄AF can further react with the formed ettringite to produce garnets:



In these two equations, the use of the formulae, such as C₆(A,F) \bar{S}_3 H₃₂, indicates that iron oxide and alumina occur interchangeably in the compounds. It can be seen that C₄AF forms the similar hydration products to C₃A. But it should be pointed out that the reaction of C₄AF is much slower than C₃A and C₃S during the first few days. The quick hydration of C₃A consumes gypsum rapidly after mixing, which will retard C₄AF reaction. Therefore, most of C₄AF remains unreacted at late age (Scrivener, 2004). As a result, the influence of C₄AF on the hydration behavior of cement paste at the early ages is not as significant as C₃A and C₃S. It was not considered as an important clinker phase that contributes to cement hydration at early age.

2.2.3 Hydration Process and Microstructure Development

The hydration of cement is an exothermic reaction, therefore, observations of the heat released from hydration can help researcher to explore undergoing chemical reactions in the cement paste at the different hydration ages. These chemical reactions

produce various hydration products with different morphologies. With the hydration progress, these products can grow and bring the individual cement grains to connect with each other, forming the microstructure of the paste matrix. The formed microstructure determines the concrete strength and durability. In this section, the chemical reactions and microstructure evolution in the cement paste at the different hydration stages defined from heat signature are briefly reviewed.

A typical heat evolution against hydration age curve gained from the calorimetric method is shown in Fig. 2.5 (Mindness et al., 2003). According to this figure, four hydration stages can be characterized. The first stage is called *rapid heat evolution stage*. It starts right after mixing and lasts for less than 15 minutes. During this stage, the reactive hydration of C_3A is dominant in the cement paste. The surface of cement particles is covered with amorphous, aluminate-rich gel. Short AFt rods (100 to 200 nm, Fig. 2.3) nucleate at the edge of the gel and in the pore solutions, which is schematically shown in Fig. 2.6. This figure is a schematic diagram showing microstructural development of cement paste at different ages, on which the microstructure illustration in this section is largely based. The formed gel layer on the cement particle surface is thought to prevent the contact between cement ingredients and water, slowing down the cement hydration (Bullard et al., 2011). At this point, cement paste goes into another stage, called *dormant period*. This stage lasts one or two hours during which cement paste is workable. During the whole stage, the reaction rate of cement paste is very low. The main phenomenon happening in the cement paste is the nucleation and growth of C-S-H gel and CH nucleates (Bullard et al., 2011). These nucleates will initiate the hydration of C_3S for the next hydration stage. Researchers typically correlate the end of

dormant period to the initial setting of the cement paste. The term, initial setting, refers to the beginning of the paste solidification, marking the point in time when the paste has become inflowable.

The dormant period is followed by the *accelerating stage* (stage III in Fig. 2.5), during which the quick reaction of C_3S begins and dominates the paste hydration. This stage can last for up to 10 hours, but sometimes as short as 4 hours. Nucleates formed from the dormant period provide the sites for the precipitation of C-S-H gel and CH. The C-S-H gel produced in this stage is called “outer products”, which precipitates on the previously formed AFt rods network from stage I (Fig. 2.6(c)). “Outer” means that the C-S-H gel is not formed on the surface of the reacting cement particles. Instead, the gel precipitates at the distance which is $\sim 1 \mu\text{m}$ away from the particles surface. As a result, there is no C-S-H gel filled between the grain surface and the hydrated shell (Hadley et al., 2000; Scrivener, 2004; Kjellsen and Lagerblad, 2007). The followed cement hydration can happen in two directions, inward and outward the shell. “Outer” C-S-H gel has the acicular and honeycomb morphologies. Another product from C_3S hydration, CH, tends to precipitate in the pores with the hexagonal plate-like shape (Fig. 2.2). These pores are previously occupied by the pore solutions which participate in cement reactions and are consumed.

The continuous C_3S hydration produces the first peak in the heat evolution at the end of the *accelerating stage*. In the meantime, the growth of C-S-H gel and CH during this stage brings the individual cement grains to connect with each other. Therefore, the achievement of the first peak in Fig. 2.5 is taken by the researchers as an indication of the

final setting in the cement paste, which hints the complete solidification of the cement paste.

Following the final setting of the cement paste, the rate of hydration slows down over a long period, which is called *deceleration stage*, shown as stage IV in Fig. 2.5. This stage lasts till the end of the concrete service life. Although the hydration rate of cement paste is very slow, but cement hydration continues during the whole stage. At this stage, secondary hydration of C_3A starts, producing long rods ettringite (Fig. 2.6(d)). With the increased hydration age, with most, but not all, cements, there is a renewed increase in the rate of hydration up to a second, lower peak at the age of 18 and 30 hours. This peak is related to the reaction of C_3A with ettringite inside shell with the depletion of gypsum, forming monosulfate (Fig. 2.6(e)).

In this stage, the reaction of C_3S also continues and “inner” C-S-H gel starts to form on the inside of hydrated shell (Fig 2.6(f)). Continuing formation of “inner” C-S-H gel from C_3S reaction reduces the separation of the anhydrous grains and hydrated shell. At the late age of the hydration (~ 14 days), sufficient “inner” C-S-H gel has formed to fill in the space between grain and shell, while “outer” C-S-H gel has become more fibrous (Rodger and Groves, 1989; Taylor, 1997; Richardson, 1999). During this stage, CH is still apt to precipitate in the capillary pores and crystalize as big hexagonal plate (10 μm or larger, Fig. 2.2).

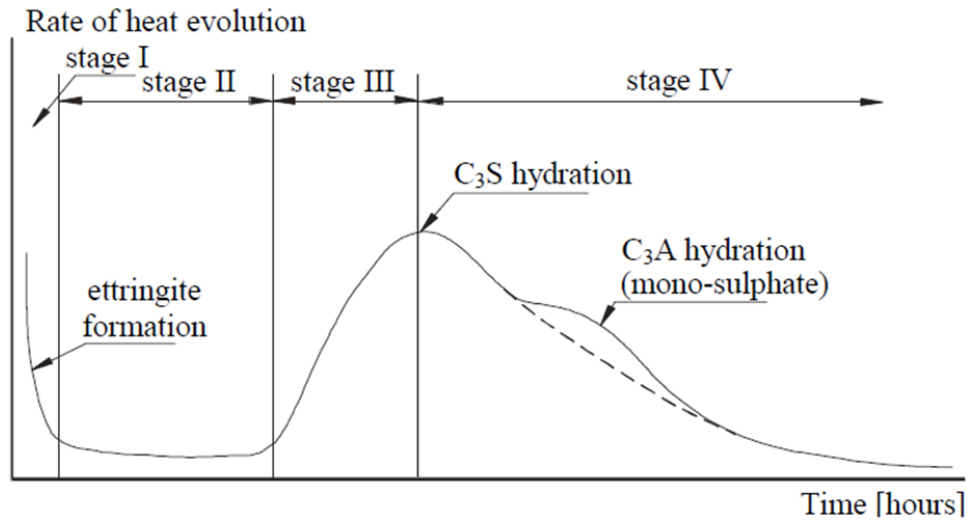


Fig. 2.5. Rate of heat evolution during the hydration of Portland cement (Mindness et al., 2003)

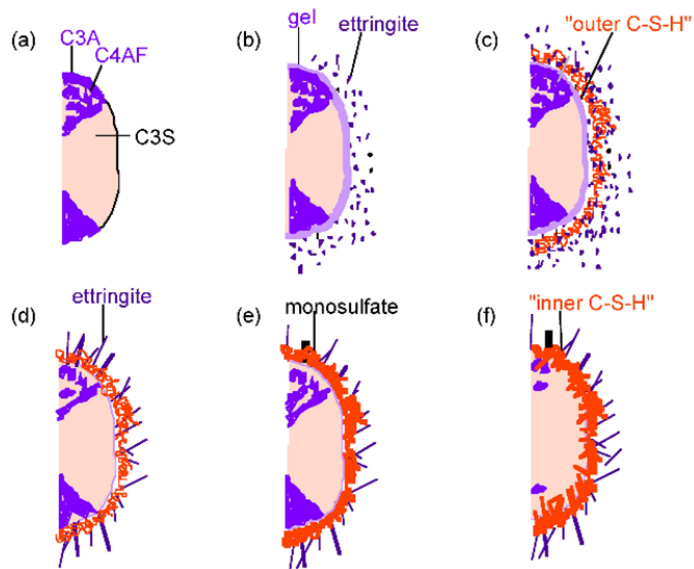


Fig. 2.6. Development of microstructure during the hydration of Portland cement (Scrivener, 1989)

2.3 Commonly Used Micro-level Methods to Study Hydration and Microstructure of Hydrating Cement Paste

Due to the importance of hydration process and microstructure development at the early age, many micro-level techniques have been applied to study the hydration mechanisms and microstructure development of cement paste, including XRD, IR, SEM, etc. XRD and IR are typically used to study the chemical reactions during the hydration process, while SEM is applied to identify the morphologies, distributions, and connections of paste components. In the following discussions, the detailed application and main findings of these microscopic and spectroscopic methods in studying cement hydration are illustrated.

2.3.1 X-ray Diffraction (XRD)

XRD is a powerful technique for characterizing crystalline materials in cement paste, including both the anhydrous clinker phases (C_3S , C_2S , C_3A , C_4AF , and other minor crystalline phases) and the main hydration products (mainly CH and ettringite) (Scrivener et al., 2004; Snellings et al., 2014), because the XRD pattern of each crystalline material is unique (Fig. 2.7).

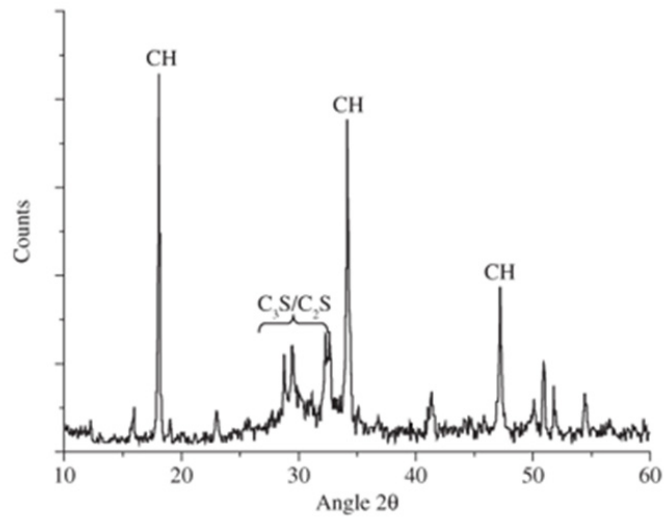
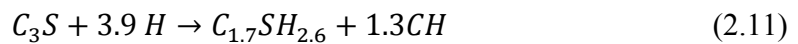


Fig. 2.7. A typical XRD pattern for cement paste with a w/c ratio of 0.40 hydrated for 28 days (Trezza, 2007)

XRD powder studies on cement paste have been reported by many investigators (Taylor, 1997; Hill and Sharp, 2002; Mechling et al., 2009; Kim et al., 2014). Gypsum phases are usually no longer detectable after 24 hours, and the clinker phases are consumed at different rates, C_3S and C_3A reacting more quickly than C_2S and C_4AF . The ratio of C_2S to C_3S thus increases steadily, and after about 90 days, little or no C_3S or C_3A is normally detected.

In ordinary Portland cement paste at room temperature ($\sim 23\text{ }^\circ\text{C}$), ettringite peaks are detectable in the XRD pattern within a few hours and increase in the intensity to a maximum often at 1 day. Peaks of AFm phase usually appear within 24 hours, but are sometimes only observed after some days or even months. With the conversion of ettringite into monosulfate (Eq. (2.8)), the ettringite peak is weakened after about 24 hours and may ultimately disappear, while peaks of monosulfate gradually become stronger.

By applying the Rietveld refinement (Rietveld, 1969), XRD analysis is also able to provide the quantitative determination of the phase compositions in the hydrating paste. This method is extremely useful for studying the hydration of calcium silicates, which can only be marked by CH detection in the XRD pattern. This is due to the amorphous structure of C-S-H gel, which is normally undetectable by XRD. In most cases, the content of C-S-H gel is calculated from the formation of CH in accordance with the following equation, assuming that the C/S ratio is 1.7 in the hydrated cement paste.



XRD is helpful for studying the chemical evolution in cement paste. But it requires sophisticated sample preparation. Firstly, the hydration of cement paste needs to be stopped by submerging the specimen into acetone or ethanol solutions. Thereafter, the sample is dried overnight in an oven to evaporate the remaining solutions. The dried sample needs further to be ground into powder. These sample preparation processes are time-consuming, and more importantly, the samples prepared in these ways are not reusable. Thus the continuous observation on the same sample is not possible. Recent developments in the XRD analysis make the in-situ observation of cement hydration possible, with either Kapton film (Hesse et al., 2007) or synchrotron radiation (Merlini and Artioli, 2007). However, as stated by Hesse et al. (2007), the overlapped XRD peaks were hard to be distinguished from each other in the paste by using Kapton film, and the synchrotron radiation is seldom used due to its expense.

2.3.2 Infrared Spectroscopy (IR)

IR has been used in the cement paste study for a long time. Similarly to XRD, IR measurements are also focused on the chemical analysis of the compounds in the cement paste. But different from XRD, IR can be used to study both crystalline and amorphous materials.

By using IR, the content of the various anhydrous cement phases in cement can be semi-quantitatively determined (Ghosh and Handoo, 1980; Hughes et al., 1995). The hydration progress of cement clinker phases can be tracked by comparing the peaks positions and intensities at the various hydration ages. Researchers found the reactive sulfates chemistry in the first 30 minutes after mixing (Ylmen et al., 2009). They postulated that the sulfates formed are most probably ettringite or monosulfate. They also pointed out that setting was due to the coalescence of cement grains, in which C-S-H gel worked as the binder.

One main drawback of the IR technique is that water displays strong absorption in the mid-IR range, which makes it virtually impossible to perform in-situ studies on cement hydration. For the ex-situ use of IR to study the very early hydration, this technique requires similar sample preparation to that in the XRD analysis. The hydration of the paste needs to be stopped, followed by being dried in an oven and then being ground into powder.

2.3.3 Scanning Electron Microscopy (SEM)

Different from XRD and IR focusing on analyzing the chemical changes of cement paste during the hydration process, SEM is used to investigate the paste microstructure. This technique can be used in two modes, secondary (SE) and backscattered (BSE). Secondary SEM is an efficient tool to distinguish the morphologies of hydration products (Figs. 2.1-2.4), while with the backscattered SEM images, the distributions and connections of the unreacted cement grains and hydration products can be found.

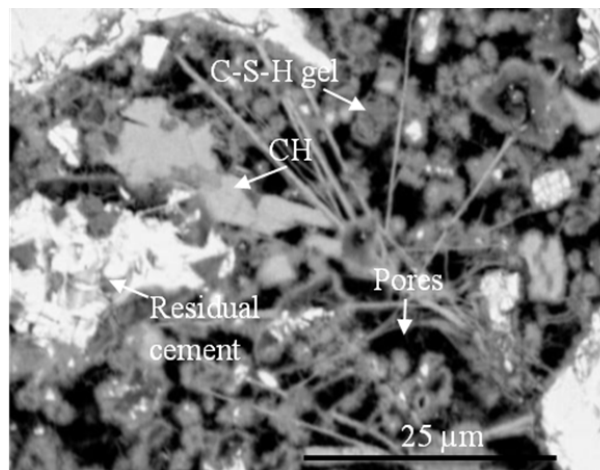


Fig. 2.8. BSE imaging of hardened cement paste at 1 day (Stutzman, 2001)

The morphologies of the main hydration products, including C-S-H gel, CH, ettringite, and monosulfate under the secondary SEM observation have been elaborated in Figs. 2.1 to 2.4 and are not repeated here. Fig. 2.8 depicts a typical SEM image for the hydrated cement paste under the BSE mode. The different contrast observed is corresponding to the average atomic number of each individual component. The higher the average atomic number, the brighter the component will be displayed in the image.

The brightest area in this figure is noted for the unreacted cement grains, mainly consisting of C_2S and C_4AF , which are unreactive at the early age hydration. Calcium hydroxide is observed as areas darker than the unreacted clinker phases but brighter than the other hydration products. It is followed by C-S-H gel, whose gray level is higher than ettringite/monosulfate and pores.

For the paste to be used in SEM, delicate sample preparations are also required. The hydration of the specimen needs to be stopped at the designated ages and then dried overnight in an oven. After this the sample should be fractured or impregnated with resin and polished for the observation under secondary or backscattered mode, respectively. Recent developments in the SEM analysis reduce the requirements for sample preparation with either Quantomix capsule (Katz et al., 2006; Venkateela and Sun, 2010) or cryo-SEM (Zingg et al., 2008). The capsule method allows an in-situ observation of the particle growth during setting. However, the detailed morphologies of the different hydration products cannot be seen. In cryo-SEM, the hydration of fresh cement paste is rapidly arrested with high pressure freezing by nitrogen. The frozen sample can only be used once. Therefore, a continuous observation on the same sample cannot be achieved with this technique as well.

2.4 Summary

Cement hydration is a complicated process, involving both chemical reactions and microstructure development. The hydration behavior of cement paste at the early age is important to both the early-age and long-term properties of concrete during its service life.

This has already revoked many micro-level techniques to be applied to directly explore the cement reactions and microstructure evolution during the hydration process. The commonly used methods, XRD, IR, and SEM, are efficient tools in investigating these two aspects. But they all require sophisticated sample preparations, which can destroy the vulnerable paste microstructure and also bring difficulties in in-situ observation on the fresh cement paste. Therefore, there is a demand for a new advanced technique with simple sample preparation process which can continuously observe the real-time hydration of fresh paste.

In the current work, Raman spectroscopy is chosen as such a technique to explore the continuous, real-time cement hydration during the setting period. This technique is also used to chemically map the components distributions and connections in the cement paste at the early age. This can provide the simultaneous measurements on the chemical and physical developments of the paste microstructure with the hydration progress.

CHAPTER 3

RAMAN SPECTROSCOPY IN CEMENT CHEMISTRY

3.1 Introduction

In this chapter, a general description of the theoretical basis of Raman spectroscopy (RS) is discussed. Following this, a detailed review about the application of RS in cement chemistry including its utilization in characterizing clinker phases, exploring hydration process, and detecting deteriorated concrete, will also be given,

3.2 Raman Scattering Theory

3.2.1 Raman Effect

RS is a spectroscopic technique used to study vibrational, rotational, and other low-frequency modes in a system (Gardiner, 1989). In a RS system, sample is usually illuminated with a laser from the visible, near infrared, or near ultraviolet range. If the molecule in the sample is considered to be in an electric field E determined by its polarizability α , and the laser is assumed to be an oscillating electromagnetic wave with electrical vector E . Upon interaction with the sample, the laser induces electric dipole moment $P = \alpha E$, which deforms molecules. Because of periodical deformation by the

laser, molecules start to vibrate with characteristic frequency ν_m (Princeton Instruments, 2012). In other words, laser with frequency ν_0 excites molecules and transforms them into oscillating dipoles. Such oscillating dipoles emit light of three different frequencies (Fig. 3.1) when:

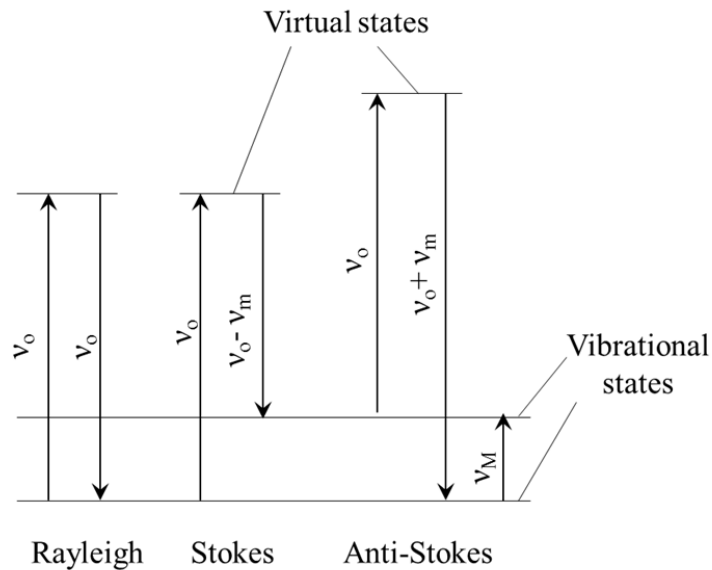


Fig. 3.1. Raman transitional schemes

- A photon with frequency ν_0 is absorbed by a molecule with no Raman-active modes. The excited molecule returns back to the same basic vibrational state and emits light with the same frequency ν_0 as the excitation source. This type of interaction is called *Rayleigh scattering*.
- A Raman-active molecule, which at the time of interaction is in the basic vibrational state, absorbs a photon with the frequency ν_0 . Part of the photon's energy is transferred to the molecule with frequency ν_m and the resulting

frequency of scattered light is reduced to $\nu_0 - \nu_m$. This Raman frequency is called Stokes frequency, or just “*Stokes*”.

- c. A Raman-active molecule, which at the time of interaction is already in the excited vibrational state, absorbs a photon with frequency ν_0 . Excessive energy of the excited Raman active mode is released, molecule returns to the basic vibrational state and the resulting frequency of scattered light is increased to $\nu_0 + \nu_m$. This Raman frequency is called Anti-Stokes frequency, or just “*Anti-Stokes*”.

In summary, there will be three types of signals scattered from the sample surface after laser interaction with the molecules in the sample, i.e., Rayleigh scattering, Raman Stokes and Anti-Stokes scatterings. The Rayleigh scattering is useless for practical purpose of molecular characterization, but about 99.999% of all incident photons in spontaneous Raman undergo Rayleigh scattering. This predominant scattering can be reduced by the instruments in the modern Raman spectrometer, such as notch filters and tunable filters, to obtain high-quality Raman spectrums. The residual 0.001% of the incident light produces inelastic Raman signals (Stokes and Anti-Stokes), from which the energy shifts provide information about the vibration modes in the system. The energy shift, also called “Raman shift”, is unique to each molecule, allowing the chemical identification of compounds within a sample. Mostly, only the Raman Stokes scattering is used to generate Raman spectrum because of their much higher intensities than Anti-Stokes (Hann, 2007).

3.2.2 Raman Shift

Raman shift is the energy difference between the incident and emitted laser. It is typically reported in wavenumber with a unit of inverse length. To convert spectral wavelength to shift in Raman spectrum, the following formula should be used:

$$\Delta\omega = \left(\frac{1}{\lambda_o} - \frac{1}{\lambda_1}\right) \quad (3.1)$$

where $\Delta\omega$ is the Raman shift expressed in wavenumber, λ_o is the excitation wavelength, λ_1 is the wavelengths of the emitted lights. It should be pointed out that Raman shift is independent of the wavelength of the laser used. This means the peaks for a component should always be at the same shift positions when different lasers are used.

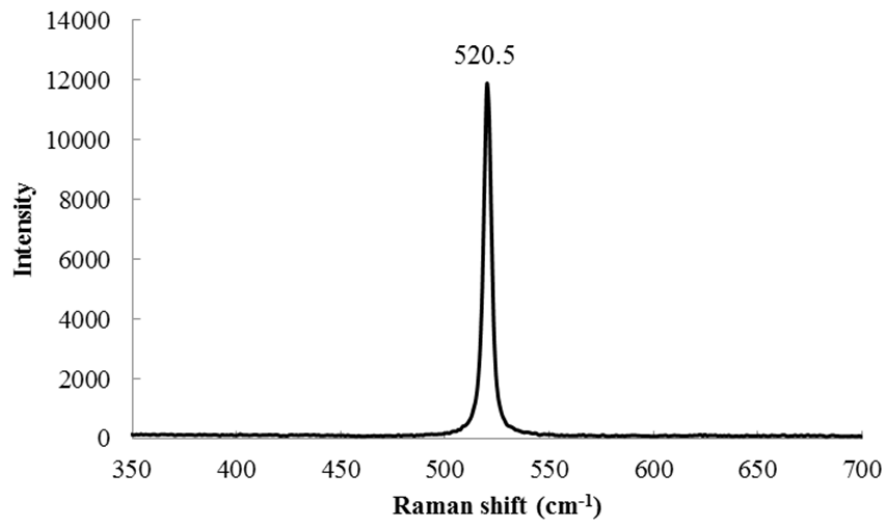


Fig. 3.2. Spectrum for silicon wafer used for calibration

Fig. 3.2 shows the Raman spectrum for the silicon wafer which is used for calibration purpose before each measurement. It can be seen that a typical spectrum consists of two parts, Raman shift and peak intensity. The silicon wafer has the strongest

peak at the Raman shift of 520.5 cm^{-1} , which is taken as the characteristic peak for silicon during the calibration process. Another important parameter provided by the spectrum is peak intensity. Intensity is proportional to the concentration of the specific compound in the sample. Higher intensity normally indicates higher content of that compound.

3.3 Raman Spectroscopy in Cement Chemistry

3.3.1 Characterization of Cement Clinker Phases

In cement chemistry, RS has received attentions for its application in characterizing pure clinker phases during the past four decades. The pioneering research of RS was carried out by Bensted (1976). In his study the main Raman shifts of various synthetic clinker phases were identified. He found strong Raman shifts for C_3S , C_2S , and C_3A at 848 cm^{-1} , 864 cm^{-1} , and $740\text{-}756\text{ cm}^{-1}$ respectively. This research was soon followed by the similar work conducted by Conjeaud and Boyer (1980). They studied the synthetic clinker phases as well as the clinker phases in white and grey cements. The peak with highest intensity for synthetic C_3S was at 845 cm^{-1} . But in Portland cement, it had the strongest intensity at 832 cm^{-1} . The shift discrepancy was caused by the increased structure disorder introduced with foreign ions in the cement. The assignment of synthetic C_2S was at the shift of 860 cm^{-1} . In cement, it had the similar characteristic peak. They also characterized the synthetic C_4AF peak at around 750 cm^{-1} .

Thereafter, Bonen et al. (1994) also analyzed both the synthetic and cement clinker minerals. The characteristic peak for synthetic C_3S and C_2S was found at the shift of 541 and 799 cm^{-1} respectively. The C_3S in cement was found to have the strongest

peak at 666 cm^{-1} . They also assigned two comparable strong peaks for synthetic C_3A at 504 and 753 cm^{-1} . These assignments were significantly different from the results obtained by Bensted (1976) and Conjeaud and Boyer (1980). This may be caused by the different lasers used in their studies. The 1064 nm laser was applied in the research of Bonen et al. (1994), while Bensted (1976) used two lasers with wavelength of 488 and 632.8 nm and Conjeaud and Boyer (1980) employed the 514 nm laser. However, the findings by Bonen et al. (1994) had some correlations with the results obtained by Newman et al. (2005), who compared Raman shifts gained by near infrared (1064 nm) and visible (514 and 632.8 nm) excitations on synthetic clinker phases and 3 different Portland cements. For the visible lasers, Newman et al. (2005) assigned the peaks with the shifts of 510 and 760 cm^{-1} to synthetic C_3A and 840 to synthetic C_3S , which agreed reasonably well with those obtained by Bensted (1976) and Conjeaud and Boyer (1980). Since Raman shifts for the same phase is independent of the laser wavelength, the researchers concluded that the characteristic Raman shifts obtained by the visible lasers should be true because these shifts were detected by both lasers. On the contrary, the peaks gained by 1064 nm laser were purely originated from the fluorescence phenomenon. They were not real Raman Stokes. Recent researchers also found the similar peak assignments to those of Newman et al. (2005) by using various visible lasers (Gastaldi et al., 2007; Frías and Martínez-Ramírez, 2009; Torréns-Martín et al., 2013).

3.3.2 Characterization on Cement Hydration

Besides its application in the clinker phases, RS has also been used in studying the hydration of pure clinker phases, white cement, and Portland cement. The first work was done by Bensted (1976). The degree of hydration of white cement at the ages from 1

to 4 days has been followed by tracking the decrease in the peak intensity of C_3S and C_2S . In addition, in his work, the evolution of gypsum was also used to follow the hydration process. The initial gypsum peak at 1010 cm^{-1} shifted slightly to 1015 cm^{-1} due to the formation of ettringite. A shift at 994 cm^{-1} was observed due to monosulfate formation after 1 day. The formation of CH was also monitored with its peak at 355 cm^{-1} . Bensted (1976) also reported that C-S-H gel did not show any detectable bands due to its poor crystallinity. But Conjeaue and Boyer (1980) identified the peak at 670 cm^{-1} for synthetic C-S-H and 640 cm^{-1} for the C-S-H gel formed in the hardened Portland cement paste. An in-situ qualitative and quantitative study of the hydration of pure C_3S was carried out by Tarrida et al. (1995). They assigned 662 cm^{-1} to synthetic C-S-H and 640 cm^{-1} to C-S-H gel in the cement paste. Their research was followed by Kirkpatric et al. (1997) who conducted an extensive characterization on the synthetic C-S-H with various C/S ratios from 0.88 to 1.45. It was found that the main peaks for C-S-H were at 450 cm^{-1} and $664\text{-}669\text{ cm}^{-1}$ and CH at 325 cm^{-1} . Garbev et al. (2007) and Black et al. (2007) later confirmed the findings by Kirkpatric et al. (1997) on the RS assignments of C-S-H gel and CH.

In 2006, Black et al. studied the hydration of calcium aluminate. They reported that ettringite was found to have a peak at $988\text{-}990\text{ cm}^{-1}$. The detection of ettringite happened at the very early age of hydration, even at 3 minutes after mixing C_3A with gypsum. And the gypsum was characterized by the peak at 1009 cm^{-1} . The conversion of ettringite to monosulfate and gypsum was found after C_3A hydrated for 2 weeks. The formed monosulfate had a peak centered at $981\text{-}983\text{ cm}^{-1}$. The similar assignments for

ettringite and monosulfate were also done in the research of Torr ens-Mart n et al. (2013), which were at the shift of 989 and 979 cm^{-1} , respectively.

3.3.2 Sulfate Attack and Carbonation

Gypsum and ettringite were characterized in the RS studies on the hydration of clinker phases and cements. These two components can also be found in the sulfate-attacked concrete. The attack is caused by the reactions between paste and soluble sulfate ions. Another commonly encountered product from sulfate attack is thaumasite, which forms primarily at low temperatures (0-5°C) when there is an available source of CO_3^{2-} . The source could either be limestone dust, which is being increasingly used as a filler, or limestone aggregate (Bensted, 1999). Therefore, different from gypsum and ettringite, both the sulfate and carbonate peaks were found in the pattern of thaumasite. This feature can be utilized to distinguish thaumasite from ettringite and gypsum in the sulfate-attacked concrete. The latter two components only had sulfate peaks. Brough and Atkinson (2001) assigned main peaks for thaumasite at 990 and 1076 cm^{-1} . The similar assignment was also drawn in the paper written by Sahu et al. (2002). Raman studies on sulfate attack were also carried out by several other authors (Deng et al., 2002; Renaudin et al., 2007; Gatta et al., 2012). The findings by these researches were consistent with those of Brough and Atkinson (2001) and Sahu et al. (2002).

Carbonation, another common deterioration of concrete, can also be detected by RS. As explained by Bensted (1976), carbonates were frequently encountered in cement chemistry in the form of calcite (CaCO_3). He studied the carbonation effects of ettringite, C-S-H, monosulfate, and white cement. The strongest CO_3 shift was shown at 1090 cm^{-1}

(Bensted, 1977). Other researchers (Bonen et al., 1994; Martinez-Ramirez et al., 2003; Newman et al., 2005) assigned the shift of 1085-1087 cm^{-1} to carbonate. These assignments also correlated well with what is currently available in the open literature for calcite.

3.4 RS Peak Assignments

Table 3.1 summarized the characteristic Raman shifts for the different cement ingredients and hydration products from the above discussed researches. These shifts will be used to characterize the cement and paste components in the following chapters (Chapters 4-7). It can be seen from this table that each compound has unique Raman shift(s) that can be used as the characteristic peak(s). To study the cement hydration process, Raman shift(s) should be assigned accordingly. For example, C_3S has strong vibrations at the broad shifts from 813 to 890 cm^{-1} , but the most intensive peak locates at the region of 840 to 848 cm^{-1} . Thus in the present work, the peak in this region is taken as the characteristic shift for C_3S . It can also be seen from this table that one substance may have multiple assigned Raman shifts. Taking C-S-H gel as an example, it has two assigned regions of characteristic shifts. This is caused by the two different types of comparably strong molecular vibrations occurring in the two regions. The peak at 600-700 cm^{-1} is resulted from the Si-O-Si bending mode in the C-S-H gel, while the one at 450 to 500 cm^{-1} corresponds to the O-Si-O bending (Kirkpatrick et al., 1997; Garbev et al., 2007).

Table 3.1. Characteristic Raman peaks for cement ingredients and hydration products summarized from pioneering researches

Chemical ingredients	Characteristic Raman shifts (cm ⁻¹)
C ₃ S	834 – 848
C ₂ S	846 – 864
C ₃ A	750 - 760, 504 – 510
C ₄ AF	740 – 770
Gypsum	1008-1020
CH	356-359
C-S-H gel	600 - 700, 450 – 500
Ettringite	987 – 992
Monosulfate	979 – 984

3.5 Summary

During the past decades, Raman spectroscopy has been utilized as an efficient tool in cement chemistry. By reading the unique Raman shift(s) belonging to each individual component, the compositions in cement and paste can be characterized, including the clinker phases, hydration products, and deteriorative substances from sulfate attack and carbonation. However, previous RS researches mainly focused on studying the powdered or hardened samples. There is a lack of study on the fresh cement paste during setting period. In next chapter, an in-situ study on the continuous hydration of cement paste after mixing till final set will be discussed.

CHAPTER 4

SPECTRAL ANALYSIS ON THE HYDRATION PROCESS OF PORTLAND CEMENT PASTE DURING SETTING

4.1 Introduction

The previous studies with Raman spectroscopy by other researchers have provided characteristic Raman shifts for different cement ingredients and hydration products. But there are very few studies reported on the observation of Portland cement during the setting period. Garg et al. (2013) studied the hydration process of Portland cement paste blended with different types of fly ash, concentrating on the sulfates and hydroxides evolution from 0.2 h to 56 days. However, the measurements were applied to different specimens for each specific hydration age. The continuous observation on the hydration process of the Portland cement paste on the same sample during setting has not yet been implemented. It should be noted that water has a weak Raman scattering, which does not interfere with the peaks of other components dissolved in it. This makes RS a good method for wet samples. In this chapter, an in-situ observation on the hydration process of fresh cement paste will be discussed. Cement paste with w/c ratios from 0.35 to 0.60 were studied with RS analysis. For all the pastes investigated, the formation of CH, C-S-H gel, ettringite, and monosulfate in the cement paste were detected at different

hydration ages. These detections were further analyzed together with the setting time and heat evolution from the Vicat needle and calorimetric tests, respectively. It was found that the C-S-H gel always firstly appeared in between dormant period and initial set. And the intensity of ettringite started to increase when dormant period was completed.

4.2 Raw Materials

Cement used in the present study was commercial Type I Portland cement from CEMEX, Louisville plant (KY, USA). Major chemical and mineral compositions of this cement are listed in Tables 4.1 and 4.2, respectively. The chemical compositions were gained by XRF analysis, and the mineral compositions were calculated based on the Bogue's equations (Taylor, 1997). The mean size of cement particles was 13 μm , determined through a laser particle size analyzer. The Blaine surface area was 400.8 m^2/kg .

Table 4.1 Chemical compositions of Type I Portland cement used

Compound	Weight, %
CaO	64.88
SiO ₂	20.49
Al ₂ O ₃	4.56
Fe ₂ O ₃	2.82
SO ₃	3.17
MgO	2.57
Na ₂ O	0.16
K ₂ O	0.39
LOI	1.20

Table 4.2 Mineral compositions of Type I Portland cement used

Clinker Phase	Weight, %
C ₃ S	64.62
C ₂ S	9.99
C ₃ A	7.33
C ₄ AF	8.58

Reagent-grade calcium hydroxide, sodium hydroxide, and potassium hydroxide (from Fisher Scientific Company, Fair Lawn, NJ) were also used in the study. Calcium hydroxide was in the powder form, while the latter two hydroxides were solids with hemispherical shape.

4.3 Sample Preparation

For RS measuring on the Portland cement and CH, around 4 grams of each type of powders was transferred to the standard tissue culture dishes (cylindrical plastic sample holders) with a diameter of 50 mm and depth of 10 mm. With a thin layer of the powder covering the bottom, the sample holder was slightly tapped to provide relatively smooth surface. Then the Raman spectrums were taken from the sample surface. It took only 1 to 2 minutes to prepare the powder sample. A prepared cement powder sample is shown in Fig. 4.1(a).

For cement paste preparation, firstly the pastes with w/c ratios of 0.35, 0.40, 0.50 and 0.60 were properly hand mixed for 5 minutes and transferred to the same sample holders used for power samples. After the sample holders were slightly tapped to consolidate the pastes, specimens were ready to be studied with RS. An example of the

prepared paste sample is displayed in Fig. 4.1(b). Including mixing, it took around only 6-7 minutes to prepare the paste sample. Compared to the techniques such as SEM and XRD, the sample preparation for RS was much simpler.

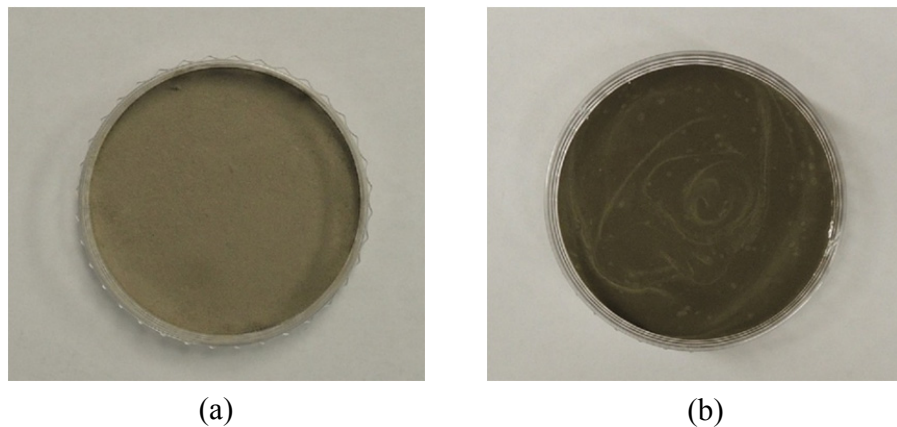


Fig. 4.1. Cement powder (a) and paste (b) samples prepared for RS measurement

All the Raman tests were carried out under the controlled laboratory conditions with a temperature of 22 °C and a relative humidity of 35%. The hydration age was measured from the instant when cement and water were initially mixed.

4.4 Raman Instrumentation

The Raman system used was a Renishaw Invia micro-Raman spectrometer with a CCD detector. Samples were illuminated with a 633 nm He-Ne Laser (Renishaw RL 633 laser). The laser power was about 4mW on the surface of the sample. According to other researchers, the relatively weak heat generated by this laser power would not alter the hydration rate of the cement paste under observation (Tarrida et al., 1995; Garg, 2012). During each test, scanning was carried out by using the syncro mode from 300 to 2000

cm^{-1} . The exposure time for each scan was 10 seconds and it took 40 to 60 seconds to acquire one spectrum. All the spectra were obtained with a 50 \times magnification objective. The laser spot had a diameter of 4 μm with this magnification. Before each test, calibrations were done by utilizing the 520.5 cm^{-1} line of a silicon wafer (Fig. 3.2). Data acquisitions were carried out with the WiRE3.3 software (Renishaw, Illinois). All the spectra were acquired with these illustrated experimental parameters.

4.5 Testing Procedures and Data Manipulation

4.5.1 RS Measurements

For all the dry powders (Portland cement and calcium hydroxide) that were used, RS analysis was applied at five random locations for each sample, and three samples were tested. The average of the total fifteen measurements was used for the components identification in this study.

For all the wet cement pastes, RS was implemented on each paste specimen at three separated locations, shown as A, B, and C in Fig. 4.2. All the locations were about 10 mm away from the inner edge of the sample holder, and the distance between any two of them was 26 mm. For each location, five positions (e.g., A1 to A5 in Fig. 4.2) which were 100 μm apart were measured. All the paste spectra shown in the following sections were averaged from the RS patterns of the specific five positions at one location. It took approximately 7 minutes to complete the measurements of one location; therefore, the time interval set for measuring each location was 10 minutes. For each sample, RS measurements started from location A at 20 minutes after mixing, followed by locations

B and C in sequence. After one round of the measurements, location A was measured again, i.e., location A was measured every 30 minutes, so were locations B and C. Measurements were carried out continuously from 20 minutes after mixing to final set (8 to 9 hours). For cement paste with each w/c ratio, four replicas were tested.

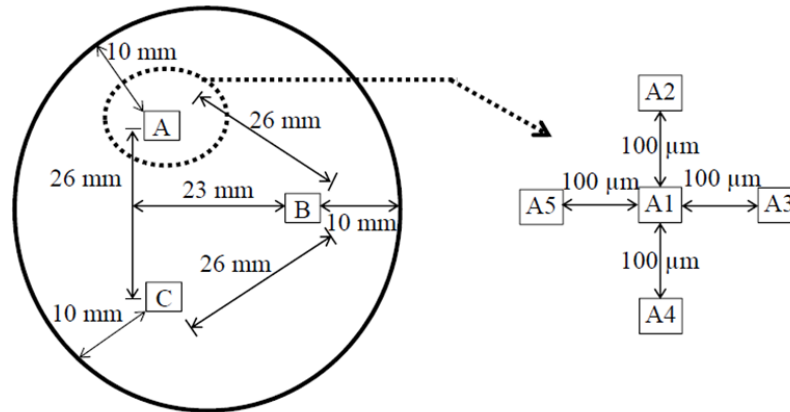


Fig. 4.2. Configuration of the measuring area

4.5.2 Raman Data Manipulation

To facilitate more explicit identification of peaks, background correction was applied to each gained spectrum. An example is given in Fig. 4.3, showing the gained and processed spectra from one position in the cement paste with a w/c ratio of 0.50 at the hydration age of 330 minutes by applying the cubic spline interpolation (Bartels et al., 1987). The small square boxes in the figure were the places where the interpolated points were inserted. It can be seen that the procedure only removes the baseline from the original spectrum, and the position and relative intensity of each individual peak were not altered. In this dissertation, all the originally obtained spectra have been processed for background subtraction with this method before averaging.

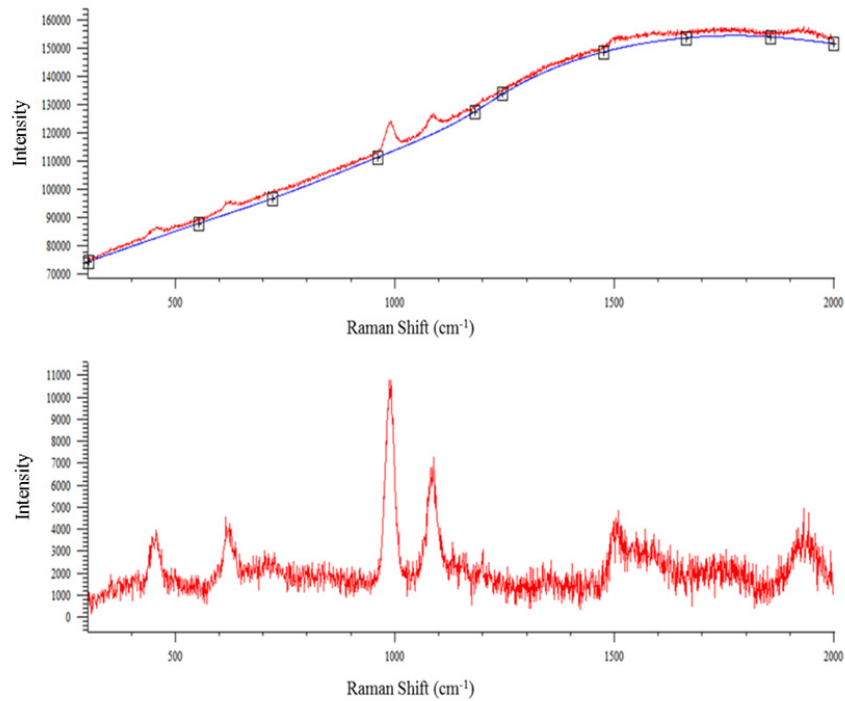


Fig. 4.3. Gained (a) and background subtracted (b) spectra from one position in the cement paste with a w/c ratio of 0.50 at the hydration age of 330 minutes

4.5.3 Complementary Experiment – Vicat Needle and Calorimetric Heat Methods

The initial and final setting time of the cement pastes with four different w/c ratios were determined by the Vicat needle tests, which were carried out according to the ASTM Standard C191 (ASTM, 2008). When the needle penetrated into the cement paste for 25 mm, initial set was achieved. Final setting was attained when there was no mark on the specimen surface with a complete circular impression. The test on cement paste of each w/c ratio was repeated three times to ensure the precision of the determination. Isothermal conduction calorimetry was also implemented on the cement pastes with four w/c ratios according to the ASTM C1702 (ASTM, 2009).

4.6 Comparison between Cement Powder and Paste

For comparison purposes, RS analysis was firstly applied to dry cement powders (Type I, Tables 4.1 and 4.2). The tests were repeated three times, and five measurements were conducted each time. The averaged spectrum of the total 15 spectra is shown as Pattern A in Fig. 4.4. In this pattern, the two strongest characteristic peaks located at 833 and 887 cm^{-1} are assigned to Si-O stretches in C_3S and C_2S , respectively. These two peaks have higher intensities than any others, suggesting that C_3S and C_2S are the two major clinker phases in Portland cement. C_3A has a bending vibration of AlO_4 assigned to the shift at 552 cm^{-1} ; however, the intensity is much lower than that of C_3S or C_2S . This corresponds to a lower content of C_3A in cement. While an AlO_4 stretching vibration in C_3A of around 750 to 760 cm^{-1} falls into the broad overlapped band, C_4AF has almost the same Raman shift as C_3A in the range of 750 to 760 cm^{-1} due to the influence of ferrite ions. For that reason, the characteristic shift for C_4AF cannot be separated from this range and no shift was assigned to it in this study. For most of the research conducted on early hydration, researchers focused on the hydration products, such as ettringite, calcium hydroxide, and C-S-H gel, which are mainly formed by C_3A and C_3S hydration (Gallucci et al., 2010; Ylmen et al., 2010; Pang et al., 2013). As a result, the lack of assigned shift for C_4AF is not likely to be a significant defect regarding the early-age hydration study. In this pattern, a sharp peak at 1005 cm^{-1} was recognized as the sulfate band stretching mode. This sulfate band can be related to gypsum and hemihydrate. The latter is formed from gypsum that loses water during the grinding process. The small discrepancies regarding the characteristic shifts between the present study and previous researches (Table 3.1) may be attributed to the difference in cement manufacturers.

Information is not available for the lower ($<350\text{ cm}^{-1}$) and higher ($>2000\text{ cm}^{-1}$) shifts in the spectrum.

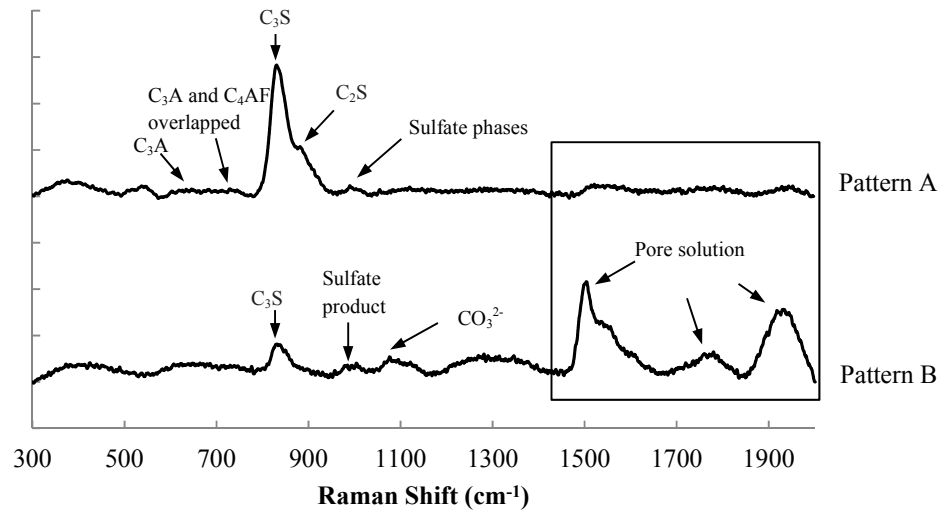


Fig. 4.4. Raman Pattern (A) for Portland cement powder and Pattern (B) for cement paste with a w/c ratio of 0.40 hydrating for 20 minutes

The spectrum of cement paste with a w/c ratio of 0.40 after 20 minutes' hydration is shown as pattern B in Fig. 4.4. Comparing the two patterns in this figure, it can be seen that the overall intensity of all the cement components decreased after mixing with water. The strong intensities of C₃S and C₂S in cement powder (pattern A) reduced dramatically in the wet cement paste (pattern B). These dramatic decreases do not mean most of the silicate components have been reacted. Instead, this indicates that they are not easily to be detected after dissolution. From Pattern B, it can also be seen that aluminate phase is not detected in the pattern, which should be attributed to the quick hydration between C₃A and gypsum. This reaction generates sulfate products with different characteristic Raman shifts from gypsum, which will be discussed in details in the following paragraphs. One

can also see a peak at the shift of 1088 cm^{-1} representing the ion of CO_3^{2-} in pattern B. The presence of this peak may be caused by the dissolution of carbon dioxide into the surface layer of cement paste. This carbonate peak was assumed not to affect the Raman analysis on the hydration process significantly, because its peak position was not in the vicinity of cement ingredients or hydration products.

4.7 Hydration Progress Detected by RS

RS measurements were carried out on cement pastes every 10 minutes in locations A, B, and C (Fig. 4.2) from 20 minutes after mixing till 8 to 9 hours. Plenty of Raman spectrums were gained by these measurements. Analyzing paste hydration every 10 minutes on different locations may obtain the same results as investigating one same location with the time interval of 30 minutes. Fig. 4.5 shows the RS results for three locations measured in sequence during the same round of measurement in the cement paste with a w/c ratio of 0.50. When comparing the spectra gained from locations A, B, and C in this figure, it can be seen that these three locations give almost the same patterns at the hydrating ages of 140, 150, and 160 minutes, respectively. Although there were time intervals among the three spectra, the intensity ranges and shift positions of the Raman peaks in the patterns do not yield any significant differences. Hence, the need for showing spectra on all the three locations was eliminated and only the representative patterns from one location will be shown in the following discussions.

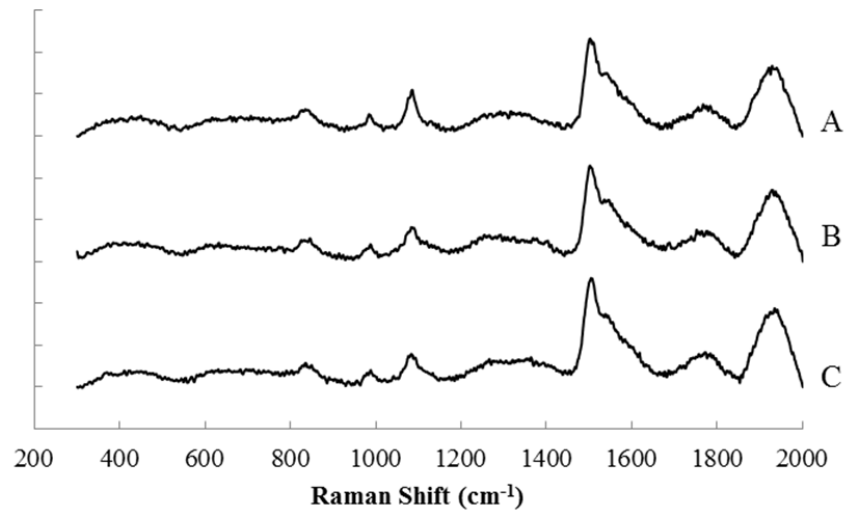


Fig. 4.5. Averaged spectra from the three positions at different hydrating ages in the paste with a w/c ratio of 0.50

4.7.1 Calcium Hydroxide Band

The most significant difference between the patterns for dry cement powder and wet paste is the peaks at the higher shifts from 1400 to 2000 cm^{-1} (boxed part in Fig. 4.4). There was no available information from previous RS researches about these peaks. It is reasonable to postulate they are related to the pore solution, because those intensive peaks appeared in the pattern of cement paste after mixing with water. The pore solution is known to mainly contain ions of Na^+ , K^+ , Ca^{2+} , and OH^- , resulting in the high alkalinity in the cement paste (Taylor, 1997). Therefore, RS analysis was also implemented on the pure (>99%) crystals of sodium hydroxide (NaOH), potassium hydroxide (KOH), and calcium hydroxide (CH) in the same way as analyzing the dry Portland cement powder. Fig. 4.6 shows the patterns for all the three alkalis. It can be seen that excluding the peaks at the lower shifts (<500 cm^{-1}), NaOH and KOH have the strongest peak at the shifts of

1080 and 1060 cm^{-1} , respectively, while CH has multiple intensive peaks at 1400 to 2000 cm^{-1} , which are taken as the characteristic peaks for CH in the present study. Those CH peaks are also found to be present in Pattern B of Fig. 4.4. For a better comparison, the 1400 to 2000 cm^{-1} section from the spectra of cement paste (Pattern B in Fig. 4.4) and pure CH crystals (Fig. 4.6(c)) were enlarged and are displayed in Fig. 4.7. According to this figure, both the shapes and positions of peaks in the two spectral segments match perfectly, except that the pure CH has a smoother curve. Through the RS analysis on these alkalis, the peaks at the shifts higher than 1400 cm^{-1} in the paste pattern (Pattern B in Fig. 4.4) are attributed to the presence of CH in the cement paste. It should be noted the formation of solid CH from cement hydration takes longer, normally a couple of hours after mixing. The detection of CH in wet cement paste at 20 minutes after mixing does not hint the formation of CH crystal. Instead, this detected CH is the combination of Ca^{2+} and OH^- caused by the absorption of OH^- onto the surface of Ca^{2+} , not the CH crystals precipitated.

In all the cement pastes (e.g., Fig. 4.8), CH was detected from the initial measurement and its intensity only increased slightly during the setting period. This was also observed by other researchers (Taylor, 1997) who periodically extracted and analyzed the aqueous phases in the cement-water pastes and suspensions. The slight increase may be explained by the approximate balance between the continued dissolution of cement phases and the precipitation of hydration products.

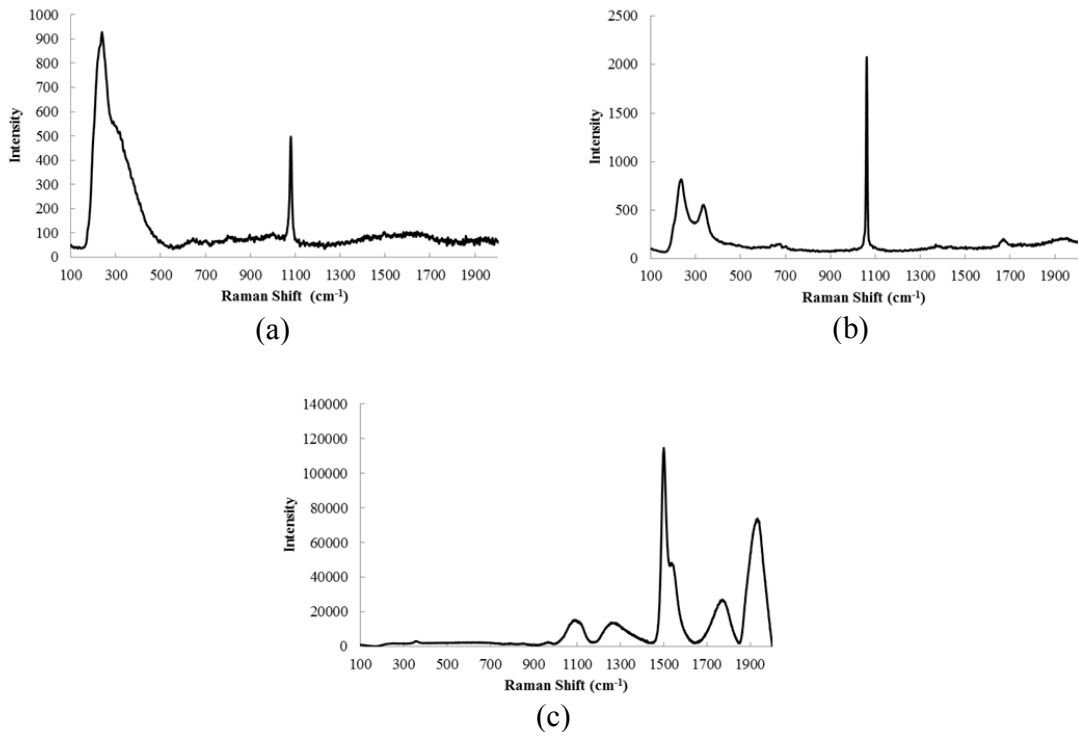


Fig. 4.6. RS patterns for the pure (a) sodium hydroxide; (b) potassium hydroxide; and (c) calcium hydroxide

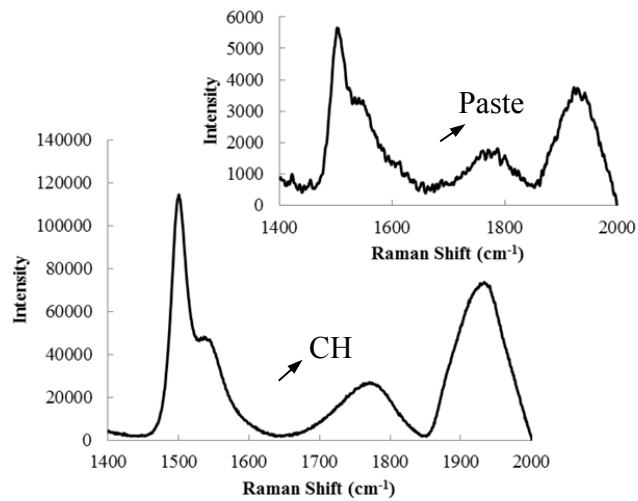


Fig. 4.7. Enlarged region of 1400 to 2000 cm^{-1} in the patterns of pure CH and cement paste with a w/c ratio of 0.40 at the hydration age of 20 minutes

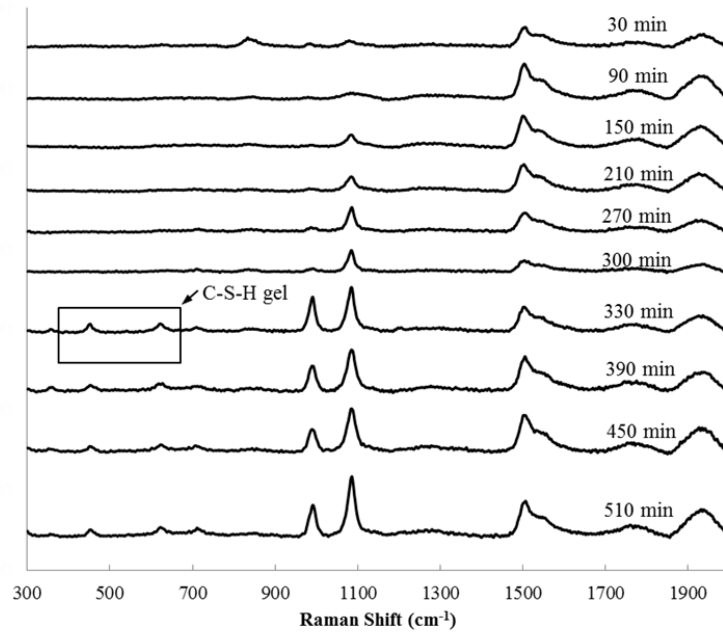


Fig. 4.8. Spectra of cement paste with a w/c of 0.60 hydrated for 30 to 510 minutes

4.7.2 C-S-H Gel Bands

For each cement paste, since the RS analysis was conducted at the same location every 30 minutes without altering the curing conditions, the hydration progress can be investigated by comparing the obtained RS spectra at different hydration ages. Fig. 4.8 shows the RS patterns for the cement paste with a w/c ratio of 0.60 at the hydration age from 30 to 510 minutes. It can be seen that two minor peaks (boxed) at 450 and 625 cm^{-1} appear in the pattern of 330 minutes. These two peaks are not present in the same paste at 300 minutes of hydration. They should be assigned to the C-S-H gel based on previous studies by other researchers (Table 3.1). According to Scrivener (1989), cement grains may be surrounded with outer product of C-S-H gel after 3 hours of hydration (Fig. 2.6

(c)). Because RS is more efficient in detecting the products on the sample surface, the detection can be assumed to be the outer layer of C-S-H gel.

These two peaks indicating C-S-H gels were found in all the cement pastes with four w/c ratios, however, the first appearance of C-S-H gel in each cement paste was at different hydration age. For cement pastes with w/c ratios of 0.35, 0.40, 0.50, and 0.60, the first detection of the C-S-H gel happened at 100, 140, 230, and 330 minutes, respectively. It indicates a relatively later formation or detection of C-S-H in paste with higher w/c ratio. This is because the cement paste with higher w/c ratio may undergo longer dormant period, which causes the later hydration of C_3S and thus the delayed formation of C-S-H gel. In addition to that, when cement paste contains lower concentration of cement grains, it will also take longer to accumulate the minimum amount of C-S-H gel to be detected by RS. It should also be noted that bleeding may have effect on the later detection of C-S-H gel in the cement paste with higher w/c ratio as well. This research also found the persistence of C-S-H gel peaks in the RS patterns after their first detections throughout the measuring period. There was not a significant change over time regarding the peaks intensities and positions. This may be inferred that only the outer layer of the C-S-H gel was detected even with the increasing hydration age.

4.7.3 Sulfate Bands

Pattern B in Fig. 4.4 is the cement paste hydrating for 20 minutes after mixing, in which the sulfate product (i.e., ettringite) has already presented. This should be attributed to the quick hydration of C_3A with gypsum. Although the sulfate hydration products were observed consistently for each paste in the measuring duration, the positions and

intensities of the sulfate peaks were found to shift and change. This is caused by the active sulfates chemistry at the early age of cement hydration. C_3A hydration consumes gypsum and produces ettringite. After the depletion of available gypsum, C_3A reacts with the present ettringite to generate monosulfate (Eq. (2.8)). Therefore, there may be simultaneous presence of different types of sulfate phases in the hydrating cement pastes. From previous studies, the assigned Raman shifts for monosulfate, ettringite, and gypsum were 979-984, 987-992, and 1008-1020 cm^{-1} (Table 3.1), respectively. Since these three sulfates have fairly close characteristic shifts, when analyzing the sulfate phases, the shift bands between 950 cm^{-1} and 1050 cm^{-1} were zoomed in to differentiate each individual sulfate phase.

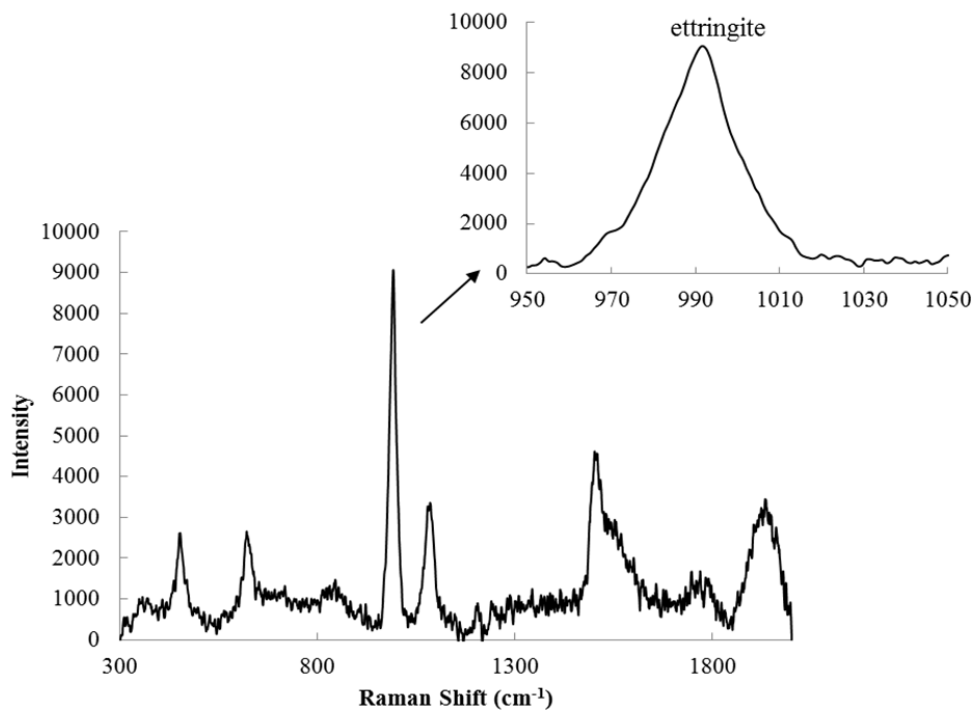


Fig. 4.9. Spectrum for cement paste with a w/c ratio of 0.40 at the hydration age of 180 minutes

Fig. 4.9 shows a pattern of the cement paste with a w/c ratio of 0.40 at the hydration age of 180 minutes. The zoomed-in sulfate band is shown at the upper right corner of the figure. It can be seen from the sulfate band that the peak centering at the shift of 991 cm^{-1} has the highest intensity. Therefore, it is ascertained that ettringite is the dominant sulfate product at this hydration age. There may be some gypsum remaining and/or other sulfate phase(s) with their peaks obscured by the predominant ettringite, considering the peak broadness. The existence of the ettringite peak was consistent from the beginning of the measurement until about 6 hours. Starting from 360 minutes, when zooming into the sulfate region, one can see three individual peaks for this paste as shown in Fig. 4.10. These peaks were at the shifts around 983, 991, and 1005 cm^{-1} . The latter two peaks were assigned to ettringite and gypsum respectively (according to Table 3.1). The assignment of 983 cm^{-1} peak can be controversial. In current research, this peak was assigned to monosulfate because its shift fell into the characteristic shift range for monosulfate ($979\text{-}984\text{ cm}^{-1}$) (Black et al., 2007; Renaudin et al., 2007; Torr ns-Mart n et al., 2013), although a different assignment of this peak can also be found in the research of Garg et al. (2013). By comparing Figs. 4.9 and 4.10, it can be presumed that during the hydration age from 180 to 360 minutes, some portion of ettringite converted to monosulfate and gypsum (Black et al., 2006). Similar results were also found in the paste with a w/c ratio of 0.35, except that monosulfate appeared earlier in the pattern, which was at 140 minutes of hydration. Although the same approach was used for analyzing the pastes with w/c ratios of 0.50 and 0.60, there were no monosulfate detections in these two pastes during the measuring period. The reason can be the less amount of ettringite formed due to the lower concentration of cement particles. Since the conversion of

ettringite requires enough amount of ettringite to react with C_3A , it may take these pastes much longer to generate enough ettringite to initiate this reaction. Therefore, it is plausible to speculate that for pastes with higher w/c ratios (0.50 and 0.60), ettringite conversion may happen after the completion of setting, and monosulfate may be detected if the observation window is extended.

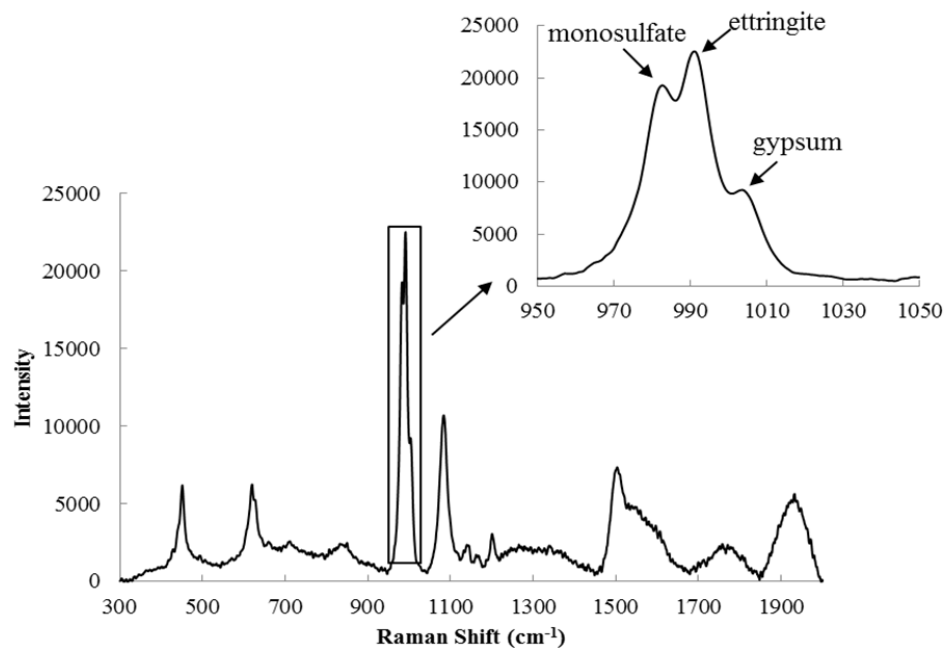


Fig. 4.10. Spectrum for paste with a w/c ratio of 0.40 hydrated for 360 minutes

Fig. 4.11 shows the position evolution of sulfate peaks in the cement pastes with all four w/c ratios during setting. Based on this figure, it can be seen that the three sulfate peaks are present consistently in the cement pastes with w/c ratios of 0.35 and 0.40 from 2 to 3 hours till the end of the measuring frame (Fig. 4.11(a) and (b)). But the peak shape of these sulfate phases in these two pastes were different. It is noted that peak at 991 cm^{-1} was much weaker than the other two peaks (983 cm^{-1} and 1005 cm^{-1}) in the cement paste

with a w/c ratio of 0.35, while in the paste with a w/c ratio of 0.40, 991 cm^{-1} peak has the predominant intensity compared to other two sulfate phases. From Fig. 4.11, it can also be seen that there was only one sulfate peak in the cement paste with w/c ratios of 0.50 and 0.60 (Fig. 4.10(c) and (d)). This peak was centered at about 991 cm^{-1} , which was assigned to ettringite (Table 3.1). In the cement paste with a w/c ratio of 0.50 (Fig. 4.11(c)), it is interesting to find that the ettringite peak was shifting slightly from 989 to 991 cm^{-1} with the increased hydration age from 260 to 540 minutes. However, for the paste with a w/c ratio of 0.6, the sulfate peak remained at 991 cm^{-1} throughout the whole studied duration.

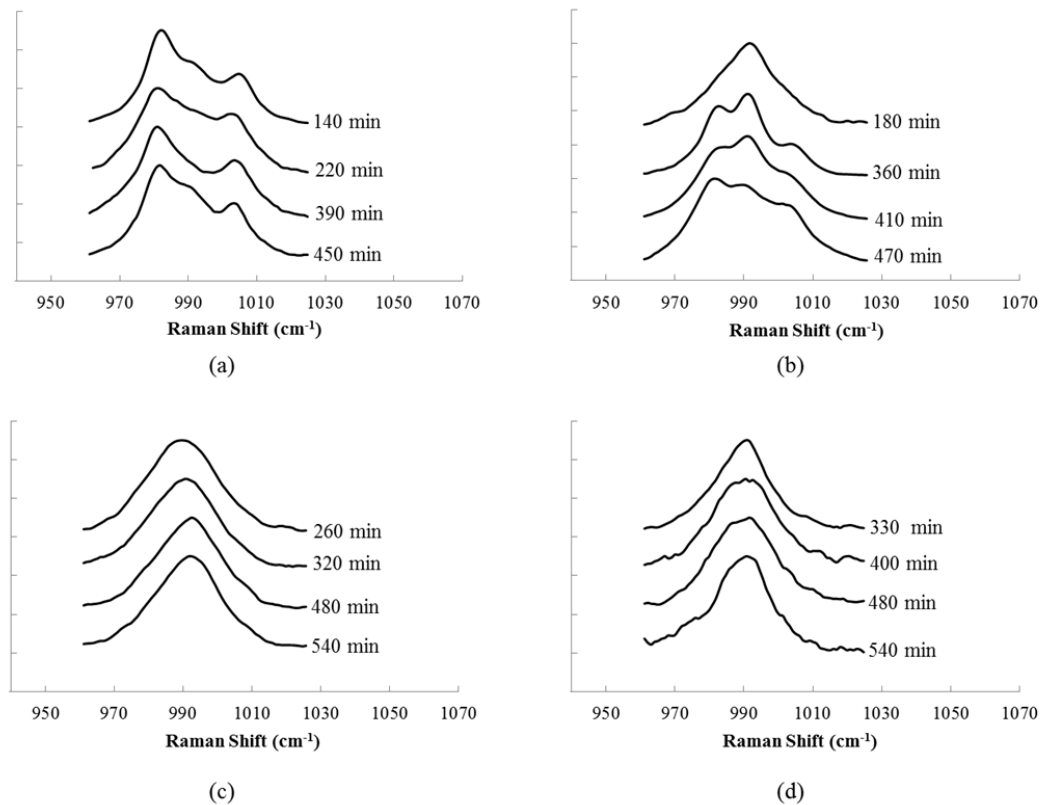


Fig. 4.11. Evolution of sulfate peak positions in cement pastes during setting: (a) w/c = 0.35; (b) w/c = 0.40; (c) w/c = 0.50; and (d) w/c = 0.60

4.7.4 Intensity Evolution of Sulfate Peaks

As aforementioned, during early hydration, reaction between C_3A and gypsum may increase the amount of ettringite (Eq. (2.7)), however, if the ettringite converts to monosulfate (Eq. (2.8)), its quantity may also be reduced. Therefore, studying the changes in intensities of ettringite can help to better understand early hydration and material behavior during setting. Fig. 4.12 shows four representative curves for the intensity changes of ettringite in the cement pastes with different w/c ratios. It should be noted that the intensity of ettringite in different cement pastes can be affected by various factors, including the degree of focusing, physical properties of sample surface, the system alignment of Raman spectroscopy, etc. Therefore, for a better comparison between cement pastes having different w/c ratios, the intensity of ettringite peak at 991 cm^{-1} was normalized to its highest value found from measuring each individual paste. Taking the paste with a w/c ratio of 0.35 as an example, it is noticeable that there are two transition points for ettringite intensity (shown as t_1 and t_2 in the figure), which are the intersections of the two corresponding trend lines obtained from linear regression. These two points divided the ettringite intensity development curve into three stages: a constant intensity stage in the first few hours, followed by an increasing stage starting at t_1 , and then the intensity decreases at t_2 until the end of the studied period. Same phenomenon can also be seen for the pastes with w/c ratios of 0.40, 0.50, and 0.60. This result matches the findings by other researchers with XRD and DTA analyses (Odler, 2003).

Table 4.3 lists the values of t_1 , t_2 , and Δt ($\Delta t = t_2 - t_1$) for all the cement pastes. From this table, it can be seen that t_1 increases with the increasing w/c ratio. This means the onset of the intensity increase was delayed in the cement paste with higher w/c ratio. The

reason can be the overall lower rate of ettringite accumulation in these pastes. The intervals between t_1 and t_2 (Δt) for the cement pastes also varied significantly. It decreased consistently from 3 and 4 hours in the cement paste with w/c ratios of 0.35 and 0.40 to less than 1 hour in the cement paste with a w/c ratio of 0.60. This indicates a much longer accelerating period of ettringite formation in the cement pastes with lower w/c ratios. This phenomenon may be attributed to the higher solid concentration in the original mixture to support the continuous reaction between C_3A and gypsum, while for those pastes with higher w/c ratios, these two components may be insufficient to sustain the long-lasting hydration.

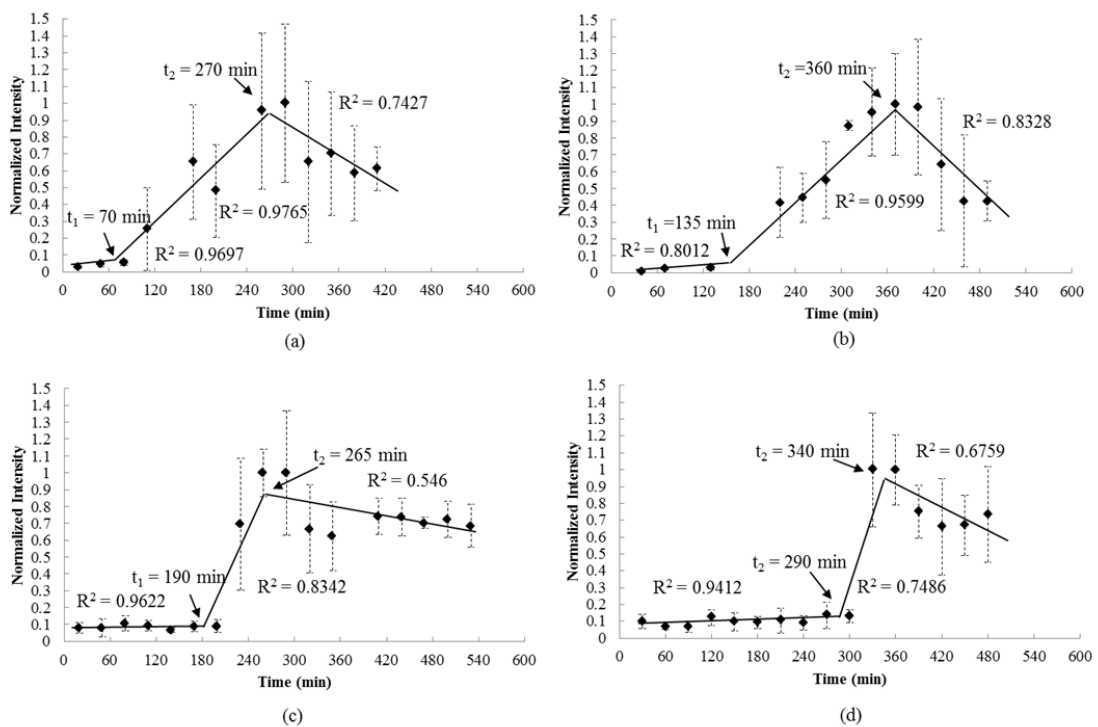


Fig. 4.12. Intensity changes of ettringite peak in the cement pastes with w/c ratios of: (a) 0.35; (b) 0.40; (c) 0.50; and (d) 0.60

Table 4.3 Transition points and duration of the accelerating period of ettringite formation in all the cement pastes

w/c	t ₁ (min)	t ₂ (min)	Δt (min)
0.35	70	270	200
0.40	135	360	225
0.50	190	265	75
0.60	290	340	50

4.8 Relationship between Raman Signals and Setting Time/Heat Signature

4.8.1 Results of Setting Time and Heat Evolution

As discussed, RS is capable of detecting the decrease or disappearance of cement ingredients and the appearance or increase of hydration products during the setting period. It will be interesting to figure out whether the Raman signals detected can be related to the macro-level properties of cement pastes. This purpose may be accomplished by analyzing the Raman signals and supplementary data gained by other commonly used macro-level methods together, because all of these methods measure the properties controlled by cement hydration. Therefore, the Vicat needle and calorimetric tests were also carried out on the cement pastes with all four w/c ratios that have been studied. The penetration and heat evolution curves for the cement pastes are shown in Fig. 4.13 and Fig. 4.14, respectively. From Fig. 4.13, it can be seen both the initial and final setting were completed later in the cement paste with higher w/c ratio. The measured initial and final setting times for each paste are listed in Table 4.4.

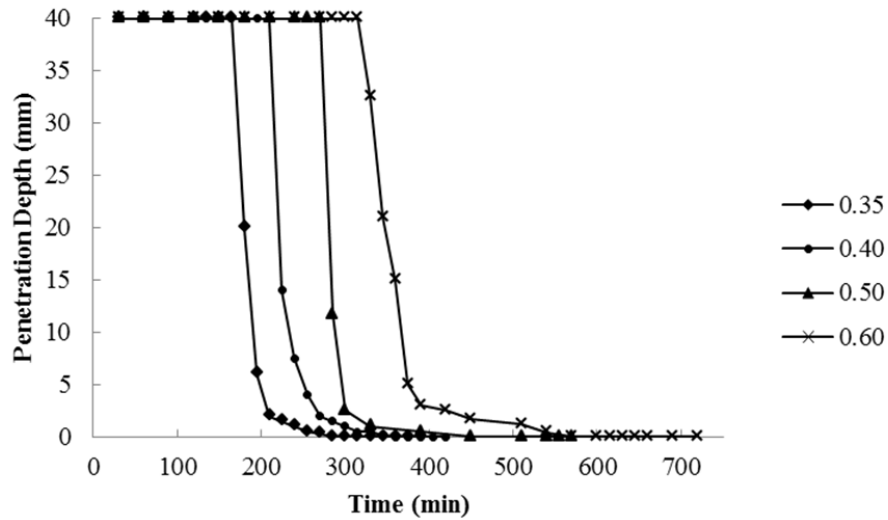


Fig. 4.13. Vicat needle penetration curves for the cement pastes with four different w/c ratios

Fig. 4.14 plots the measured heat evolution curves for cement paste with a w/c ratio of 0.60 during the first 10 hours after mixing. Point **b** in Fig. 4.14 is the maximum rate of heat releasing, indicating the end of the accelerating period. For point **a**, the end of the dormant period, currently there is no standard specification on its determination. In this work, intersect of the two straight lines which are tangential to the curved segments of dormant and accelerating periods was taken as the end of the dormant period. According to Fig. 4.14, the end of dormant period and maximum heat peak were achieved in the cement paste with a w/c ratio of 0.60 at 105 and 441 minutes respectively. This same method was also used to determine the end of dormant period and max heat peak in the cement pastes with other three w/c ratios. The obtained results are all listed in Table 4.4.

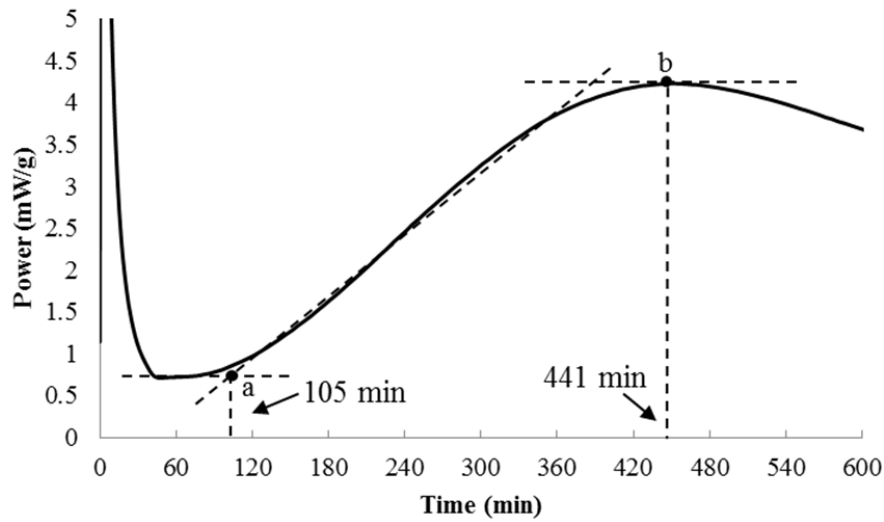


Fig. 4.14. Heat evolution for cement paste with a w/c ratio of 0.60 during the first 10 hours after mixing

Table 4.4 Summarized critical time points of setting time, heat signature, and Raman signals with unit of minute

w/c	Initial set	Final set	End of dormant period	Max heat peak	Ettringite t_1	Ettringite t_2	C-S-H gel
0.35	175±3	285±7	85	300	70	270	100
0.40	219±5	360±12	96	345	135	360	140
0.50	278±8	450±18	100	424	190	265	230
0.60	340±5	570±12	105	441	290	340	330

According to Table 4.4, it can be seen that the dormant period was only extended slightly when the w/c ratio of cement paste was increased. The maximum heat peak of the accelerating period was also delayed in the cement paste with higher w/c ratio. From this table, it can also be seen that for all the w/c ratios, the initial setting and dormant period differ significantly. The end of dormant period was always achieved earlier than the

initial setting. There was approximately 4 hours interval between the end of the dormant stage and the initial setting in the cement paste with a w/c ratio of 0.60. This time difference decreased with the decreasing w/c ratio. On the other side, the final set and the end of the acceleration stage on the heat curve appeared within the same time scale. There was only 15 to 20 minutes difference between them except in the cement paste with a w/c ratio of 0.60.

4.8.2 Raman Signals versus Setting Time and Heat History

In order to compare the RS results with the setting time and heat history in the cement pastes, Table 4.4 also includes the first and second transition time of the ettringite intensity (t_1 and t_2 from Fig. 4.12) and the appearance time of C-S-H gel (from *Section 4.7.2*) for all the cement pastes. It has been mentioned previously that the peak of ettringite can be found in the paste pattern at 20 minutes after cement mixed with water. This happened to the cement pastes with all four w/c ratios and this phenomenon was discussed as the result from the fast reaction between the C_3A and gypsum during the rapid reaction stage, which undergoes in the cement paste before the dormant period. By comparing the end of dormant period and the time when the ettringite intensity began to increase rapidly (t_1), it can be assumed that C_3A hydration nearly terminated during dormant period, leading to the almost constant ettringite intensity. This can especially be seen in the cement pastes with w/c ratios of 0.35 and 0.40. In these two pastes, the intensity increasing of ettringite started around or a little later than the end of dormant period. The higher w/c ratio causes the more significant difference between t_1 and the end of dormant period due to lower ettringite concentration in the paste. After the dormant period, the more available aluminate from the cement dissolution aroused the rehydration

of C_3A with gypsum, leading to the fast increasing stage for ettringite intensity. This stage lasts till the final setting in the cement pastes with w/c ratios of 0.35 and 0.40, while in the cement pastes with higher w/c ratios, the ettringite intensity stopped increasing almost at the time when the initial setting was achieved.

From Table 4.4, with the comparison between the C-S-H gel detection and heat evolution in the cement paste, it can be found that C-S-H gel was always detected after the dormant period. This is rational because during the rapid reaction and dormant periods, the main phenomena happening in the cement paste are the dissolution and reaction of the calcium aluminate and gypsum, dissolution of the calcium silicates, and nucleation of C-S-H gel (*Section 2.2.3*). After the dormant period, C-S-H gel nucleates starts to grow and precipitate onto the surface of the reacting cement particles, which is able to be detected by the Raman spectroscopy. It can also be seen from Table 4.4 that this C-S-H gel detection occurred earlier than the initial setting of the cement paste, regardless of the w/c ratios. This is because for the completion of initial setting, sufficient amount of C-S-H gel is required to connect the various components to form the microstructure which is strong enough to resist the 25 mm penetration in the Vicat needle tests (ASTM C191, 2008). Therefore, after its formation, time is needed for accumulating C-S-H gel to gain the initial setting in the cement paste. With the prolonged hydration after initial setting, the further hydration of calcium silicates (mainly C_3S) produces more C-S-H gel. This will make the paste more solidified, achieving its final setting. In the meantime, the maximum rate of heat releasing can also be caused by the main C_3S hydration.

4.9 Summaries and Conclusions

RS has already been proven to be a useful technique in studying various cement phases. In this work, Raman spectroscopy was used to investigate the hydration behaviors of the cement pastes with different w/c ratios after mixing till the final setting. Efforts were also put into finding correlations between the Raman signals and the setting time/heat evolution of the cement pastes. The following conclusions are drawn based on this study.

(1) The simple sample preparation procedures of RS analysis make it a good and appropriate method for in-situ observation of hydrating cement paste during the setting period.

(2) For the RS studies on cement pastes with four different w/c ratios, hydration products, including CH, C-S-H gel, ettringite, and monosulfate can be characterized. This makes RS a valuable tool to explore the hydration mechanisms of cement paste, especially during the setting period.

(3) For all the pastes, CH can be detected right after mixing and it appears consistently throughout the whole measurement with only slightly increased intensity.

(4) The higher the w/c ratio, the longer it took for the C-S-H gel to be seen in the RS patterns. And for all the studied pastes, C-S-H gel was detected after the dormant period (measured with the calorimetric method) but before initial setting time determined with the Vicat needle tests.

(5) For all the pastes, ettringite was found instantly after mixing. Its peak appeared consistently throughout the studied period, however, the peak intensity and position varied during the setting period. The intensity change of ettringite was found to be related to the dormant period of cement hydration.

CHAPTER 5

HYDRATION DIFFERENCE DETECTED BY RAMAN SPECTROSCOPY IN ULTRA-HIGH PERFORMANCE CONCRETE (UHPC) AND PORTLAND CEMENT PASTE

5.1 Background and Introduction

The application of RS on the hydration of fresh cement paste (Chapter 4) was extended to study the hardened ordinary paste and ultra-high performance concrete (UHPC). UHPC is a new type of concrete that is being developed by agencies concerned with infrastructure protection. It has been considered for use in a wide variety of applications, including highway infrastructure, precast concrete piles, seismic retrofit of substandard bridge substructure, etc. (FHWA, 2013). UHPC is a steel fiber reinforced cement composite material. Being different from a conventional concrete, a UHPC's compressive strength is in excess of 150 MPa, and it can be high up to exceeding 250 MPa (AFGC, 2002). This type of cement-based material is also distinguished by its constituent materials composites: typically finely ground silica flour, silica sand, silica fume, small steel fibers, blends of high-strength cements, high range water-reducing admixture, and water (FHWA, 2013). Silica flour and silica sand are inert in nature and do not react with water or components in cement paste. They are mainly work as the fine

fillers to form dense microstructure for UHPC. Another form of silica, silica fume, is amorphous and chemical reactive. It can react with calcium hydroxide (CH) produced from the hydration of calcium silicates (C_3S and C_2S) at the very early age (Neville, 2010). The reaction of silica fume and CH forms additional calcium silicate hydrate that is very similar to the C-S-H gel formed from Portland cement hydration. This process is called pozzolanic reaction in cement chemistry. The additional C-S-H gel produced can contribute to the improved early and late age strength and durability of concrete. The different compositions between UHPC and ordinary Portland cement paste are expected to cause differences in the hydration mechanisms for these two materials.

To study the hydration differences between Portland cement paste and UHPC, ordinary cement paste with a w/c ratio of 0.60 and UHPC with the same mix proportion as Williams et al. (2009) were studied with Raman Spectroscopy. RS analysis was applied to these two materials at the hydration ages from 3 to 28 days. In this work, the pozzolanic reaction of silica fume can be detected with the consumption of CH during the UHPC hydration. This result enhances the potential for expanding RS to study various types of materials.

5.2 Materials and Sample Preparation

5.2.1 Raw Materials

For the ordinary paste (w/c=0.6), Type I Portland cement was used. The chemical compositions and particle size distribution of this cement were given in *Section 4.2*.

For the UHPC, Class H cement (oil well cement specified by American Petroleum Institute (API)), processed fine silica sand, finely ground silica flour, and silica fume were used. The chemical compositions of these components are list in Table 5.1, which were gained by XRF analysis. It can be seen from the table that silica sand and flour have the similar compositions and they mainly contain silicon dioxide (99.20% and 98.87%). The silica fume has less content of SiO₂, but still higher than 90%.

Table 5.1 Chemical compositions of Class H cement, silica sand, silica flour, and silica fume

Compound (%)	Class H	Silica Sand	Silica Flour	Silica Fume
SiO ₂	21.75	99.20	98.87	93.00
Al ₂ O ₃	2.73	0.07	0.25	0.59
Fe ₂ O ₃	4.43	0.05	0.03	0.72
CaO	64.25	0.17	0.19	1.29
MgO	2.35	0.06	-	0.17
SO ₃	2.85	0.01	0.02	0.13
Na ₂ O	0.09	-	-	-
K ₂ O	0.17	-	0.01	0.02
Na ₂ O _{eq}	0.20	-	-	-

Based on the oxides percentages in Table 5.1, the mineral compositions of Class H cement were calculated according to Bogue's equations (Neville, 2010), which is shown in Table 5.2. It can be found from this table that the content of C₃A in this cement is not significant enough to be detected by XRF analysis. The lower amount of aluminate can contribute to the durability of UHPC. This is because the C₃A hydration produces ettringite (Eq. (2.7)), which is expansive at the presence of water. After concrete hardened, this expansion can lead to cracking in the concrete matrix, increasing the permeability of the concrete to detrimental chemicals, such as sulfates and carbonates.

Compared with the compositions in Type I Portland cement (Table 4.2), the content of C_2S and C_4AF are higher in Class H cement. There is not a significant difference of C_3S concentration in the two types of cement (64.62% in Type I cement and 63.24% in Class H cement).

Table 5.2 Mineral compositions of Class H cement

Clinker Phase	Weight, %
C_3S	63.24
C_2S	14.65
C_3A	N/A
C_4AF	13.27

5.2.2 Sample Preparation

For the UHPC, the mix proportion is listed in Table 5.3 (Williams et al., 2009). During mixing, the four constituent materials were dry mixed for about 5 minutes. And then water and superplasticizer were combined before being gradually added to the dry mixture while actively mixing. Mixing time was approximately 15 minutes to achieve a wet, flowable paste. After this, steel fibers were added to the mixture and the concrete was then allowed to mix for another 10 more minutes. When mixing was done, UHPC was transferred to the standard tissue culture dishes (*Section 4.3*) and slightly tapped to give a relatively smooth surface. The sample holders were covered till the samples were hardened.

For the ordinary cement paste, mixing procedures as described in *Section 4.3* were followed. After mixing, paste was then transferred to sample holders with slightly tapping and then covered till hardened.

For both UHPC and ordinary paste, after hardening, the samples were cured in water at the temperature of 20 °C without covers till the hydration ages of 3, 7, 14, 21, and 28 days. At each age, three specimens for each material, cement paste and UHPC, were taken out from the curing tank to be prepared for RS analysis.

Table 5.3 UHPC mix composition (Williams et al., 2009)

Materials	Product	Proportion by Weight
Cement	Lafarge, Class H, Joppa, MO	1.00
Silica Sand	US Silica, F55, Ottawa, IL	0.967
Silica Flour	US Silica, Sil-co-Sil 75, Berkeley Springs, WV	0.277
Silica Fume	Elkem, ES 900 W	0.389
Superplasticizer	W.R. Grace, ADVA 170	0.0171
Water (tap)	N/A	0.208
Steel Fibers	Bekaert, Dramix® ZP305	0.310

5.3 Raman Measuring Procedures

The Raman system used was the same as in the study of fresh cement paste described in *Section 4.4*, including the excitation source, range of Raman shifts, exposure time, objective, calibration, and acquisition software, etc. All the spectra for Portland cement paste and UHPC were acquired with the same experimental parameters. For these two materials, RS analysis was applied at 10 discrete points for each sample and each spectrum gained was corrected with the background subtraction (*Section 4.5.2*). At each designated hydration age, 3 samples were tested. The average of the total 30 spectra after background corrections was used as the representative pattern.

5.4 Results and Discussion

5.4.1 Comparison between Spectra for Type I and Class H cement

In ordinary paste, Type I cement was used. While in UHPC, class H cement was used. The difference in the raw cement types will lead to different hydration mechanisms in the two materials. Therefore, RS analysis was firstly applied to compare the two cements that were used. Fig. 5.1 shows the Raman spectrum for Class H cement. The pattern for Type I cement was also included in the figure for comparison purpose. The phases in both patterns are identified based on the peak assignments in Table 3.1. Comparing the two patterns, it can be seen that the peaks for C_3S , C_2S , and gypsum can be identified clearly in both cements, which are at the Raman shift of 833, 887 and 1005 cm^{-1} , respectively. The peak intensity of gypsum is higher in UHPC than that in Type I Portland cement. The most significant difference regarding the two patterns lies in the identification of C_3A peak. In the pattern for Type I cement, the peak for C_3A is characterized at the shift of around 552 cm^{-1} . However, in the Class H cement, the corresponding peak cannot be separated from the overlapped shift range of C_3A and C_4AF . This result is consistent with the XRF analysis applied to identify the compositions of both cements. The lower content of C_3A in Class H cement (Table 5.2) than Type I Portland cement (Table 4.2) generates weaker peak that is easily to be obscured by C_4AF peak.

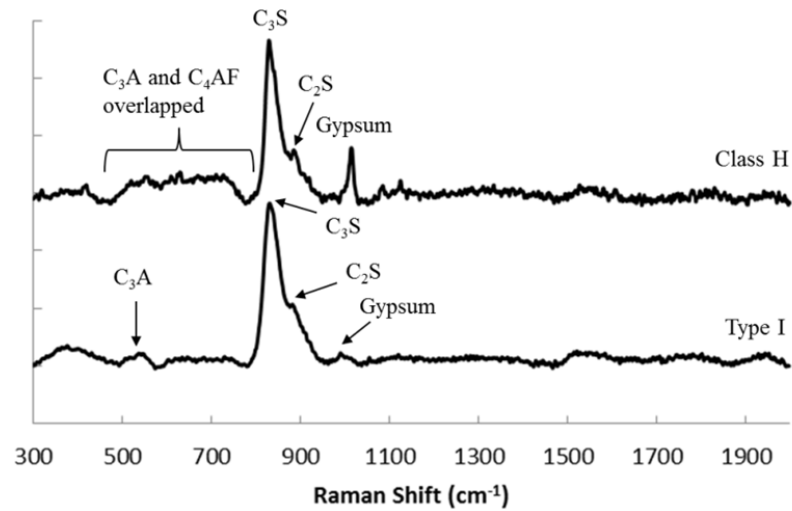


Fig. 5.1. Raman spectra for Class H and Type I cements

5.4.2 Characterization of Silica Components in UHPC

Besides Class H cement, silica components were also included in the UHPC. The characteristic peaks for these silicas can serve as the references in identifying each individual silica component in the hydrated UHPC. With RS analysis on these silicas, it is noted that although they are all primarily composed of silicon dioxide, but they can still be distinguished according to their individual spectral features. Fig. 5.2 shows the Raman patterns for silica flour, silica sand, and silica fume, respectively. By comparing Fig. 5.2(a) and (b), it is observed that both the silica flour and silica sand have a strongest peak at 465 cm^{-1} . This peak is characterized for quartz (SiO_2) (Guedes et al., 2008; Garg, 2012). Quartz is stable in nature and does not participate in the cement hydration. It is also seen from these two patterns that silica flour has other two strong peaks at 1371 and 1397 cm^{-1} , which cannot be found in the spectrum of silica sand. It should be noticed that, these two peaks are not present in the pattern for silica fume (Fig. 5.2(c)), either.

Therefore, these two peaks can be taken as the characteristic peaks for silica flour. For silica fume, its pattern has a unique, strong peak at 517 cm^{-1} , which can also be assigned to silicon dioxide. The different shift positions of strongest SiO_2 peak in silica flour/sand (465 cm^{-1}) and silica fume (517 cm^{-1}) should be attributed to the differences in their atomic structures. Silica flour and sand are crystalline materials, while silica fume is an amorphous material that does not have an overall structure.

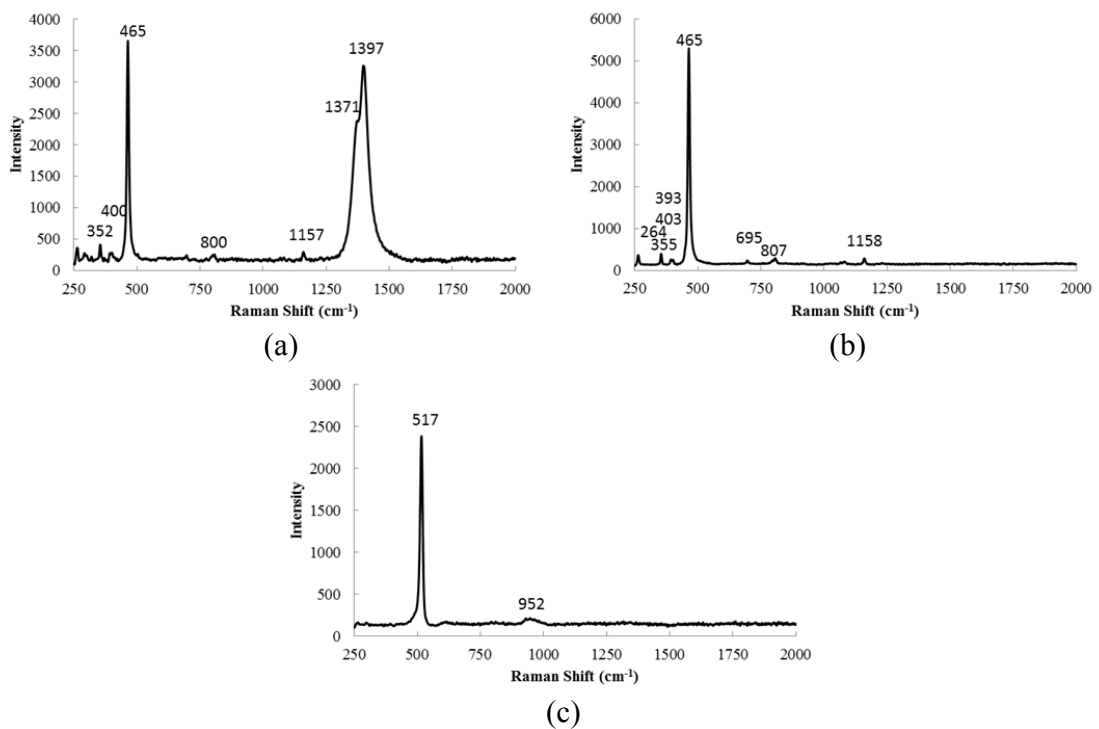


Fig. 5.2. Raman spectra for silica components in UHPC: (a) silica flour; (b) silica sand; (c) silica fume

5.4.3 Portland Cement Paste at 3-28 days

To study the hydration processes of ordinary Portland cement paste and UHPC, the RS analysis was conducted on both materials at hydration ages from 3 to 28 days. Fig. 5.3 stacks Raman spectra obtained from the ordinary paste with a w/c ratio of 0.60. From

these patterns, calcium silicates (C_3S and C_2S), ettringite, and CH are consistently found at all the hydration ages. For calcium silicates, different from the paste hydrating for 20 minutes (Pattern B in Fig. 4.4), the peak intensity for C_2S is always higher than C_3S in the patterns during the measuring framework. This is caused by the higher reactivity of C_3S at the early age, leading to its faster consumption during the first 3 days after mixing. The domination of C_2S in the calcium silicate phases occurred to all the pastes measured. It is also noticeable from the stacked patterns that the intensities of calcium silicates peaks decreased gradually with the increasing hydration ages. On the contrary, as one of the hydration products of calcium silicates, CH increased at the hydration ages from 3 to 28 days. From the figure, one can also see the decreased intensity of ettringite at late age. In all the patterns, the peak for C_3A was not detected, attributing to its reactive hydration at the very early age.

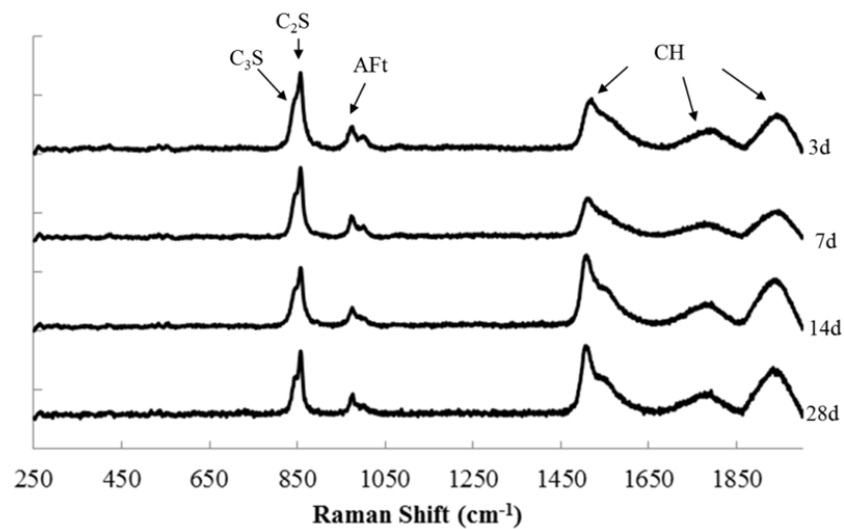


Fig. 5.3. Stacked spectra for ordinary paste with a w/c ratio of 0.60 at the hydration ages from 3 to 28 days

5.4.4 UHPC at 3-28 days

Fig. 5.4 depicts the spectrum for UHPC hydrated for 3 days. The pattern for the ordinary paste at this hydration age was also displayed in the figure. According to the spectrum for UHPC, both the cement paste components and silicas can be recognized easily. The paste components found in the UHPC had the same peak positions as those in the ordinary paste. These included calcium silicates (C_3S & C_2S), ettringite, and calcium hydroxide (CH). But these peaks were also noted to be much weaker in the UHPC than in the ordinary paste. This is due to the less amounts of cement used in UHPC (Table 5.3). It is also noticeable from the UHPC pattern that the peak for silica fume has a higher intensity than both silica flour and silica sand, although the amount of silica fume was less. This may be due to the fact that silica fume is more easily to be detected by RS which is a surface measurement. As a very fine powder, it is easier for silica fume to be distributed on the surface of the UHPC.

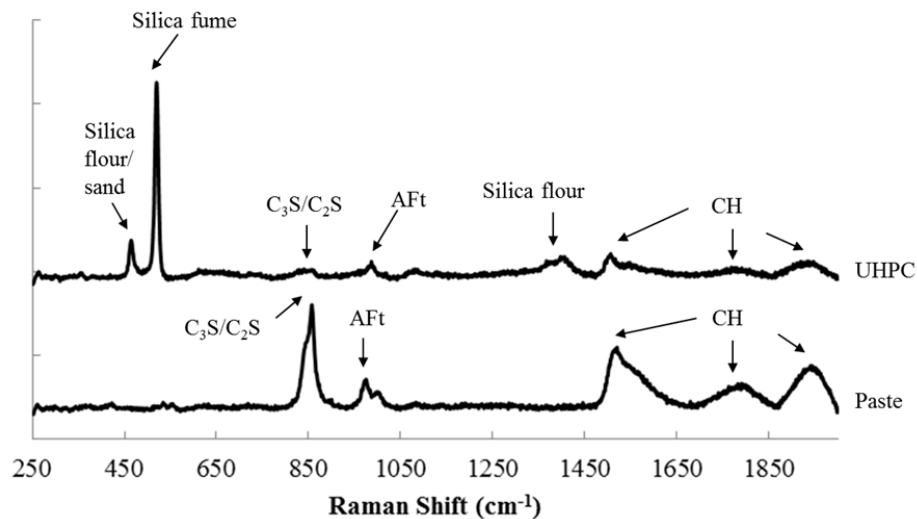


Fig. 5.4. Spectra comparison between UHPC and ordinary paste hydrated for 3 days

Similar to the Portland cement paste, the Raman spectrum collected from the UHPC was also stacked to explore its hydration behavior. Fig. 5.5 illustrates the patterns for UHPC at different hydration ages. By comparing these patterns, one can notice that the peaks found for UHPC in Fig. 5.4 are present consistently at all the hydration ages. The predomination of silica fume peak over the other components happened to all the measured UHPC. Because of this intensive peak for silica fume, the changes of UHPC components at the different hydration ages were not able to be characterized visually. Quantitative analysis on the peaks for these components thus was applied, which will be illustrated in the following discussions.

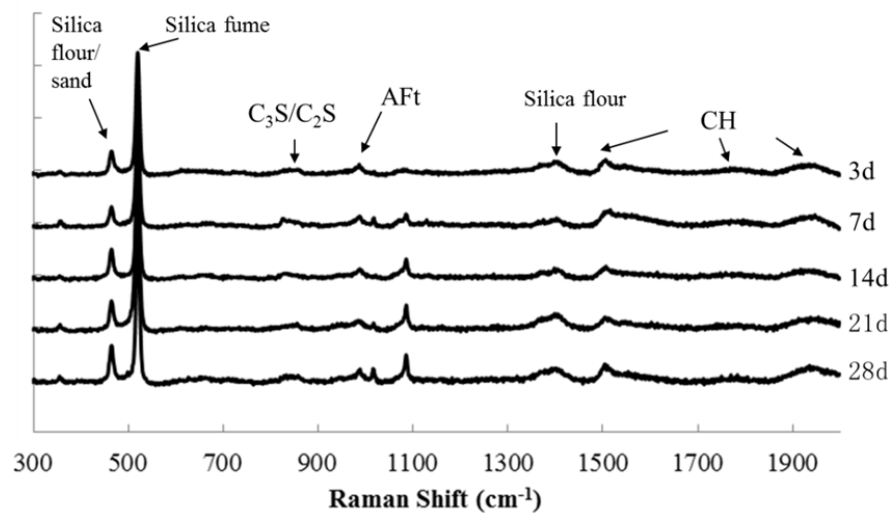


Fig. 5.5. Stacked spectra for UHPC at the hydration ages from 3 to 28 days

5.4.5 Quantitative Analysis of Ordinary Portland Cement Paste

The predomination of silica fume peak in the UHPC patterns shielded difficulties in tracking the peak intensity changes of other components, thus the quantitative analysis was focused on tracking the peak area during the hydration process. According to other

researchers, both the peak intensity and peak area can reflect the concentration of the species investigated in the samples (Strommen and Nakamoto, 1984; Tarrida et al., 1995; Vagenas and Kontoyannis, 2003; Skorda and Kontoyannis, 2008; Simone et al., 2014). The same quantitative analysis was also applied to the ordinary pastes. By comparing the analysis results from both materials, the differences in their hydration mechanisms can be revealed.



Fig. 5.6. Evolution of peak area for calcium silicates in the ordinary paste at the hydration ages from 3 to 28 days

For ordinary cement paste ($w/c=0.6$), quantitative analysis was applied to the peaks for calcium silicates (C_3S+C_2S), CH and ettringite. For each Raman pattern, the gained peak area for each component was divided by the sum of peak areas for the total three compounds from the same pattern. The averaged quotient from the 3 samples (30 patterns) at each age was further normalized to the maximum averaged value obtained at all the hydration ages. Fig. 5.6 shows the evolution of peak area for calcium silicates of ordinary paste attained by this analysis method. According to this figure, the amount of

calcium silicates is decreasing at the increased hydration age, especially during the first two weeks. This is caused by the more reactive hydration of calcium silicates (mainly C_3S) at the early age (Taylor, 1997). The decreasing trend of the peaks was almost terminated after two weeks. This may be due to the fact that the hydration of C_2S controls the reaction of calcium silicates, and the C_2S reaction is known to be much slower than C_3S .

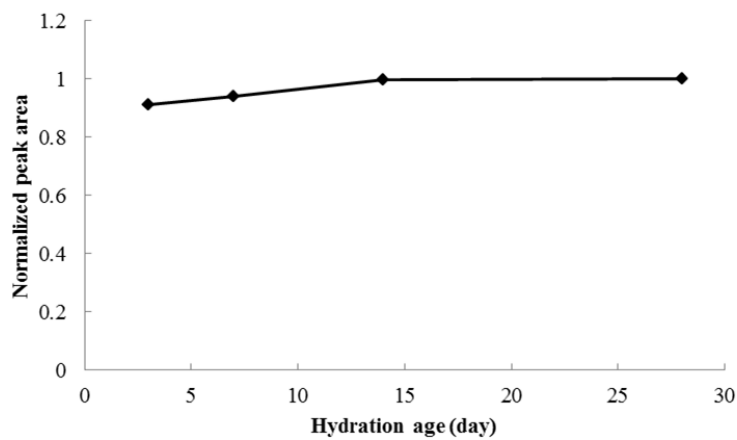


Fig. 5.7. Evolution of peak area for calcium hydroxide in the cement paste hydrated for 3 to 28 days

Fig. 5.7 exhibits the quantitative analysis results of the peak area for calcium hydroxide in the cement paste. By comparing Figs. 5.6 and 5.7, it can be seen that the evolution of CH was corresponding to that of calcium silicates. This is because CH is produced from the hydration of calcium silicates (Eqs. (2.5) and (2.6)). With the faster consumption of (C_3S+C_2S) at the first two weeks, the relatively rapid increasing of calcium hydroxide during this period was also observed. The approximately constant

peak area for CH at late age can be the result from the dominated, slower C_2S reaction after paste hydrated for more than 2 weeks (Fig. 5.6).

The evolution of ettringite peak area in cement paste was displayed in Fig. 5.8. It is apparent from the figure the content of ettringite remains almost constant from 3 days to 7 days and then it decreases rapidly till 14 days. Thereafter, ettringite content is constant again. Combining with the discussion on the ettringite intensity change during the setting period in *Section 4.7.4*, the decreased content may be caused by the conversion of ettringite to monosulfate.

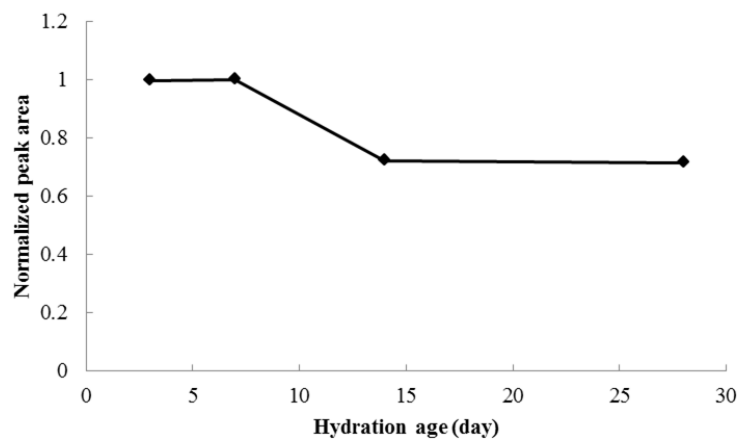


Fig. 5.8. Evolution of peak area for ettringite in the cement paste hydrated for 3 to 28 days

5.4.6 Quantitative Analysis of UHPC

Quantitative analysis on peak area was also applied to the UHPC to investigate the evolutions of the components at different hydration ages. But the normalization method adopted was different. It has been mentioned that UHPC incorporated three silica components, i.e., silica sand, silica flour and silica fume. Among these silicas, only the

silica fume can react with calcium hydroxide in the presence of water during hydration (Section 5.1). Thus the peak area of (silica flour + sand) was assumed to be constant at the different ages. Therefore, instead of normalizing to the sum of the peak areas for all the analyzed compounds in cement paste, the peak area of each component was normalized to the peak area of (silica flour + silica sand) for each pattern. After this, the averaged quotient from the 3 samples (30 patterns) at each age was further divided by its maximum value obtained at all the hydration ages. This method was applied to the peaks for silica fume, C_3S+C_2S , CH, and ettringite in the UHPC patterns. Fig. 5.9 displays the gained evolution curve for silica fume by the quantitative analysis. The faster decreasing of silica fume during the first two weeks is observed from the figure. This may be attributed to the fact that silica fume is ultrafine powder and it can react quickly at the very early age during cement hydration. The observed decreasing trend nearly ceased at the ages later than two weeks, which can be caused by the less amount or decreased reactivity of silica fume at these ages.



Fig. 5.9. Evolution of peak area for silica fume in UHPC at the hydration ages from 3 to

28 days

Fig. 5.10 shows the evolution of calcium silicates in the UHPC. From this figure, the decreased content of calcium silicates is seen at the increased hydration age. Compared to the evolution of calcium silicates in ordinary cement paste (Fig. 5.6), the decreasing trend was not so obvious in UHPC, which was caused by the less amount of cement in the concrete.



Fig. 5.10. Evolution of peak area for calcium silicates in UHPC

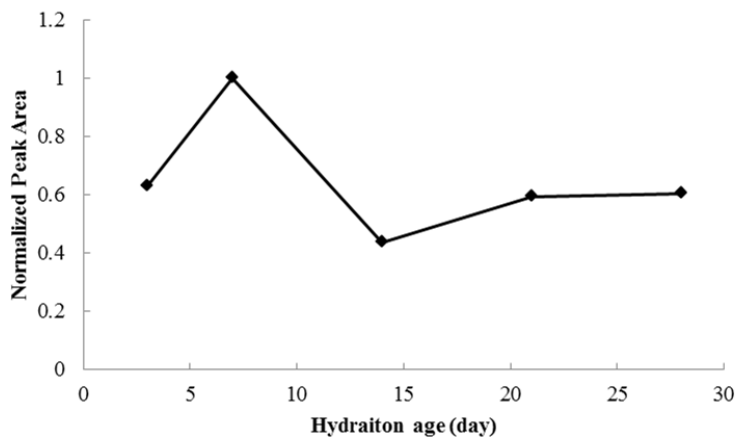


Fig. 5.11. Evolution of peak area for CH in UHPC

The evolution curve for CH in the UHPC is shown in Fig. 5.11. This curve shows the increased CH content during the first week after mixing. Thereafter, the content decreased till 14 days and then it only increased slightly. The increased amount at the early age is due to the hydration of calcium silicates, producing more CH, while the decreased CH during 7 to 14 days can be attributed to its faster consumption by silica fume than the formation from calcium silicates hydration. The lower reactivity of both calcium silicates and silica fume after 14 days led to the only slightly increased CH during this period.

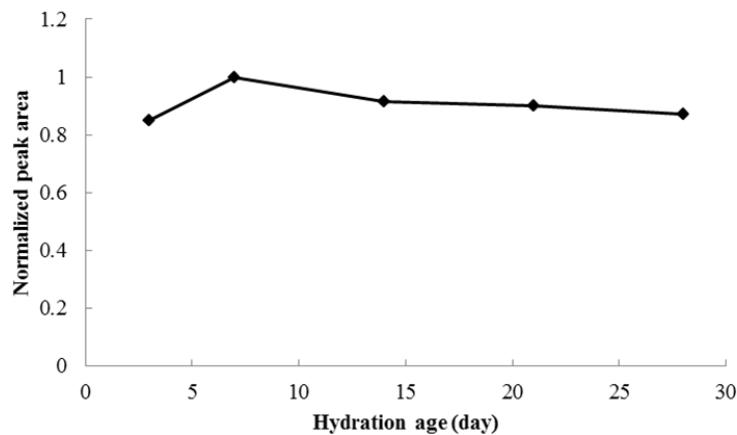


Fig. 5.12. Evolution of peak area for ettringite in UHPC

In Fig. 5.12, the evolution curve for ettringite in UHPC is shown. Comparing this curve to the evolution of ettringite in the Portland cement paste (Fig. 5.8), it can be seen that ettringite had the similar trend regarding its peak area in both materials. Its peak area started decreasing rapidly at 7 days and it only changed slightly after 14 days. But the overall changes of ettringite in the UHPC were less obvious than in ordinary paste. This may be due to the less C_3A content in UHPC, producing less amount of ettringite.

5.5 Conclusions

The study described in this work shows that the Raman spectroscopy is a promising method for investigating the differences in the hydration process of Portland cement paste and UHPC. In particular, the following conclusions can be drawn:

- (1) RS is capable of characterizing the main constituents in Class H cement, including C_3S , C_2S , and gypsum.
- (2) Different types of silica components used in UHPC can also be characterized based on their individual spectral features.
- (3) From the quantitative analysis on peak areas, silica fume was found to be more reactive during the first two weeks.
- (4) Calcium silicates decreased with increased hydration age in both materials, but this decreasing trend was more obvious in the ordinary paste than in the UHPC.
- (5) CH was also detected in the two materials. In ordinary paste, its amount increased with ages. However, in the UHPC, its amount decreased after 7 days due to its consumption by silica fume.
- (6) Detection of ettringite showed the similar trend of peak area changes in the two types of materials. It started to decrease rapidly from 7 days and only changed slightly after 14 days.

CHAPTER 6

DEVELOPING A PROTOCOL FOR CHEMICAL MAPPING STUDY ON HARDENED PASTE

6.1 Introduction

In the previous two chapters, RS analysis on the hydration process of fresh and hardened ordinary cement paste and UHPC has been discussed. The results prove this technique an effective tool in identifying the different cement ingredients and hydration products in both materials. In the following two chapters, RS is applied to explore microstructure development of cement paste at late ages. This can be achieved by the RS chemical mapping, which provides visual images of the distributions and connections of chemical components in cement paste.

RS chemical mapping has been widely used in the food and pharmaceutical industries (Zhang et al., 2005; Belu et al., 2008; Fischer et al., 2009; Gorden et al., 2011). However, there is little work done with this technique in cement chemistry. Jallad et al. (2001) studied thaumasite formation in the sulfate-attacked mortar. From their study, the distribution of gypsum and thaumasite can be found from the obtained chemical maps. The chemical mapping study on the Portland cement paste has not yet been implemented.

The objective of this chapter is to develop a protocol of chemical mapping, so that the obtained map reflects correctly the dispersion, concentration, and connection of chemical ingredients in cement paste. To achieve this goal, a hardened self-consolidating concrete (SCC) paste spared from another research project was used.

6.2 Raman Measuring Procedures

The RS system used was similar to the studies described in the previous chapters (Chapters 4 and 5), including the same excitation source, range of Raman shifts, exposure time, objective, calibrations, and acquisitions software, etc. The only difference regarding the RS system setting was the slit opening. It was increased from 20 μm (default) for spectra analysis to 50 μm for chemical mapping. The increased slit opening is able to improve the signal to noise (S/N) ratio for Raman spectra, but the acquisition time was also increased slightly.

For the preliminary study, chemical mapping was carried out on an area of $20 \times 20 \mu\text{m}^2$ having a total of 100 points spreading in a grid matrix on the sample surface, shown as in Fig. 6.1. The grid size was set based on the size of the laser spot (4 μm). This is to ensure that the whole area can be measured continuously. After setting up the measuring area, Raman spectrometer collected spectra sequentially from point 1 to point 100. Thus from one mapped area, there were 100 spectra acquired. It took around 90 minutes to map the whole area.

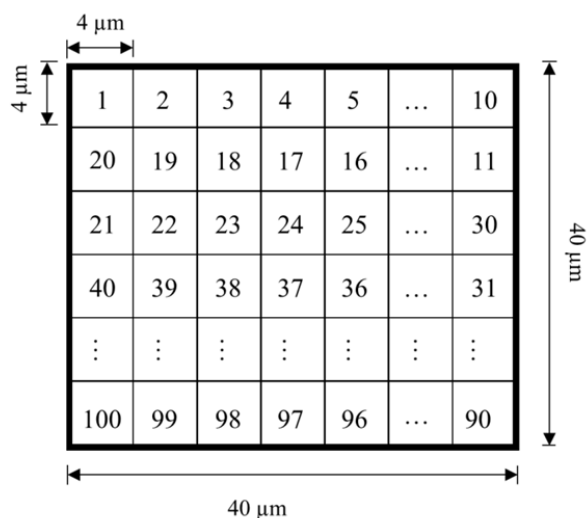


Fig. 6.1. Mapping setup for analyzing an area on the sample surface

6.3 Chemical Mapping Methodologies

In chemical mapping, once the spectra of all measured points are obtained, the map can be constructed with different analysis methods. Of those methods, the main three suitable to be used without peak fitting are mapping with peak intensity, peak area, and direct classical least squares components analysis. Peak intensity and peak area can reflect the concentration of the species investigated in the samples. The underlying technique used in components method is direct classical least square fitting of the obtained Raman spectrum to a linear combination of the studied components spectra in the sample. To find the best fit for paste analysis, all of the three methods were tried on the SCC paste specimens. The detailed mapping results are shown and discussed in the following sections.

6.3.1 Mapping with Peak Intensity

(a) Mapping the Acquired Raman Spectra

Before constructing chemical images by mapping with peak intensity, the acquired Raman spectra need background subtraction (*Section 4.5.2*). This is because background signals can contribute significantly to the intensity of all the characteristic peak(s). After background correction, the chemical maps for each individual paste component can be constructed by the mapping function called “intensity at a point” embedded in the WiRE3.3 software. The intensity at the shift of 465, 853, 989, and 1510 cm^{-1} were mapped to create chemical images for C-S-H gel, calcium silicates, ettringite, and CH, respectively. These shifts located approximately at the center of the respective characteristic peaks. It should be noticed that after being hydrated for 1 year, the peak for C-S-H gel at 625 cm^{-1} in the fresh cement paste (*Section 4.7.2*) was undetectable. This may be due to the morphology and structural changes of this hydration product with the undergoing hydration (Bensted, 1976). In addition, CH had multiple peaks at 1400 to 2000 cm^{-1} , of which the one with the highest intensity (1510 cm^{-1}) was taken as the characteristic peak during the mapping procedure.

To distinguish different phases in the cement paste by chemical mapping, each studied component was assigned with a different color. Colors red, yellow, green, and blue were representing C-S-H gel, calcium silicates, ettringite, and CH, respectively. Fig. 6.2 shows the dispersion for C-S-H gel by mapping the intensity at 465 cm^{-1} over the mapped area (100 spectra). In the figure, the brightness of the color corresponds to the intensity of the peak. For example, point #53 is brightest, since the intensity of the C-S-H

gel peak in this point is higher than all other points. By looking at the map, one would think point #36 also has a high intensity of C-S-H gel peak and point #52 may have a very low intensity of C-S-H gel, simply because the brightness of point #36 is higher than point #52. However, this does not reflect the truth when looking at the spectra obtained from these two locations. Fig. 6.3 plots the spectra for point #36 and #52. From Fig. 6.3(a), one can see that there is actually no peak at the shift of 465 cm^{-1} , but the absolute value of the intensity is very high (it has a value of 1098 at 465 cm^{-1}). In Fig. 6.3(b), a clear peak at 465 cm^{-1} with an intensity of 577 can be easily identified. Simply due to the absolute values in the intensity, the software misleads the conclusion that #36 had a high concentration of C-S-H gel. The phenomenon also occurred to some other positions in the map (Fig. 6.2) and to the maps for the other three paste components. Since the intensity variances among different points can be tremendous, it can be affected by the degree of focusing, physical properties of the sample surface, the RS system alignment, etc. To get a chemical map more fitting to the real concentration of the components, normalization should be applied to decrease or eliminate the intensities differences among different points caused by the external factors other than the tested material itself.

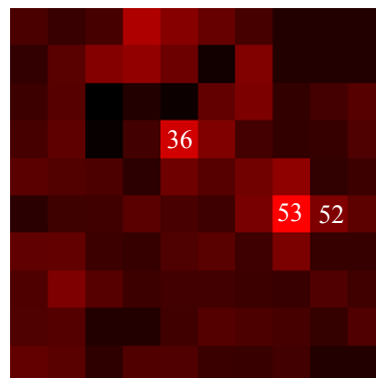


Fig. 6.2. Chemical map for C-S-H gel gained by mapping the intensity at 465 cm^{-1}

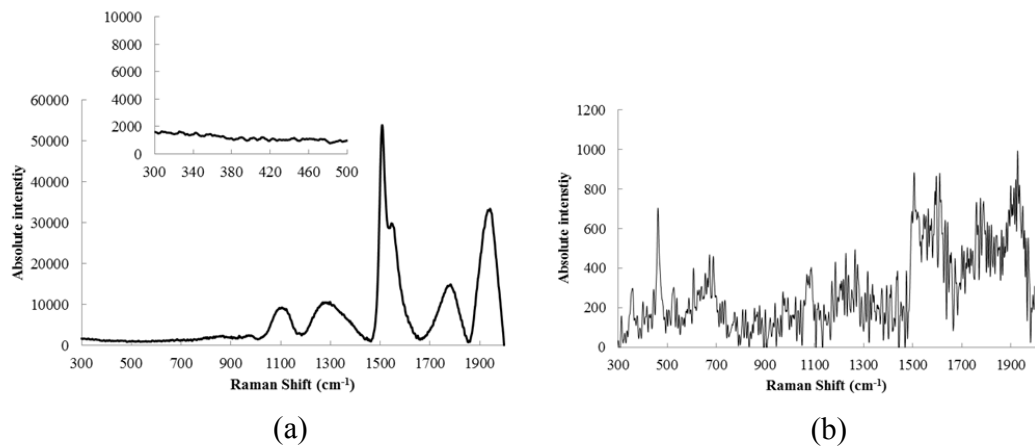


Fig. 6.3. Raman spectra gained from point (a) # 36 and (b) #52

(b) Mapping with Normalized Raman Spectra having Same Intensity Range

There are total 3 normalization methods that were tried to normalize the Raman spectrums with the WiRE3.3 software. The spectra can be normalized to have the same intensity range, have the same integrated signal, or have the same mean and variance. Normalizing to the same intensity range means that the intensity values of each spectrum is multiplied by a number so that all the spectrums have the same lower and upper limits. The number is normally different for different patterns. The values set for the two limits in this study are 0 and 6000. There was no specific requirement on setting the limits, only if the normalized intensities for the peaks were sensitive enough to be differentiated by chemical mapping. Fig. 6.4 shows an example of the resulted spectra after pattern #36 and #52 (Fig. 6.3) normalized with this method. By comparing Figs. 6.4 and 6.3, it can be seen that the shape of the two spectra did not change after being normalized. Only the intensity range for these two spectra was adjusted. It is also found from this figure that with the same intensity range, intensity of the C-S-H gel peak at 465 cm^{-1} in the #52 pattern is higher than the intensity at the same shift in the #36 pattern. The new C-S-H gel

image is shown in Fig. 6.4. From this map, it can be seen that point #36 is much darker than point #52. This is consistent with the C-S-H gel detection with the RS for these two points.

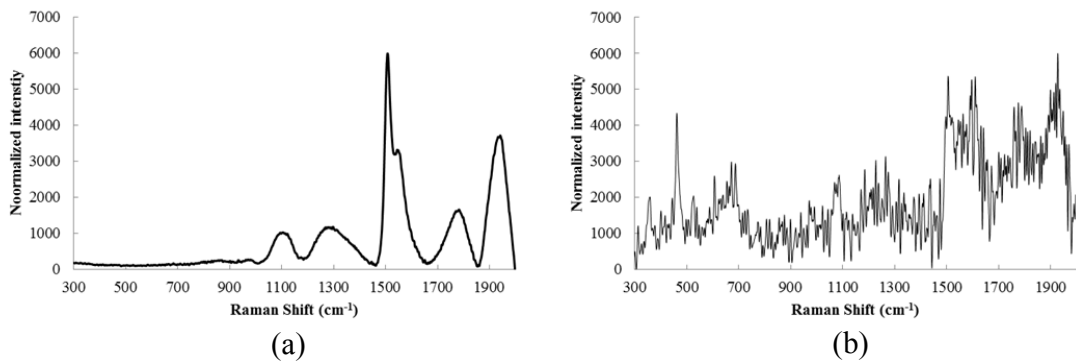


Fig. 6.4. Spectra after normalized to the same intensity range of 0 to 6000: (a) #36; (b)

#52

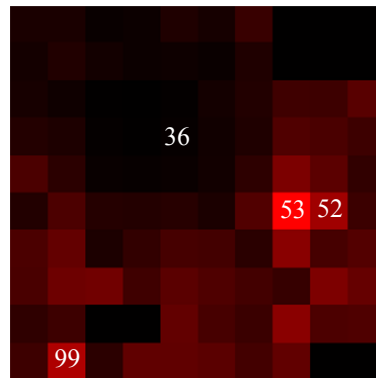


Fig. 6.5. Chemical map for C-S-H gel gained after the Raman data normalized to the same intensity range of 0 to 6000

Closer checking of the new C-S-H gel image (Fig. 6.5) reveals difficulties with this normalization method in mapping the points that do not contain any peak. Take the point #99 as an example. The background subtracted and normalized spectra are shown in

Fig. 6.6. From Fig. 6.6(a), there is no obvious peak identified from this location and the intensity values in the pattern do not vary significantly. After normalized, the intensity at 465 cm^{-1} in point #99 (3899) is higher than that in point #52 (3608), leading to its higher brightness in the C-S-H gel map (Fig. 6.5). Therefore, this normalization method did not work effectively for the chemical mapping with peak intensity, especially when mapping the points without any component peak.

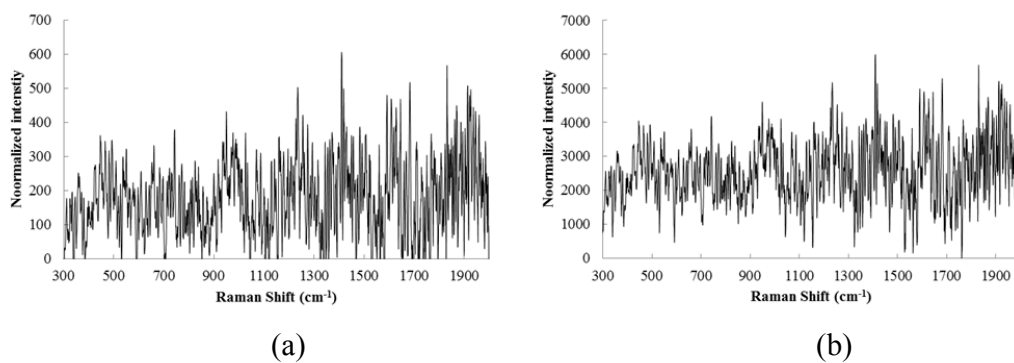


Fig. 6.6. Spectra from point #99 in the mapped area: (a) acquired; (b) normalized to have the intensity range of 0 to 6000

(c) Mapping with the Normalized Raman Spectra having Same Integrated Signal

Another normalization method regarding the integrated signal was also tried for the chemical mapping. This method is to proportionally modifying the intensity value so that the sum of all values in each given spectrum is a same constant K . The value for K was 10000 in the current study. There is no detailed requirement on setting K value. The application of this method provided a good chemical map for C-S-H gel, which can reflect its real distribution. This same method was also applied to map the calcium silicates and CH. From their maps, the problems in mapping the points without any peak as discussed for point #99 in Fig. 6.5 was also found. The brightness of the point only

containing noise was higher than the points having real peaks. Take the obtained map for calcium silicates as an example, which is shown in Fig. 6.7. It can be seen from this map that point #72 is brighter than #58, suggesting the higher intensity at the shift of 853 cm^{-1} in point #72. Fig 6.8 shows the two spectra for these two points. It is apparent from Fig. 6.8(a) that there is no calcium silicates peak detected from point #72. Only two of the acquired spectra in the mapping area contained calcium silicates peaks, i.e., point #58 (Fig. 6.8 (b)) and #55. Thus mapping the paste with Raman spectra having the normalized integrated signal, was not able to provide the correct chemical images as well.

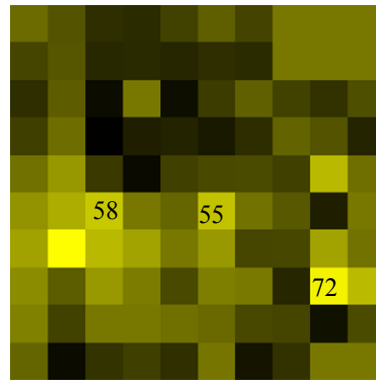


Fig. 6.7. Chemical map for calcium silicates gained after the Raman data normalized to have the same integrated signal of 10000

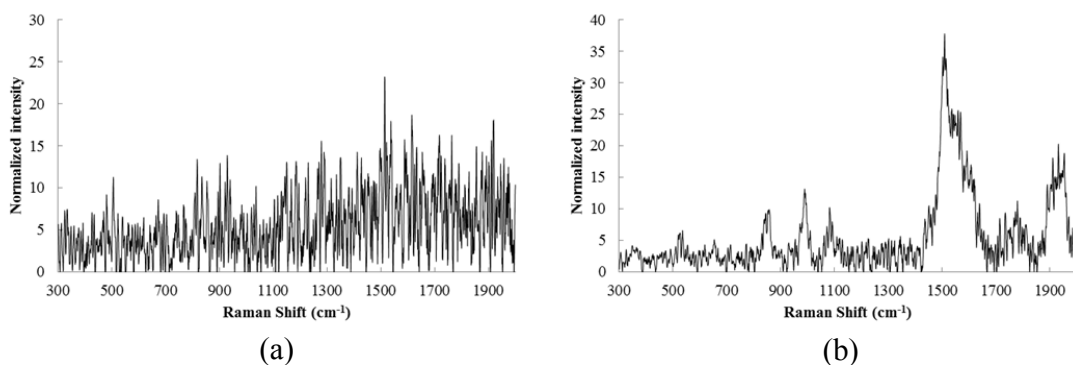


Fig. 6.8. Spectra after normalized to the same integrated signal: (a) #72; (b) #58

(d) Mapping with the Standardized Raman Spectra

The last normalization method in the acquisition software is to modify the intensity value so that each spectrum has the same mean and variance. With the respective value for mean and variance set as 0 and 1 in the current study, this method can also be called “standardization”. The standardization of the intensities in a spectrum can be explained by the following equation.

$$x' = \frac{x - \bar{x}}{\sigma} \quad (6.1)$$

where x , \bar{x} , σ and x' are the original, mean, standard deviation, and reproduced value of the intensity in each spectrum, respectively. By applying this equation, the variances between each intensity value and mean intensity were displayed as the new spectrum.

Fig. 6.9 shows the calcium silicates map from the same area as previous images (Figs. 6.2, 6.5, and 6.7) after standardizing the 100 spectra. By looking at this figure, it can be found that the brightness of point #72 is still the highest among all the points, but no calcium silicates peak was detected in this location (Fig. 6.8(a)). As a result, it is reasonable to conclude that mapping the standardized Raman spectra has the same problem in the points without any peak, as encountered in the two previously discussed normalization methods, i.e., normalizing the spectra to have same intensity range or same integrated signal. In all these three methods, the brightness of the points did not correspond correctly to the Raman detections.

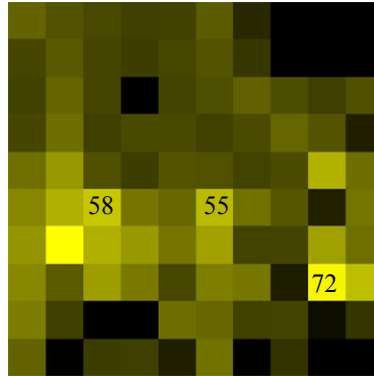


Fig. 6.9. Chemical map for calcium silicates gained after the Raman data normalized to have the mean of 0 and variance of 1

From these discussions, it can be seen that chemical images constructed by the peak intensity with or without normalization methods cannot reflect the real locations of the components in the paste. For those points without any peak, they are possible to have higher brightness than those having relatively strong peaks. This may mislead the mapping analysis, therefore, mapping with peak intensity was not adopted in this research.

6.3.2 Mapping with Peak Area

Different from mapping with peak intensity, mapping with peak area does not require the acquired spectrums to be background subtracted. This is because the peak area values are obtained by calculating the area between the peak and the baseline for the corresponding peak. This can dramatically reduce the data processing for constructing a map, especially when large areas with hundreds or even thousands of spectra are mapped. In this research, the area under shift range of $447\text{-}483\text{ cm}^{-1}$, $823\text{-}880\text{ cm}^{-1}$, $962\text{-}986\text{ cm}^{-1}$, and $1467\text{-}1670\text{ cm}^{-1}$ were mapped for C-S-H gel, $\text{C}_3\text{S}+\text{C}_2\text{S}$, ettringite, and CH, respectively. These shifts ranges were set to include the whole peak of each studied component.

Similarly to the mapping with peak intensity, colors red, yellow, green, and blue were assigned to C-S-H gel, calcium silicates, ettringite, and CH, respectively. By comparing the obtained maps for these components from the same area as shown in the previously discussed chemical images, CH was found to dominate the measured area. Thus the following discussions of the mapping with peak area are primarily based on the CH maps. Fig. 6.10 shows the chemical image for CH by mapping the peak area at the shifts from 1467-1670 cm^{-1} . A bright area consisting of 5 points is noticed from this image, i.e., point #23, #24, #36, #37, and #38. These points are brighter because they contain higher concentration of CH. Fig. 6.11 shows a representative spectrum for these points, from point #38. It can be seen from this spectrum that point #38 contains pure CH only.

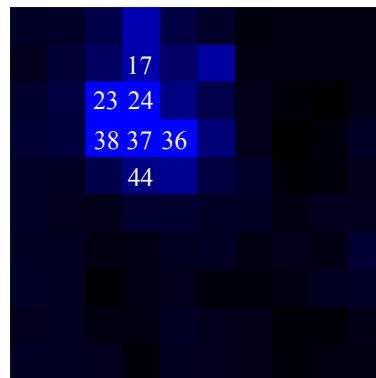


Fig. 6.10. Chemical map for CH gained by mapping the peak area at the shift of 1467 to 1670 cm^{-1}

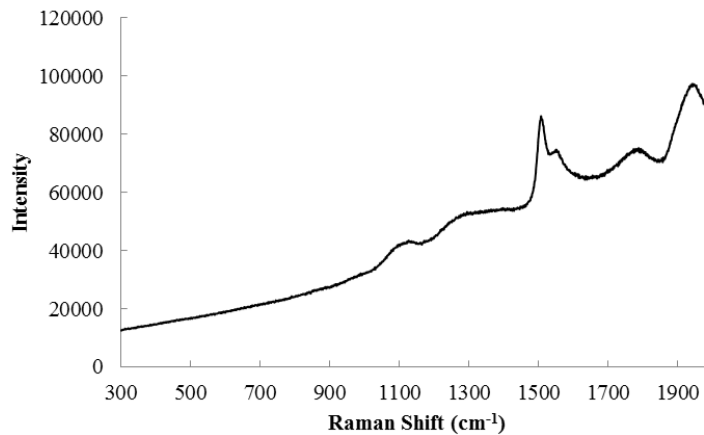


Fig. 6.11. Raman spectrum acquired for point #38

The examination of the CH images also revealed the similar problem encountered in mapping this area with peak intensity without normalizing the Raman data. The greatly differences in the intensity values for each spectrum caused flaws in mapping the peak area. For example, the brightness of point #17 is higher than #44 in the image. However, from their individual spectrum, the CH peak was found to be weaker in point #17 than in #44. This can be seen from the Fig. 6.12. As illustrated in *Section 6.3.1 part (a)*, the tremendous differences in the intensity values for the acquired spectrums were caused by various external factors. To remove their influences, normalization should be applied.

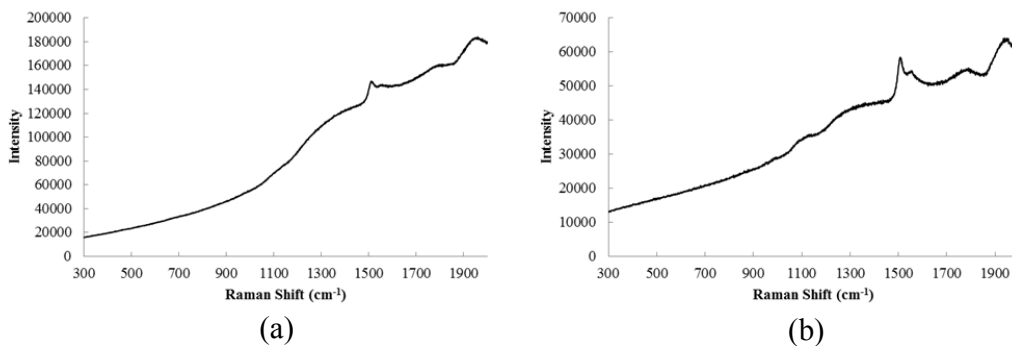


Fig. 6.12. Acquired Raman spectra from point (a) #17 and (b) #44

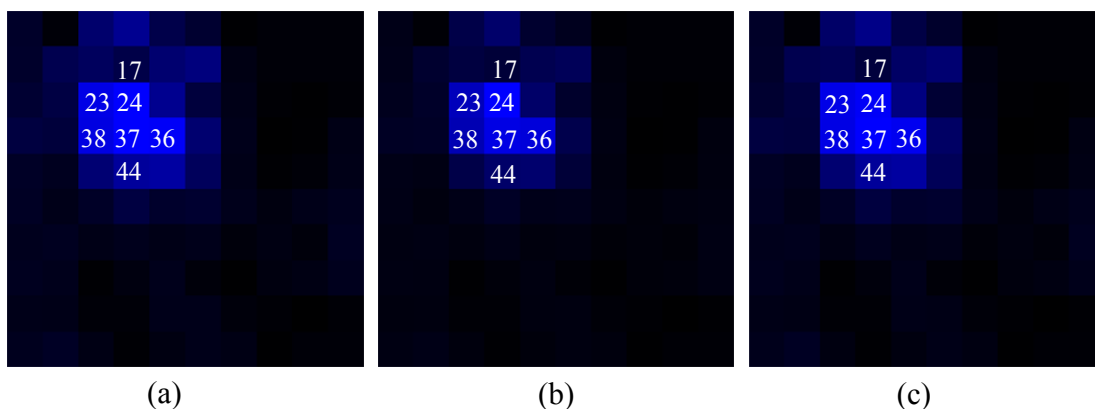


Fig. 6.13. Chemical maps for CH gained by mapping the peak area at the shift of 1467 to 1670 cm^{-1} after: (a) normalizing the spectra to the same intensity range; (b) normalizing the spectra to have the same integrated signal; (c) standardizing the spectra

Normalizing the acquired spectra to have the same intensity range produces the new CH map as shown in Fig. 6.13(a). From this map, point #44 is brighter than point #17. This means that the stronger peak corresponds to the higher brightness and vice versa. By comparing this image with the one produced from acquired Raman spectrums (Fig. 6.10), the correspondence between the brightness and the peak area has been improved.

The other two normalization methods, normalizing the spectra to have the same integrated signal or same mean and variance, were also used. The obtained CH images with these two methods are displayed in Fig. 6.13 (b) and (c). The 5 brightest points seen in Fig. 6.10 can still be observed from these two images, i.e., point #23, #24, #36, #37, #38. For a more clear comparison of these three images in Fig. 6.13, the points without CH peaks should be removed from the figure. This can be achieved by setting peak area threshold, which means the points with peak area lower than the threshold value will not be shown in the map. By checking all the acquired Raman spectrums, the CH peak area

in point #6 was chosen as the threshold for the images. The #6 spectrum is shown in Fig. 6.14. The CH peak in this spectrum is weak, thus it is validated to make an assumption that the spectrums with weaker CH peak than point #6 did not contain CH or only contained neglect amount of CH.

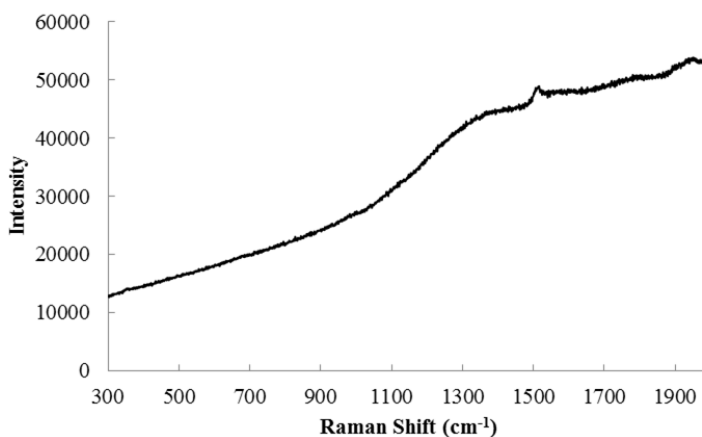


Fig. 6.14. Acquired Raman spectrum from point #6

Fig. 6.15 shows the CH images after the three images in Fig. 6.13 being processed with peak area threshold set as point #6. The differences among the three reproduced images lie in the point #21 and #55. These two points are present in Fig. 6.15(a) and (c), while they are removed from Fig. 6.15(b). Fig. 6.16 illustrates the spectra from the two points. By comparing the peak areas in these two patterns with that in the point # 6 (Fig. 6.14), the three CH peaks are comparably weak and it is difficult to determine which point should be present in the chemical map. To eliminate the uncertainty, only the points with strong CH peaks were studied. These points can be taken as the areas where the CH were concentrated. Fig. 6.17 illustrates the maps only showing the points with strong CH peaks. When creating this map, it is assumed that the points with the stronger CH peak

than point # 38 (Fig. 6.11) were concentrated with CH. The points with concentrated CH were assigned to the same brightness.

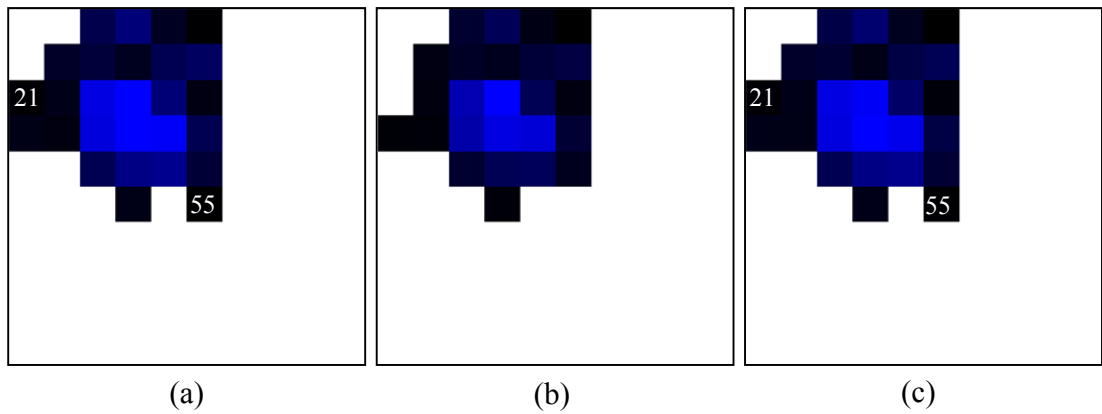


Fig. 6.15. CH chemical maps after setting threshold value for peak area: (a) Raman data normalized to the same intensity range; (b) Raman spectra normalized to the same integrated signal; (c) standardized Raman spectra

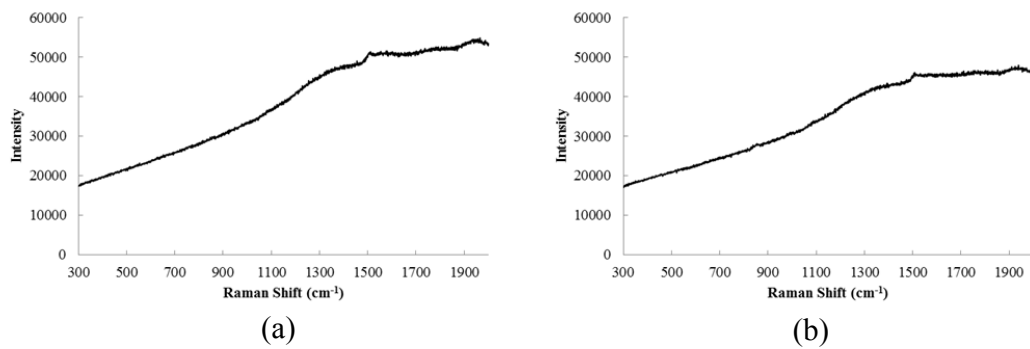


Fig. 6.16. Acquired Raman spectra from point (a) #21 and (b) #55

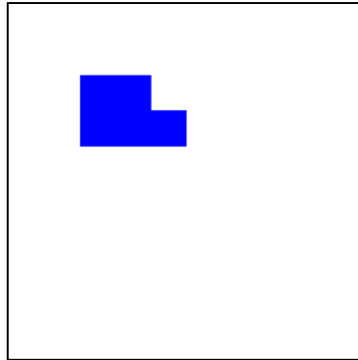


Fig. 6.17. Chemical map concentrated with CH

The threshold setting method was also used when mapping the C-S-H gel and calcium silicates with the three different normalization methods. It is found that these three methods produced the same chemical maps for both components, which are illustrated in Fig. 6.18. It should be pointed out that ettringite was not detected in the measured area (due to the limited size of the mapped area), so its map was not shown. From the figure, C-S-H gel was found at point #52 and #53, and calcium silicates were at point #55 and #58. These were consistent with the Raman detections. Therefore it can be concluded that mapping with peak area with any of the three normalization method is able to provide the chemical maps reflecting the distribution of the components. Thus when studying the cement pastes at different hydration ages (Chapter 7), the peak area mapping with standardized data was used. The gained results were also compared with the other two normalization methods. They did not show significant differences regarding the maps with concentrated components.

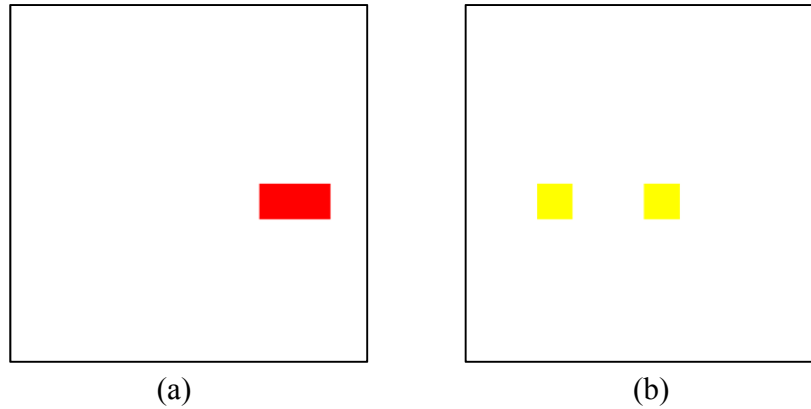


Fig. 6.18. Chemical maps for (a) C-S-H gel and (b) calcium silicates

6.3.3 Mapping with Components Method

Components method is to fit the obtained Raman spectrum to a linear combination of all the components spectra in the sample. Different from the two mapping methods discussed previously, this method requires the availability of the reference spectra for the studied components. Good mapping results can be obtained when the reference spectra for all the components in the mixture are available. However, the maps gained with the spectra for the main components may also be useful. Therefore, this method was also used for mapping the SCC pastes as a preliminary study.

From the hydration study (Chapter 4 and 5), the peaks for C-S-H gel, ettringite, and CH can be found, which are shown in Fig. 6.19. The characteristic peaks for C_3S and C_2S were quite close in the hydrated cement paste (e.g., Fig. 5.3 in Chapter 5), so they were treated as one component during mapping. Its reference spectrum is also displayed in Fig. 6.19. In this figure, the patterns were normalized to have the same intensity range. It has been mentioned in *Section 6.3.1 part (a)* that the peak at 625 cm^{-1} for C-S-H gel

cannot be detected in the measured area. So the reference pattern for C-S-H gel was only characterized with the peak at 450cm^{-1} .

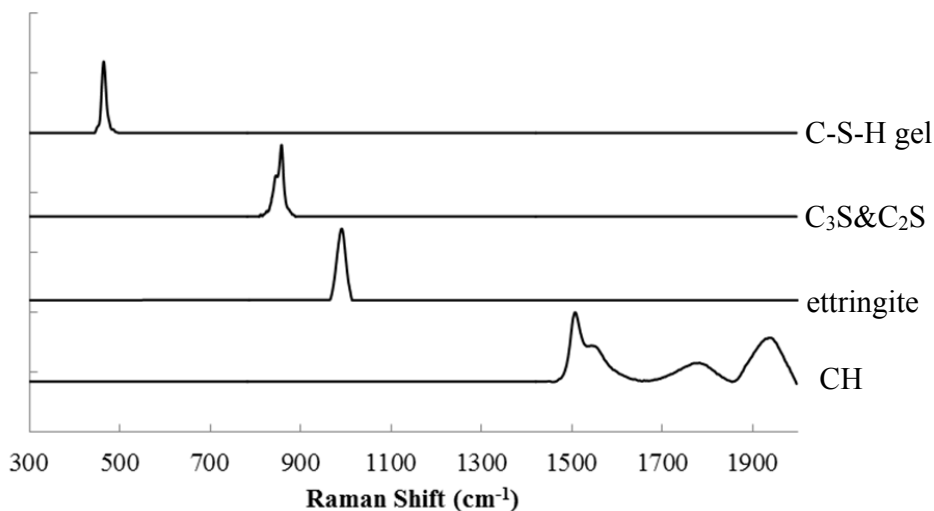


Fig. 6.19. Reference spectrums used in mapping with the components method

Similarly to the chemical maps with peak intensity, the background of the acquired spectrums should be removed before applying the components method. Fig. 6.20 shows the gained chemical map for C-S-H gel. This map is gained from the same area as that in Fig. 18(a). C-S-H gel was only detected in two points in this area, i.e., point #52 and #53. But from this map, several points without C-S-H gel peak are brighter than point #52, such as point #4 and #36. Therefore, components method on the background subtracted data is not able to provide the chemical maps consistent with the detections from the Raman patterns. The aforementioned normalization methods were also used for the components method to figure out whether the maps can be improved or not.

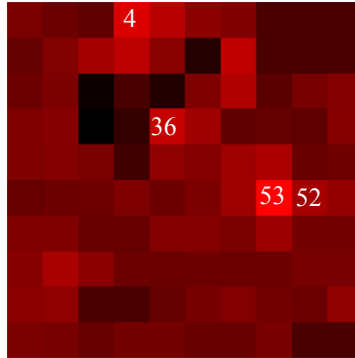


Fig. 6.20. Chemical map for C-S-H gel gained by components method on the background subtracted Raman data

With the application of the normalization methods, the map for C-S-H gel was produced correctly. When checking the maps for calcium silicates with the same methods, the problem that the brightness did not correspond to the component concentration still existed. The chemical maps for calcium silicates are displayed in Fig. 6.21. It can be seen that in all the images, the brightness of points #70 and #72 is higher than point #55. There was actually no calcium silicates detected from the former two points, while the point #55 had a relatively strong peak. Thus it is validate to conclude that the components method is not appropriate to be applied in mapping the cement pastes.

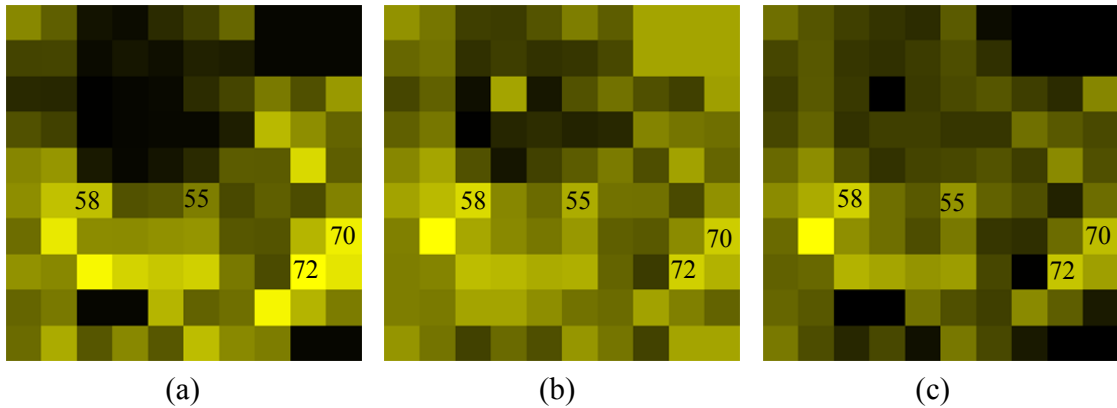


Fig. 6.21. Chemical maps for C_3S and C_2S with the components method: (a) Raman data normalized to the same intensity range; (b) Raman spectra normalized to the same integrated signal; (c) standardized Raman spectra

6.4 Composite Maps

The chemical maps shown above were for single component. It is necessary to merge the maps together to investigate the connections of the different components in the paste. Fig. 6.22 displays the composite map from merging the chemical images shown in Figs. 6.17 and 6.18. Same procedures were also applied to another specimen. The map is shown as Fig. 6.22(b). The colors red, yellow, green, and blue are still representing C-S-H gel, calcium silicates, ettringite, and CH in the maps. By comparing the two images, they vary significantly in the types and amounts of the components detected. This can be caused by the limited area measured ($20 \times 20 \mu\text{m}^2$). From Fig. 6.22(a), one can see the isolated areas with blue, yellow, and red colors. That means for this specimen, there is no overlapped area of each component. In Fig. 6.22(b), it is seen that ettringite tends to concentrate on the surface of cement particles, which is shown as the overlapped zone of

yellow (calcium silicates) and green colors (ettringite). Therefore, the maps can help us not only identify the location and dispersion of each ingredient, but also find out the correlations and connections between different phases.

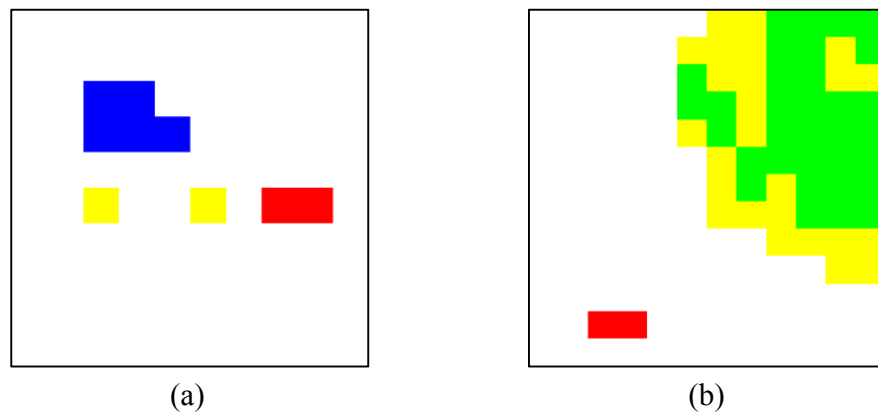


Fig. 6.22. Composite maps gained from two measured areas

6.5 Summary

In this chapter, the chemical mapping protocol for cement paste was developed. After the spectra of the observed area were obtained, three chemical mapping methods, including mapping with peak intensity, mapping with peak area, and mapping with components method, were used to investigate two SCC specimens as a preliminary study. The targeted good map would give the correct locations of an ingredient, and in the meantime, the brightness of map would reflect the concentration of that ingredient correctly. By comparing the results gained, the images based on mapping with peak area method were consistent with the detections of the Raman signals over the measured area for the SCC samples. The composite maps merged from the images for each individual component was not only able to provide the information on the physical dispersion of the

components, but also the contacts and connections between the different phases. Based on this preliminary study, the developed protocol was applied extensively to Portland cement pastes with different w/c ratios and different hydration ages. The research findings are illustrated in the following chapter.

CHAPTER 7

RAMAN CHEMICAL MAPPING STUDY ON PORTLAND CEMENT PASTE

7.1 Introduction

Based on the preliminary study introduced in the previous chapter, chemical mapping with peak area was able to reflect the distributions and connections of the different components in the SCC paste, including C-S-H gel, calcium silicates, ettringite, and CH. Thus, in this chapter, the established mapping protocol is applied to extensively and systematically investigate the microstructure evolution of hardened Portland cement pastes. Combining the gained chemical maps with the spectral analysis of the fresh paste, the effect of early-age hydration on the microstructure development of the cement pastes at late age can be explored.

Cement pastes with w/c ratios of 0.35 to 0.60 were used, which were the same as in the fresh paste study (Chapter 4). The main components, calcium silicates, ettringite, and CH, were mapped at the different hydration ages from 12 hours after mixing to 28 days. From their chemical maps, the microstructure of cement paste at different hydration ages was observed. It was found that ettringite tended to locate on the surface of silicates at the early age. And CH was apt to concentrate and localize in the pores. CH was the only phase that can be detected as a pure phase in the single measuring cells.

7.2 Experimental Procedures

7.2.1 Materials and Sample Preparation

Type I Portland Cement was used and its chemical ingredients were introduced in Chapter 4 (Tables 4.1 and 4.2). Cement pastes with w/c ratios of 0.35, 0.40, 0.50, and 0.60 were properly mixed (ASTM C305, 2014) and transferred to sample holders with a size of around 20×20×10 mm. Then the sample holders were slightly tapped to remove the entrapped air. A plastic sheet was then used to cover the sample holders to prevent moisture loss. When hardened, the samples were demolded and cured under lime saturated water with a constant temperature of 22±2°C till the designated hydration ages of 12 hours, 1 day, 2 days, 3 days, 7 days, 14 days, 21 days and 28 days. At each age, 3 samples were prepared for Raman chemical mapping. Because the chemical mapping process can take a couple of hours, and it is well known that at early ages, pastes without hydration arresting can undergo significant microstructure changes, additional sample preparation processes were adopted to avoid microstructural changes during mapping measurements. Firstly, the hydration of the samples was stopped by immersing the specimens into isopropanol for 7 days. The microstructure of the cement paste can be reserved to a maximum extent by using this type of alcohol (Feldman and Beaudoin, 1991; Konecny and Naqvi, 1993; Collier et al., 2008). During the 7 days, isopropanol was replaced regularly, every 12 hours for the first 3 days, and then once a day. After that, the samples were put into an oven at the temperature of 60 °C for 24 hours to evaporate the remaining solution. Thereafter, the dried samples were stored in a desiccator till the onset of the Raman testing. Right before carrying out mapping measurements, paste samples were ground lightly to give relatively smooth and flat surfaces. Grounding the

7.2.3 Mapping Creation

Mapping with the peak area was applied to construct the chemical images for calcium silicates (C_3S+C_2S), ettringite, and CH in the cement pastes during hydration. Their maps were created by mapping the area under shift range of 823-880, 962-986, and 1467-1670 cm^{-1} respectively. One can note that the chemical map for C-S-H gel was not studied in the current research. This is because C-S-H gel became nearly undetectable. Only one or two points were found in the whole measured areas. It has already been discussed in *Section 6.3.1* that the undetectable C-S-H gel should be attributed to the morphology and structure changes with the hydration progress, which was also found by other researcher (Bensted, 1976).

Mapping with peak area does not require the Raman spectra to be background subtracted. The acquired patterns just need to be normalized to have the same intensity range or same integrated signal, or same mean and variance. As discussed in *Section 6.3.2*, all these three normalization methods were applicable to be used. In this study, the last one was selected. The mean and variance were set as 0 and 1 respectively. There is no requirement on the value of these two parameters, only if the obtained chemical maps fit well with the Raman signals. For each chemical map, brightness threshold was set to remove the points that did not contain the specific component. The detailed procedures in setting the threshold have been illustrated in *Section 6.3.2*. After defining the threshold, the uncertainty in determining the presence of the component in the points with relatively weak peaks was further eliminated by only studying the points with concentrated component.

7.3 Chemical Mapping Analysis for Cement Paste

7.3.1 Chemical Maps for Calcium Silicates

Fig. 7.2 shows the gained calcium silicates maps for the cement paste with a w/c ratio of 0.35 at the hydration age of 12 hours to 28 days. In current study, area fraction, the fraction of the points with the concentrated compound over the total measured area (625 points), was taken as an indication of the compound content in the paste. As seen from this figure, the content of calcium silicates decreases significantly with the increase of the hydration age. The area fraction for calcium silicates was 30.23% at 12 hours. After the paste hydrated for 28 days, it decreased to 13.20%. The maps also indicated that from 12 hours to 28 days, there were less and less small cement particles. This can be observed by comparing the number of small spots (4 μm) at each specific age. This complies with the widely accepted concept that smaller particles have higher hydration rates than bigger particles, so they would be consumed more quickly during the hydration process (Costoya, 2008; Scrivener and Nonat, 2011). It is also noticed that the unreacted cement grains become more dispersive at the increased ages, which may be caused by the reduced size of the particles with the hydration progress. These phenomena also occurred to the cement pastes with the other w/c ratios during the hydration process.

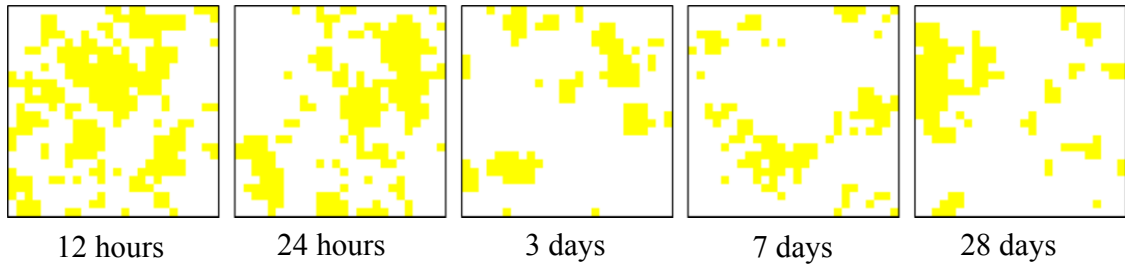


Fig. 7.2. Chemical maps for calcium silicates in the paste with a w/c ratio of 0.35 at the hydration ages from 12 hours to 28 days

Comparison of the calcium silicates maps in the cement pastes with different w/c ratios was also conducted to reveal the influence of solid concentration on the paste microstructure. Fig. 7.3 illustrates the maps for calcium silicates in the pastes with four w/c ratios at the hydration ages of 12 hours and 28 days. At both ages, cement paste with lower w/c ratio contained more unreacted calcium silicates. For example, at 12 hours, the content of calcium silicates was decreasing from 30.23% in the cement paste with a w/c ratio of 0.35 to 16.62% in the paste with a w/c ratio of 0.60. It is also seen from the figure that at each age, the amount of big unreacted cement particles ($>12\ \mu\text{m}$) was higher in the cement paste with lower w/c ratio. Taking the cement pastes at the hydration age of 28 days as an example, in the cement paste with a w/c ratio of 0.35, most of the unreacted cement particles had a size of 12 to 16 μm with one particularly large particle having the size of up to $30 \times 50\ \mu\text{m}$. At this age, only one big particle (around 16 μm) was found in the paste with a w/c ratio of 0.60, together with several smaller particles (4-8 μm). Less big particles remained in the cement paste with higher w/c ratio can be caused by the less amount of cement used and also the higher hydration rate of the paste. Less cement used would reduce the chance of incorporating bigger particles into paste, while the cement

particles in the cement paste with higher w/c ratio hydrate faster and thus the unreacted grains would be smaller at the same hydration age.

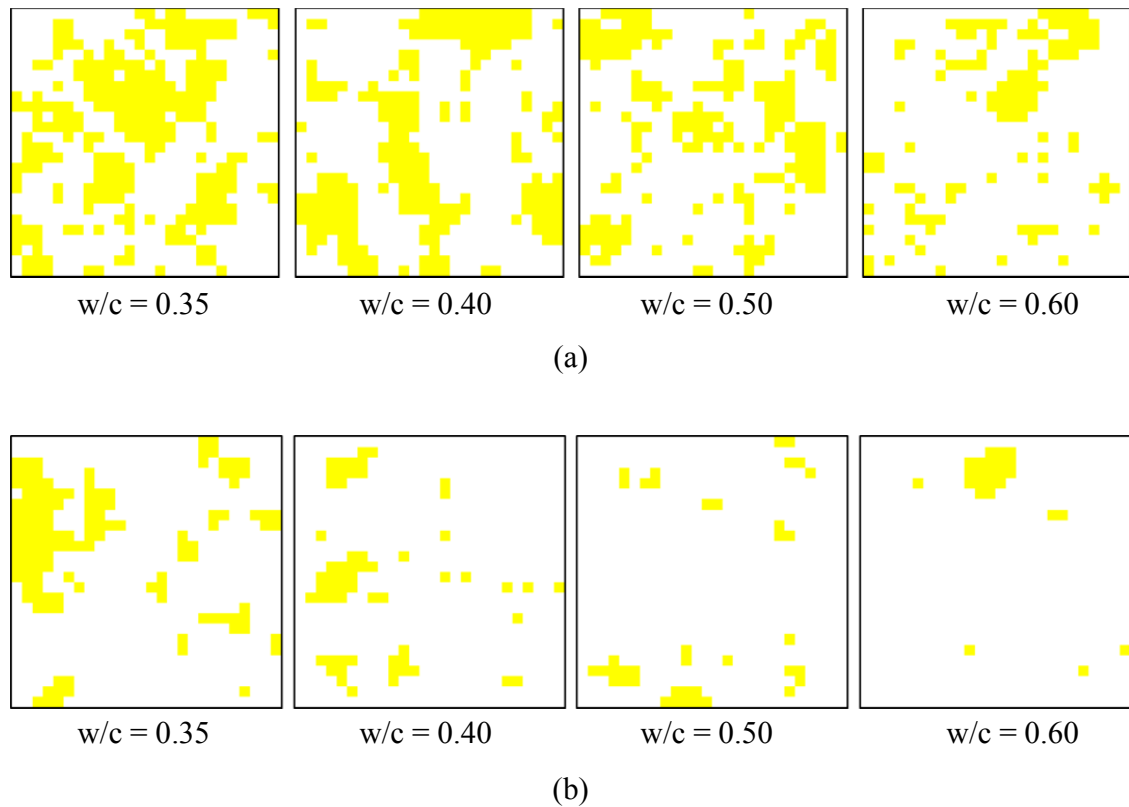


Fig. 7.3. Calcium silicates maps for cement pastes with four different w/c ratios at the hydration ages of (a) 12 hours and (b) 28 days

7.3.2 Chemical Maps for Calcium Hydroxide

As one of the major hydration products, the distribution of calcium hydroxide (CH) in the cement paste was also examined. Fig. 7.4 displays the obtained chemical maps for CH in the cement paste with a w/c ratio of 0.35 at the ages of 12 hours to 28 days. It is seen from this figure that with the increased hydration age, the area fraction of calcium hydroxide increases. Its content increased from 10.30% at 12 hours to 25.11% at

28 days. The increased CH corresponds to the decreased amount of calcium silicates observed in Fig. 7.2. With the hydration progress, the growth and connection of CH can be found. From the chemical image at 12 hours, the sizes of CH clusters were in the range of 4 to 20 μm , and these CH clusters were isolated with each other. After cement paste hydrated for longer period, CH clusters were bigger and became contact with one another, forming clusters with a size of even larger than 50 μm . This can be observed clearly in CH chemical maps hydrated for more than 3 days. The similar developments of CH were also found in the cement pastes with other three w/c ratios during the hydration process.

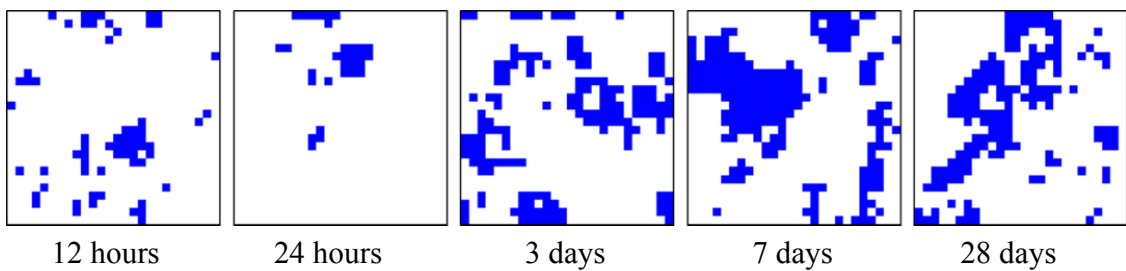


Fig. 7.4. Chemical maps for CH in the paste with a w/c ratio of 0.35 at the hydration ages from 12 hours to 28 days

The comparison regarding the CH distribution in the cement pastes with different w/c ratios at the same hydration age was also implemented. The chemical maps for CH in the pastes with the hydration ages of 12 hours and 28 days are shown in Fig. 7.5. By comparing the images at each age, less CH content is contained in the cement paste with higher w/c ratio. At 12 hours, the CH content was decreased from 10.30% in the cement paste with a w/c ratio of 0.35 to 5.31% in the paste with a w/c ratio of 0.60. For cement pastes hydrated for 28 days (Fig. 5(b)), CH fraction was decreased from 25.10% to 17.59% with the increased w/c ratios from 0.35 to 0.60. When looking at Fig. 5(b), one may note

that the paste with a w/c ratio of 0.50 had the highest CH content (35.95%) at 28 days. This may be caused by the coincident measurement on the area dominated by CH.

From the maps in Fig. 7.5, there is no significant difference found for the distribution of CH clusters in the different pastes. At 12 hours, most of the CH clusters had the size of 4-12 μm with one or two clusters of 20 μm big in the measured area. This was observed in the pastes with all four w/c ratios. When cement hydrated for 28 days, the maps were mainly occupied by large clusters (20 to 30 μm). Small CH cluster (4-8 μm) was also found in the pastes, but the area fraction was much lower than the large clusters.

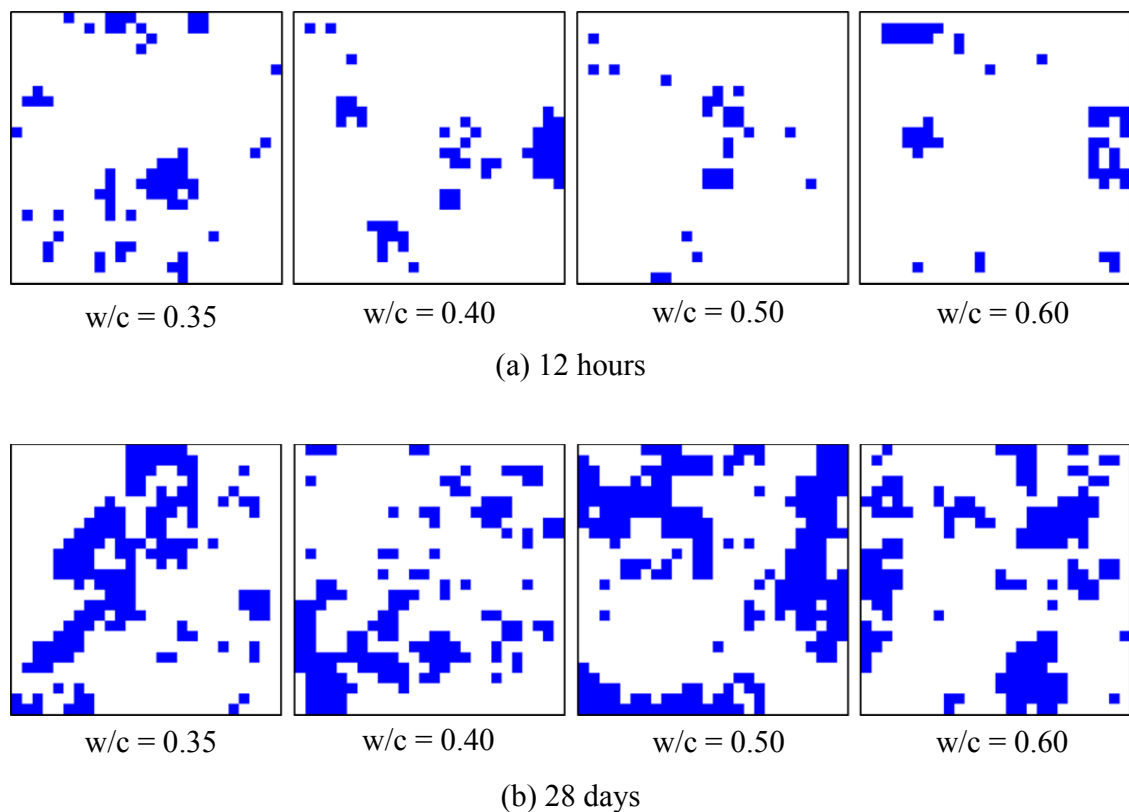


Fig. 7.5. CH maps for cement pastes with four different w/c ratios at the hydration ages of (a) 12 hours and (b) 28 days

7.3.3 Chemical Maps for Ettringite

The last component studied was ettringite. Fig 7.6 shows the ettringite in the cement paste with a w/c ratio of 0.35 at the different hydration ages. From this figure, ettringite content was found to decrease with the increased hydration ages. Its fraction decreased from 8.83% at 12 hours to 1.23 % at 28 days. Compared to calcium silicates (30.23 to 13.20%) and CH (10.30 to 25.11%) in the cement paste with the same w/c ratio (Fig. 7.4), the fraction of ettringite was always less than these two components at the different hydration ages.

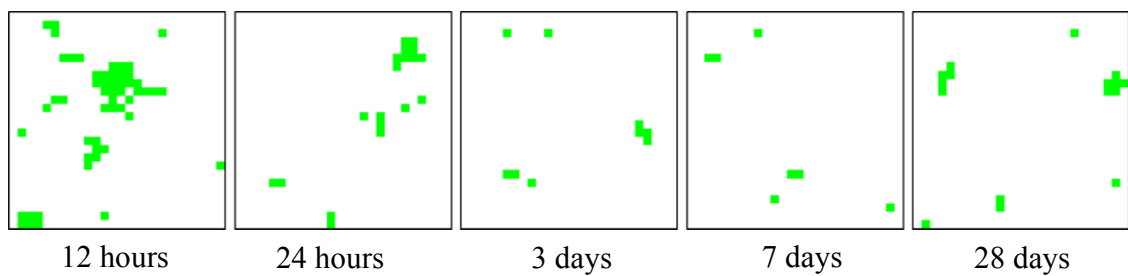


Fig. 7.6. Chemical maps for ettringite in the paste with a w/c ratio of 0.35 at the hydration ages from 12 hours to 28 days

With the examination of ettringite maps in the cement pastes with all four w/c ratios, the sizes of the ettringite clusters were found to be similar in all the pastes, in the range of 4 to 20 μm . The dispersive distributions of these clusters across the measured area were also found. But it should be pointed out that the content of ettringite changed in different ways in the cement pastes with different w/c ratios. Fig. 7.7 depicts the ettringite fractions at the different hydration ages in the cement pastes. From the figure, decreased content of ettringite from 12 hours is only observed in the cement paste with a w/c ratio of 0.35. In the cement pastes with higher w/c ratios, 0.40, 0.50, and 0.60, the content

increased slightly from 12 hours to 48 hours and then it remained almost constant till 28 days. One may notice that in these pastes, ettringite content scattered after 48 hours. But it is still seen not to change significantly from 48 hours to 28 days.

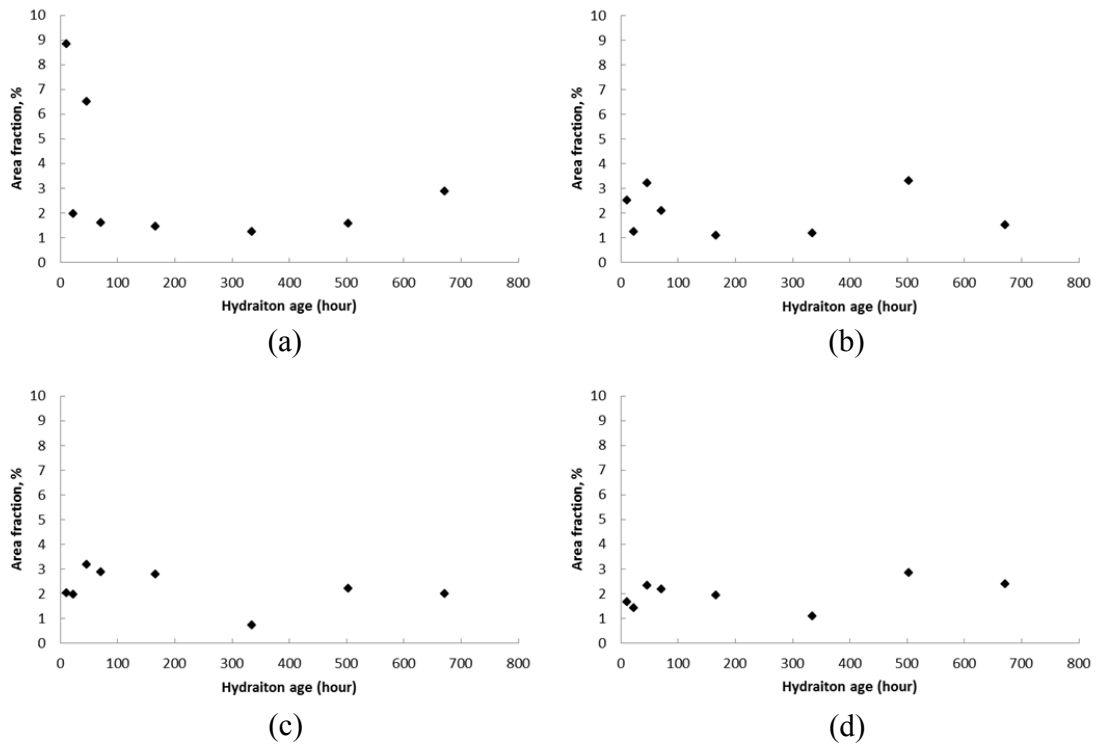


Fig. 7.7. Area fraction changes of ettringite in the cement pastes with w/c ratios of: (a) 0.35; (b) 0.40; (c) 0.50; and (d) 0.60

7.3.4 Composite Maps for Cement Pastes

The maps for calcium silicates, CH, and ettringite were merged together to create the composite map that simultaneously contained all the three components. These maps were utilized to investigate the dispersions and connections of the different components in the paste microstructure. Figs. 7.8-7.11 show the composite maps for cement pastes with w/c ratios of 0.35 to 0.60 during the hydration process. The colors yellow, green,

and blue in the maps are still representing calcium silicates, ettringite, and CH, respectively. From the figures, there is no significant difference found in the connections of the different components in the cement pastes with various w/c ratios. As shown in the composite maps, ettringite was mainly detected on the surface of the unreacted calcium silicates, which was shown as an overlapped zone of colors yellow and green on all the maps (Figs. 7.8-7.11). On the contrary, there are very few overlapped areas between CH and calcium silicates. CH was first emerged at the peripheral area of silicates, and it gradually precipitated to the locations away from the unreacted cement particles as big crystals (sometimes bigger than 50 μm). Thus it is postulated that CH was more likely to form in the pores rather than on the surface of cement grains. It should be mentioned that CH was the only phase that was detected as a pure phase in some locations. While for silicates and ettringite, their detections were always accompanied with other phases. Due to their different precipitation locations, the contact between CH and ettringite was only found in few points over the whole measured area. The schematic diagrams illustrating the paste microstructural development is shown in Fig. 7.12.

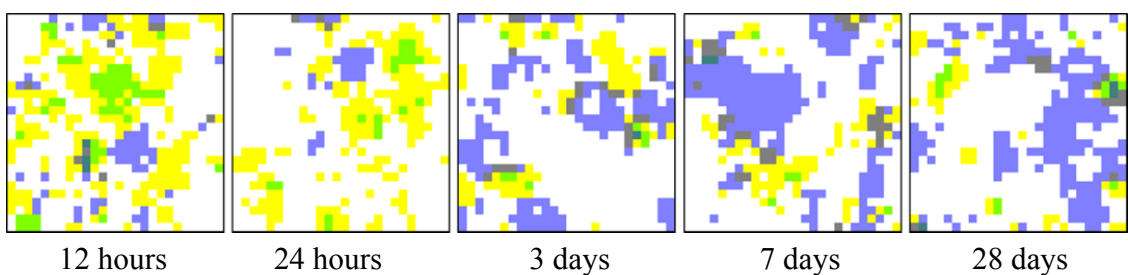


Fig. 7.8. Composite maps for the paste with a w/c ratio of 0.35 during hydration

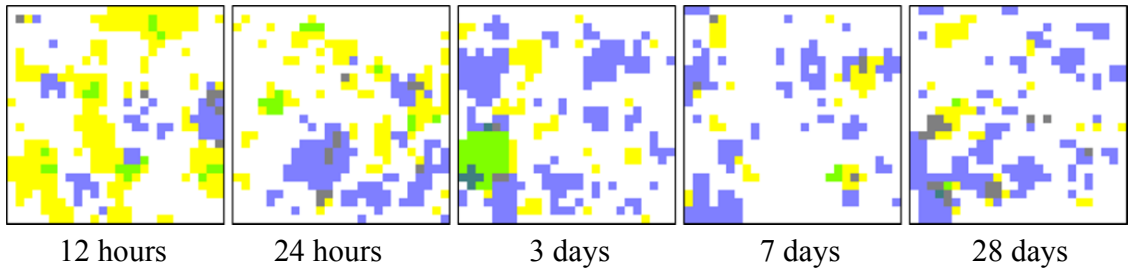


Fig. 7.9. Composite maps for the paste with a w/c ratio of 0.40 during hydration

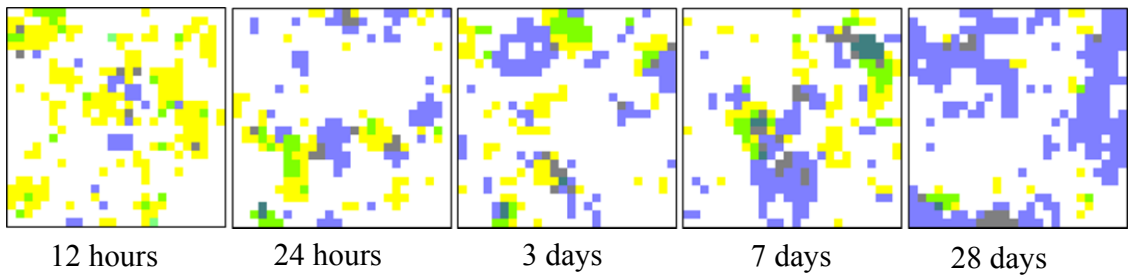


Fig. 7.10. Composite maps for the paste with a w/c ratio of 0.50 during hydration

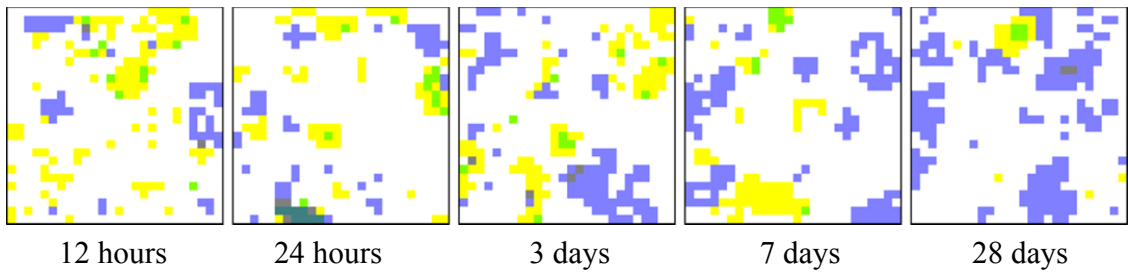


Fig. 7.11. Composite maps for the paste with a w/c ratio of 0.60 during hydration

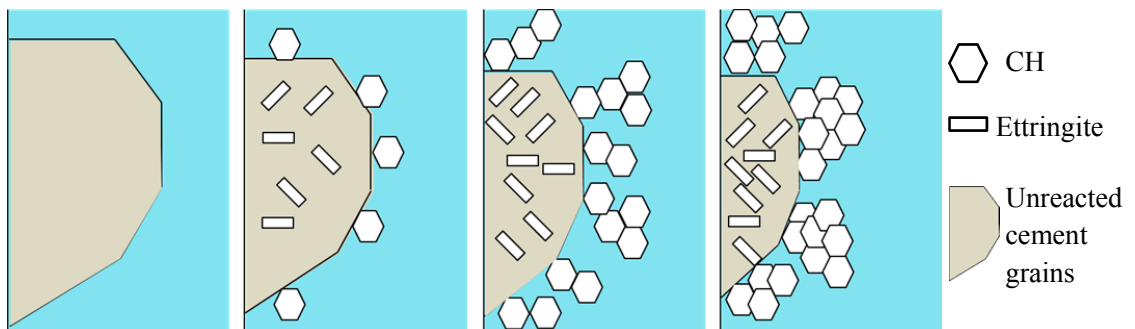


Fig. 7.12. Schematic diagrams for the distributions and connections of the unreacted cement grains, CH, and ettringite in the paste during the hydration process

7.4 Quantitative Analysis on Cement Hydration

From 12 hours to 28 days, cement hydration is dominated by the reaction of calcium silicates (*Stage IV in Section 2.2.3*). Therefore, in order to study the influence of w/c ratio on hydration and microstructure, quantitative analysis was applied to track the fraction changes of calcium silicates and CH. The detailed analyses are presented as follows.

7.4.1 Quantitative analysis on Fraction Change of Calcium Silicates

Fig. 7.13 illustrates the fractions of calcium silicates in the cement pastes with all four w/c ratios at the different hydration ages. It can be seen from the figure that for each w/c ratio, calcium silicates decreased consistently from 12 hours to 28 days, which was similar to the direct observation from the chemical maps. Comparing to the maps, the figure provides more information on decreasing rate of calcium silicates. It can be seen that the decreasing rates are different at the early and late ages. For example, in the cement paste with a w/c ratio of 0.35 (Fig. 7.13(a)), calcium silicates decrease rapidly from 12 hours to 48 hours. Then its decreasing rate slows down and its content only decreases slightly. The similar decreasing trends are also found in the cement pastes with w/c ratios of 0.40, 0.50, and 0.60 (Fig. 7.13 (b)-(d)). The detailed differences about the decreasing rates in the cement pastes with different w/c ratios were compared by applying regression analysis, from which the results were shown as the curves in the figure.

The area fraction of calcium silicates, A , during the hydration process can be illustrated by Eq. (7.1).

$$A = \frac{A_0}{1+k \ln(1+t)} \quad (7.1)$$

In this equation, k is a shape factor that can be obtained via regression and t is the hydration age with the unit of hour. A_0 is representing the initial area fraction (volume fraction) of calcium silicates before cement hydration and can be calculated by the following equation:

$$A_0 = \frac{\frac{1}{SG} \times W}{\frac{1}{SG} + w/c} \quad (7.2)$$

where W is the mass percentage of calcium silicates (C_3S+C_2S) in the cement used and it can be calculated from Table 4.2, i.e., 74.61% (64.62% for C_3S and 9.99% for C_2S). In this equation, SG is the specific gravity of the cement used, which typically has the value of 3.15 (PCA, 1988). With the known value of W and SG, A_0 can be easily calculated for cement pastes with w/c ratios of 0.35, 0.40, 0.50, and 0.60, which were 37.55%, 32.66%, 29.33%, and 26.12%, respectively. It should be mentioned that by using the equation, the specific gravities of the different cement ingredients were assumed to be the same.

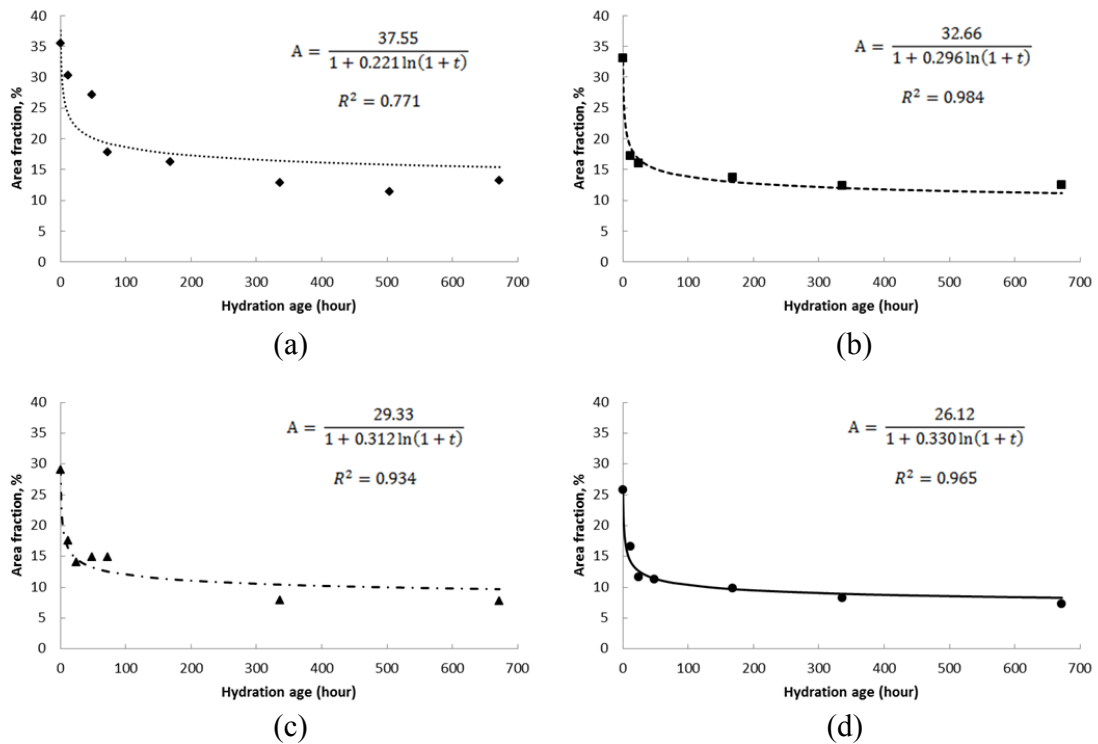


Fig. 7.13. Area fraction changes of calcium silicates in the cement pastes with w/c ratios of: (a) 0.35; (b) 0.40; (c) 0.50; and (d) 0.60

The regression equations are also shown in the upper right corner in each of the fraction charts in Fig. 7.13, together with the coefficients of determination (R^2). In the equation, the value of k governs the converging rate of each curve. From the regression, it can be seen that the k value increases with the increase of w/c ratio. That means for the paste with a w/c ratio of 0.60, the A value converges to its final value more quickly than any other w/c ratios. This converging rate corresponds to the quick consumption of calcium silicates in this paste.

Fig. 7.14 stacked the four curves shown in Fig. 7.13 together. For a given age, the cement paste with lower w/c ratio always has higher calcium silicates content. With the

curves, it can be expected that at the ages later than 28 days, there will still be more unreacted cement grains in the cement paste with lower w/c ratio.

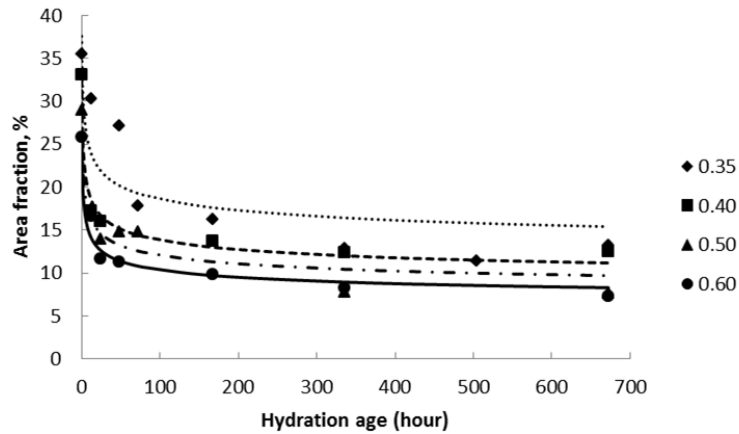


Fig. 7.14. Curves for the fraction changes of calcium silicates in the pastes with four different w/c ratios

7.4.2 Quantitative Analysis on Fraction Change of CH

With the decreasing content of calcium silicates, CH content was increasing. The detailed fractions of CH in the different cement pastes with hydration progress are shown in Fig. 7.15. For cement paste with each w/c ratio, the increasing rate of CH was found to be different at the different ages. The rapid increase of CH fraction in the first 48 hours was observed, which was corresponding to the faster consumption of calcium silicates during this period (Fig. 7.13). After 48 hours, the increasing rate of CH slowed down and its content only increased slightly till 28 days. Similarly to the fraction changes of calcium silicates, regression analysis was also applied to all the pastes to figure out the differences in the formation rate of CH when pastes had different w/c ratios.

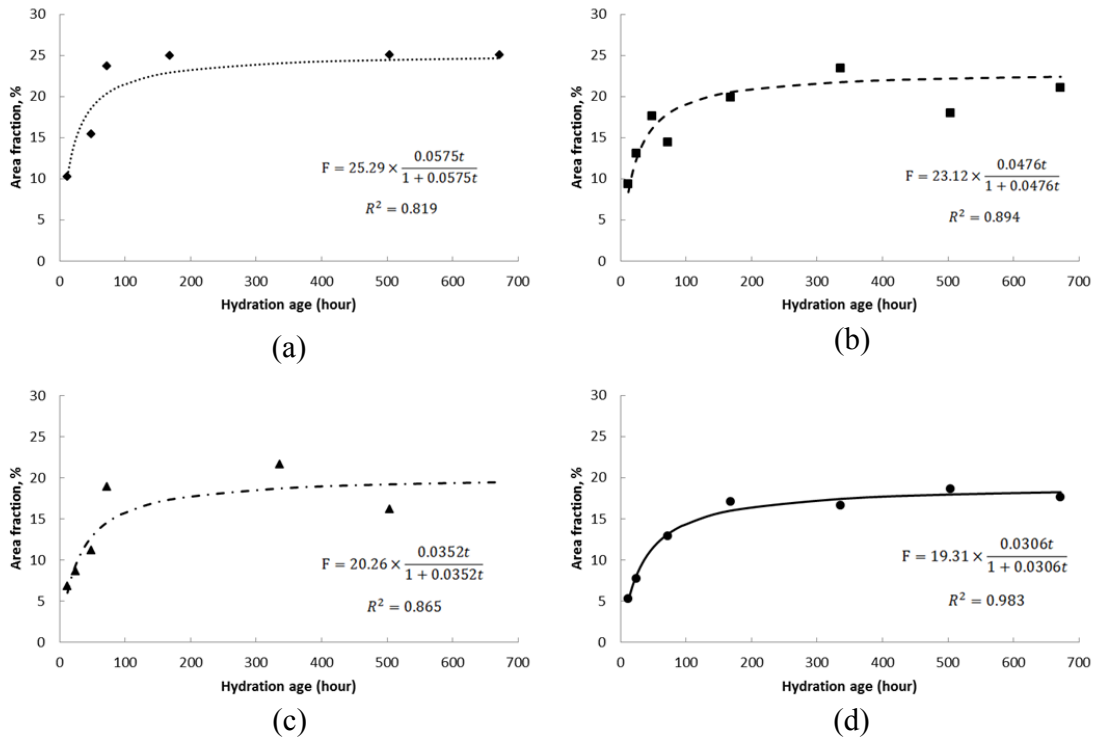


Fig. 7.15. Area fraction changes of CH in the cement pastes with w/c ratios of: (a) 0.35; (b) 0.40; (c) 0.50; and (d) 0.60

CH fraction, F , at different hydration ages in the cement paste can be described by Eq. (7.3).

$$F = F_u \times \frac{\alpha t}{1 + \alpha t} \quad (7.3)$$

where F_u and α are the two parameters that can be obtained via regression. The physical meaning of F_u is the ultimate area fraction achieved when cement hydrates completely. Same as in Eq. (7.1), t represents the hydration age (hour).

The regressed equations from the least square fit of the CH fractions are shown in Fig. 7.15 in the lower right corner in the charts, together with the coefficients of determination (R^2). The curves based on the obtained equations were also plotted for the

cement pastes with four w/c ratios. From the figure, R^2 has the values of 0.819 to 0.983, all of which are acceptable. This indicates the validity of using Eq. (7.3) to fit the fraction changes of CH. It is also seen from the figure that for cement pastes with w/c ratios of 0.35, 0.40, 0.50 and 0.60, the value of the ultimate CH fraction (F_u) is 25.29%, 23.12%, 20.26%, and 19.31%, respectively. This means that with the increased w/c ratio, less amount of CH will be formed when the cement is fully hydrated. This should be attributed to the less amount of cement used. In addition to the ultimate fraction (F_u), the coefficient α governs the shape of the curve. From the regression, the α value decreases persistently from 0.0575 in the cement paste with a w/c ratio of 0.35 to 0.0306 in the paste with a w/c ratio of 0.60. This indicates that in the paste with a w/c of 0.35, the CH value increases quickly during the early age to approach its ultimate value.

Fig. 7.16 stacks the fraction curves for CH in the cement pastes with four w/c ratios. It is observed that at each individual age, lower CH content is contained in the cement paste with higher w/c ratio.

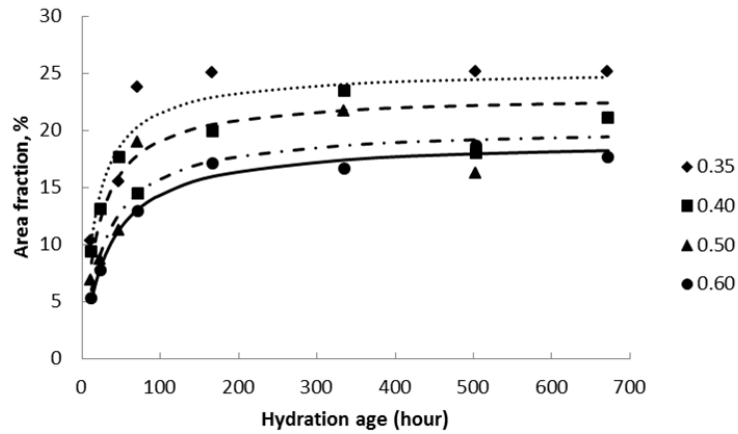


Fig. 7.16. Area fraction changes of CH for the cement pastes with four different w/c ratios

7.5 Conclusions

In this work, Raman spectroscopy was used to chemically map the microstructure development of cement pastes with w/c ratios of 0.35 to 0.60 from 12 hours to 28 days. Based on the chemical images and quantitative analysis on the fractions changes of the components, the following conclusions can be drawn:

(1) From the chemical maps for calcium silicates, the unreacted cement grains become more dispersive with the increased hydration ages from 12 hours to 28 days. With the hydration progress, the number of small particles with the size of around 4 μm decreased due to their faster hydration rates compared to the bigger particles. At all the ages, smaller amount of big unreacted grains ($> 12 \mu\text{m}$) was found in the cement paste with higher w/c ratio.

(2) Calcium silicates were found to hydrate much more rapidly in the first 48 hours. After 48 hours, their hydration slowed down. For cement paste with higher w/c ratio, the calcium silicates hydrated faster.

(3) At the early age of hydration, CH clusters were found to have the typical size of 4 to 20 μm and they were isolated from each other. With the ongoing hydration, CH became contact with one another and formed bigger clusters which sometimes could have a size larger than 50 μm .

(4) For a cement paste with higher w/c ratio at each age, the amount of CH was lower. But the size distribution of CH clusters did not vary significantly in the cement pastes with different w/c ratios.

(5) From the regression analysis, the increase of CH content corresponded well to the decrease of calcium silicates. The formation of CH was much faster during the first 48 hours, and then the content only increased slightly.

(6) The composite maps showed ettringite mainly formed on the surface of unreacted cement particles, while CH tended to precipitate as big particles in the pores.

CHAPTER 8

CONCLUSIONS AND FUTURE WORK

8.1 Conclusions

In this dissertation, the hydration process and microstructure development of fresh and hardened cement pastes were investigated by Raman spectroscopy. RS analysis was firstly applied to the in-situ and continuous observation on the hydration of fresh pastes during setting. The detected Raman signals were correlated to the macro-level properties of the pastes, including setting time and heat signature. The utilization of RS was then expanded to explore the differences in the hydration mechanisms in hardened ordinary pastes and UHPC. Besides these spectral analyses, the chemical mapping feature of RS was used to investigate the microstructure development of cement pastes with w/c ratios of 0.35 to 0.60 during the hydration from 12 hours to 28 days. From the mapping results, the effects of solid concentration on the paste microstructure development were evaluated. Based on these studies, the conclusions with regards to the main objectives of this research can be given as follows:

8.1.1 Fresh Cement Paste during Setting

(a) Hydration of C_3S and C_2S

C_3S and C_2S were characterized clearly by RS with the respective peaks at 833 and 887 cm^{-1} . After mixing, the intensities of these two peaks decreased dramatically due to the dissolution process. Their hydration produced CH and C-S-H gel. CH can be detected by RS at the very early stage of hydration with multiple peaks at the shifts from 1400 to 2000 cm^{-1} . These peaks consistently presented in the paste patterns from 20 minutes to 9 hours without significant intensity change. Another product, C-S-H gel, was detected later than CH in the pastes. It had characteristic peaks at 450 and 625 cm^{-1} . Its detection happened after dormant period but before initial setting time. For cement pastes with w/c ratios of 0.35, 0.40, 0.50, and 0.60, C-S-H gel was detected at the ages of 100, 140, 230, and 330 minutes, respectively. During the setting period, the intensity of C-S-H gel peaks did not change significantly.

(b) Reaction between C_3A and Gypsum

C_3A had a characteristic peak at 550 cm^{-1} and another peak at 750-760 cm^{-1} overlapped by C_4AF . C_3A reacted quickly with gypsum (with a peak of 1005 cm^{-1}) at the very early age of hydration, producing ettringite with the appearance of a peak at 991 cm^{-1} . The ettringite peak was presented consistently in the spectrums throughout the setting period. Its intensity remained almost constant during the first few hours and then it increased rapidly due to the renewed reaction of C_3A . The time point of the onset of ettringite increasing intensity can indicate the end of the dormant period in the pastes. Following the increasing period, ettringite intensity started to decrease till final set, which

was assumed to be caused by the ettringite conversion into monosulfate. In the current study, the peak for monosulfate (983 cm^{-1}) was found in the pastes with w/c ratios of 0.35 and 0.40 at the respective hydration ages of 140 and 360 minutes. This peak was not detected in the cement pastes with w/c ratios of 0.50 and 0.60.

8.1.2 Hydration Mechanisms of Ordinary Pastes and UHPC

(a) Class H Cement versus Type I Cement

Class H cement had C_3S , C_2S , and gypsum detected at the same shifts as Type I cement, at 833, 887 and 1005 cm^{-1} , respectively. But in Class H cement, C_3A peak cannot be separated from the overlapped region of C_3A and C_4AF due to the fact that it contained much less C_3A compared to Type I cement.

(b) Silica Sand, Silica Flour, and Silica Fume

Both silica sand and silica flour had a strong peak at 465 cm^{-1} , while the strongest peak for silica fume was at the shift of 517 cm^{-1} . Among all these three silicas, only silica flour had two relatively strong peaks at 1371 and 1397 cm^{-1} . These two peaks did not present in the patterns for silica sand and silica fume. Thus the two peaks at 1371 and 1397 cm^{-1} were taken as the characteristic peaks for silica flour in the study. Different from the silica sand and silica flour that did not take part in the hydration, the pozzolanic reaction of silica fume was found. This reaction was more reactive during the first two weeks.

(c) C_3S and C_2S in Ordinary Pastes and UHPC

Calcium silicates decreased with increasing hydration ages in both materials, but this decreasing trend was more obvious in the ordinary cement paste than in the UHPC. Their hydration product, CH, was detected in both materials. In ordinary paste, CH amount increased with ages. However, in UHPC, its amount decreased after 7 days due to the consumption by silica fume reaction.

(d) Ettringite in Ordinary Pastes and UHPC

The peak for C_3A was undetectable in both materials at the observed ages from 3 to 28 days. The content of its hydration product, ettringite, had similar trend in the two materials. It decreased from 7 to 14 days and then kept almost constant till 28 days.

8.1.3 Chemical Mapping Analysis on Pastes Microstructure

(a) Mapping Protocol Developed

Three chemical mapping methods, including mapping with peak intensity, peak area, and components method were tried in the preliminary study. Among these three methods, only the mapping with peak area method provided the maps correctly reflecting the detections of the Raman spectrums acquired from the measured areas. For the application of this method, the obtained Raman spectrums from the mapped area should be normalized to have the same intensity, same integrated signal, or same mean and variance. The last normalization method was adopted in the current study. With the constructed maps, only the points with concentrated components were studied to remove

the uncertainty in determining the presence of the specific component in the points with relatively weak peaks.

(b) Maps for C_3S and C_2S

For a given cement paste, the chemical maps indicated the content of calcium silicates to decrease consistently from 12 hours to 28 days and they become more dispersively distributed at the increased hydration ages. The faster hydration of small particles with the size of around $4\mu\text{m}$ was also found. During the hydration process, these two components hydrated rapidly in the first 48 hours and thereafter the rates slowed down. With increased w/c ratio, their hydration rates increased.

(c) CH Images

CH formation was much faster during the first 48 hours and then its content only increased slightly. At the early age, CH clusters had a typical size of 4 to 20 μm and they were isolated from each other. With the ongoing hydration, the clusters became contact with each other and formed as big clusters (sometimes larger than 50 μm) in the pores.

(d) Images for ettringite

Compared to calcium silicates and CH, ettringite occupied much smaller area fraction in the chemical maps at all the hydration ages. This component was found to precipitate on the surface of unreacted cement grains.

8.2 Future Work

This work suggests Raman spectroscopy an efficient tool in studying the hydration process and microstructure development for the cement pastes. Some future work on this topic can be investigated:

- With the decreased intensity of ettringite peak after its increasing period during setting, the monosulfate was only detected in the fresh pastes with w/c ratios of 0.35 and 0.40, not in the pastes with w/c ratios of 0.50 and 0.60. The window for in-situ observation on the pastes with the latter two w/c ratios can be extended from 9 hours to 12 hours to further examine the peaks in the sulfate region.
- Chemical mapping of fresh cement pastes has not been implemented in the current study due to the long time (9 hours) needed for mapping measurements. In future research, instead of measuring a complete range of 300 to 2000 cm^{-1} , the shift range can be shortened to focus on studying the hydration behavior of each individual cement ingredient.
- The resolution for chemical maps in the current work was 4 μm , determined by the 50 \times magnification objective used. The objectives with higher magnifications can be used to improve the resolution. For example, by using the 100 \times magnification objective, the resolution for maps can be increased to 1 μm . The results would be helpful to understand the paste microstructure better.
- The 2-D chemical mapping method is promising for the distributions and connections of the cement pastes. The study can be extended to 3-D mapping to explore the depth profile of the hydrating paste.

- It will be interesting to compare the results of RS analysis with other existing micro-level techniques, such as XRD, IR, and SEM. Combining these methods will give more comprehensive understanding about cement hydration mechanism and microstructure development, benefiting the cement and concrete industries in their manufacturing and construction processes.
- With the available Raman spectrums and chemical images, computational tools can be explored to model the paste microstructure for the fresh pastes during the hydration process. The modeling results can be compared with macro-level properties, e.g., setting time and heat signature, which can provide supports to the RS findings.
- The research is currently staying with Type I cement and ordinary paste. It would be interesting to further investigate the application of Raman spectroscopy, including spectral analysis and chemical mapping, to other types of cement and paste/mortar/concrete with various chemical and mineral admixtures under the different curing conditions.

REFERENCES

- AFGC (Association Francaise de Genie Civil). (2002). "Ultra high performance fiber-reinforced concretes." Paris.
- ASTM. (2008). "Standard test method for time of setting of hydraulic cement by Vicat needle." C191, ASTM international, West Conshohocken, PA.
- ASTM. (2009) "Standard test method for measurement of heat of hydration of hydraulic cementitious materials using isothermal conduction calorimetry." C1702, ASTM international, West Conshohocken, PA.
- ASTM. (2014). "Standard practice for mechanical mixing of hydraulic cement pastes and mortars of plastic consistency." C305, ASTM international, West Conshohocken, PA.
- Bartels, R. H., Beatty, J. C., Barsky, B. A. (1987). *An introduction to splines for use in computer graphic and geometric modeling*, M. Kaufmann Publisher, Los Altos, CA.
- Belu, A., Mahoney, C., Wormuth, K. (2008). "Chemical imaging of drug eluting coatings: combining surface analysis and confocal Raman microscopy." *Journal of Controlled Release*, 2(3), 111-121.
- Bensted, J. (1976). "Use of Raman spectroscopy in cement chemistry." *Journal of the American Ceramic Society*, 59(3-4), 140-143.

- Bensted, J. (1977). "Raman spectral studies of carbonation phenomena." *Cement and Concrete Research*, 7(2), 161-164.
- Bensted, J. (1999). "Thaumasite – background and nature in deterioration of cements, mortars and concretes." *Cement and Concrete Research*, 21(2), 117-121.
- Black, L., Breen, C., Yarwood, J., Deng, C.-S., Phipps, J., Maitland, G. (2006). "Hydration of tricalcium aluminate (C₃A) in the presence and absence of gypsum – studied by Raman spectroscopy and X-ray diffraction." *Journal of Materials Chemistry*, 16(13), 1263-1272.
- Black, L., Breen, C., Yarwood, J., Garbev, K., Stemmermann, P., Gasharova, B. (2007). "Structural features of C-S-H (I) and its carbonation in air-a Raman spectroscopic study. Part II: carbonated phases." *Journal of American Ceramic Society*, 90(3), 908-917.
- Bonen, D., Johnson, T.J., Sarkar, S.L. (1994). "Characterization of principal clinker materials by FT-Raman microspectroscopy." *Cement and Concrete Research*, 24(5), 959-965.
- Brough, A.R., Atkinson, A. (2001). "Micro-Raman spectroscopy of thaumasite." *Cement and Concrete Research*, 31(3), 421-424.
- Bullard, J.W., Jennings, H.M., Livingstone, R.A., Nonat, A., Scherer, G.W., Schweitzer, J.S., Scrivener, K.L., Thomas, J.J. (2011). "Mechanisms of cement hydration." *Cement and Concrete Research*, 41(12), 1208-1223.
- Chen, Y., Odler, I. (1992). "On the origin of Portland cement setting". *Cement and Concrete Research*, 22(6), 1130-40.

Collier, N.C., Sharp, J.H., Milestone, N.B., Hill, J., Godfrey I.H. (2008). "The influence of water removal techniques on the composition and microstructure of hardened cement pastes." *Cement and Concrete Research*, 38(6), 737-44.

Conjeaud, M., Boyer, H. (1980). "Some Possibilities of Raman microprobe in cement chemistry." *Cement and Concrete Research*, 10(1), 61-70.

Costoya, M., (2008). "Kinetics and microstructural investigation on the hydration of tricalcium silicates." PhD Thesis, EPFL, Switzerland.

Cuberos, A.J.M., Torre, A.G.D.L., Martin-Sedeno, M.C., Moreno-Real, L., Merlini, M., Ordonez, M.L., Aranda, A.G. (2009). "Phase development in conventional and active belite cement pastes by Rietveld analysis and chemical constraints." *Cement and Concrete Research*, 39(10), 833-842.

Deng, C.S., Breen, C., Yarwood, J., Habesch, S., Phipps, J., Craster, B., Maitland, G. (2002). "Aging of oilfield cement at high humidity: a combined FEG-ESEM and Raman microscopic investigation." *Journal of Materials Chemistry*, 12, 3105-3112.

Deschner, F., Winnefeld, F., Lothenbach, B., Seufert, S., Schwesig, P., Dittrich, S., Goetz-Neunhoeffler, F., Neubauer, J. (2012). "Hydration of Portland cement with high replacement of siliceous fly ash." *Cement and Concrete Research*, 42(10), 1389-1400.

Diamond, S., Kjellsen, K.O. (2006). "Resolution of fine fibrous C-S-H in backscatter SEM examination." *Cement and Concrete Composites*, 28(2), 130-132.

- Diamond, S., Lachowski, E.E. (1983). "Investigation of the composition and morphology of individual particles of Portland cement paste: 2. Calcium sulfoaluminates." *Cement and Concrete Research*, 13 (3), 335-340.
- Feldman, R.F., Beaudoin, J.J. (1991). "Pretreatment of hardened hydrated cement pastes for mercury intrusion measurements." *Cement and Concrete Research*, 21(2-3), 297-308.
- FHWA (Federal Highway Administration) (2013). "Ultra-high performance concrete: A state-of-the-art report for the bridge community." FHWA-HRT-13-060, Frankfort, KY.
- Fischer, H., Ibach, W., Dampel, H., Sanchen, D. (2009). "A confocal Raman imaging study on emulsions." *Imaging & Microscopy*, 11(4), 35-38.
- Frías, M., Martínez-Ramírez, S. (2009). "Use of micro-Raman spectroscopy to study reaction kinetics in blended white cement pastes containing metakaolin." *Journal of Raman Spectroscopy*, 40(12), 2063-2068.
- Galluci, E., Mathur, P., Scrivener, K. (2010). "Microstructural development of early age hydration shells around cement grains." *Cement and Concrete Research*, 40(1), 4-13.
- Garbev, K., Stemmermann, P., Black, L., Breen, C., Yarwood, J., Gasharova, B. (2007). "Structural features of C-S-H (I) and its carbonation in air-a Raman spectroscopic study. Part I: fresh phases." *Journal of American Ceramic Society*, 90(3), 900-907.
- Garcia-mate, M., De la Torre, A.G., Leon-Reina, L., Aranda, M.A.G., Santacruz, I. (2013). "Hydration studies of calcium sulfoaluminate cements blended with fly ash." *Cement and Concrete Research*, 54, 12-20.

Gardiner, D. J. (1989). *Practical Raman Spectroscopy*, 1st ed., Springer, New York.

Garg, N. (2012). "Raman spectroscopy for characterizing and determining the pozzolanic reactivity of fly ashes." M.S. thesis, Iowa State Uni., Ames, IA.

Gastaldi, D., Boccaleri, E., Canonico, F., Bianchi, M. (2007). "The use of Raman spectroscopy as a versatile characterization tool for calciumsulphoaluminate cements: a compositional and hydration study." *Journal of Materials Science*, 42(20), 8426-8432.

Garg, N., Wang, K., Martin, S.W. (2013). "A Raman spectroscopic study of evolution of sulfates and hydroxides in cement-fly ash pastes." *Cement and Concrete Research*, 53, 91-103.

Gatta, G.D., McIntyre, G.J., Swanson, J.G., Jacobsen, S.D. (2012). "Minerals in cement chemistry: a single-crystal neutron diffraction and Raman spectroscopic study of thaumasite, $\text{Ca}_3\text{Si}(\text{OH})_6(\text{CO}_3)(\text{SO}_4)12\text{H}_2\text{O}$." *American Mineralogist*, 97(7), 1060-1069.

Ghosh, S.N., Handoo, S.K. (1980). "Infrared and Raman spectra studies in cement and concrete (review)." *Cement and Concrete Research*, 10(6), 771-782.

Gordon, K.C., McGoverin, C.M. (2011). "Raman mapping" of Pharmaceuticals." *International Journal of Pharmaceutical*, 417(1-2), 151-162.

Gu, P., Beaudoin, J.J. (1997). "A conduction calorimetric study of early hydration of ordinary Portland cement/high aluminate pastes." *Journal of Materials Science*, 32(14), 3875-3883.

Gualtieri, A.F., Boccaletti, M. (2011). "Recycling of the product of thermal inertization of cement-asbestos for the production of concrete." *Construction and Building Materials*, 25(8), 3561-3569.

Guedes, A., Valentim, B., Prieto, A.C., Sanz, A., Flores, D., Noronha, F. (2008). "Characterization of fly ash from a power plant and surroundings by micro-Raman spectroscopy." *International Journal of Coal Geology*, 73(3-4), 359-370.

Hadley, D.W., Dolch, W.L., Diamond, S. (2000). "On the occurrence of hollow-shell hydration grains in hydrated cement paste." *Cement and Concrete Research*, 30(1), 1-6.

Hann, D.H. (2007). "*Raman Scattering Theory*." University of Florida, Gainesville, FL.

Hesse, C., Goetz-Neunhoeffler, F., Neubauer, J., Braeu, M., Gaeberlein, P. (2007). "Quantitative in-situ X-ray diffraction analysis of early hydration of Portland cement at defined temperatures." *Powder Diffraction*, 24(2), 112-215.

Hill, J., Sharp, J.H. (2002). "The mineralogy and microstructure of three composite cements with high replacement levels." *Cement and Concrete Composites*, 24(2), 191-199.

Hughes, T.L., Methven, C.M., Jones, T.G., Pelham, S.E., Fletcher, P., Hall, C. (1995). "Determining cement compositions by Fourier transform infrared spectroscopy." *Advanced Cement Based Materials*, 2(3), 91-104.

Jansen, D., Goetz-Neunhoeffler, F., Lothenbach, B., Neubauer, J. (2012). "The early hydration of ordinary Portland cement: an approach comparing measured heat flow with calculated heat flow from QXRD." *Cement and Concrete Research*, 42(1), 134-138.

- Kalliopi, K.A., R de Rooij, M., Macdonald, D.D. (2000). "Analysis of iron oxides accumulating at the interface between aggregates and cement paste." *Cement and Concrete Research*, 30(12), 1941-1945.
- Katz, A., Bentur, A., Kovler, K. (2006). "A novel system for in-situ observations of early hydration reactions in wet conditions in conventional SEM." *Cement and Concrete Research*, 37(1), 32-37.
- Kim, K., Heo, Y., Kang, S., Lee, J. (2014). "Effect of sodium silicate- and ethyl silicate-based nano-silica on pore structure of cement composites." *Cement and Concrete Composites*, 49, 84-91.
- Kirkpatrick, R.J., Yarger, J.L., McMillan, P.F., Yu, P., Cong, X.D. (1997). "Raman spectroscopy of C-S-H, Tobermorite, and Jennite." *Advanced Cement Based Materials*, 5(3-4), 93-99.
- Kjellsen, K.O., Justnes, H. (2004). "Revisiting the microstructure of hydrating tricalcium silicate-a comparison to Portland cement." *Cement and Concrete Composites*, 26(8), 947-956.
- Kjellsen, K.O., Lagerblad, B. (1997). "Hollow-shell formation-an important mode in the hydration of Portland cement." *Journal of Materials Science*, 32(11), 2921-2927.
- Kjellsen, K.O., Lagerblad., B. (2007). "Microstructure of tricalcium silicate and Portland cement system at middle periods of hydration-development of Hadley grains." *Cement and Concrete Research*, 37(1), 13-20.

Korpa, A., Kowald, T., Trettin, R. (2009). "Phase development in normal and ultra-high performance cementitious systems by quantitative X-ray analysis and thermoanalytical methods." *Cement and Concrete Research*, 39(2), 69-76.

Konecny, L., Naqvi, S.J. (1993). "The effect of different drying techniques on the pore size distribution of blended cement mortars." *Cement and Concrete Research*, 23(5), 1223-1228.

Lothenbach, B., Winnefeld, F., Alder, C., Wieland, E., Lunk, P. (2007). "Effect of temperature on the pore solution, microstructure and hydration products of Portland cement pastes." *Cement and Concrete Research*, 37(4), 483-491.

Martinez-Ramirez, S., Sanchez-Cortes, S., Garcia-Ramos, J.V., Domingo, C., Fortes, C., Blanco-Vareta, M.T. (2003). "Micro-Raman spectroscopy applied to depth profiles of carbonates formed in lime mortar." *Cement and Concrete Research*, 33(12), 2063-2068.

Mechling, J., Lecomte, A., Diliberto, C. (2009). "Relation between cement composition and compressive strength of pure pastes." *Cement and Concrete Composites*, 31(4), 255-262.

Mehta, P.K., Monteiro, P.J.M. (2005). *Concrete microstructure, properties and materials*, 3rd ed., The McGraw-Hill Companies, New York.

Merlini, M., Artioli, G. (2007). "The early hydration and the set of Portland cements: In-situ X-ray powder diffraction studies." *Powder Diffraction*, 22(3), 201-208.

Mindness S., Young, J.F., Darwin D. (2003). *Concrete*, 1st ed., Pearson Education, Inc., Upper Saddle River, New Jersey.

Mollah, M.Y.A., Yu, W., Schennach, R., Cocke, D.L. (2000). "A Fourier transform infrared spectroscopic investigation of the early hydration of the early hydration of Portland cement and influence of sodium lignosulfonate." *Cement and Concrete Research*, 30(2), 267-273.

Myers, R.J., Bernal, S.A., Provis, J.L. (2014). "A thermodynamic model for C-(N)A-S-H gel: CNASH_{ss}. Deviation and validation." *Cement and Concrete Research*, 66, 27-47.

NRMCA (National Ready Mixed Concrete Association) (2013). "Ready Mixed Concrete Production Statistics."

Newman, S.P., Clifford, S.J., Coveney, P.V., Gupta, V., Blanchard, J.D., Serafin, F., Ben-Amotz, D., Diamond, S. (2005). "Anomalous fluorescence in near-infrared Raman spectroscopy of cementitious materials." *Cement and Concrete Research*, 35(8), 1620-1628.

Neville, A.M. (2010). *Properties of concrete*, 4th ed., Pearson Education limited, London.

Nonat, A., Mutin, J.C., Lecoq, X., Jiang, S.P. (1997). "Physico-chemical parameters determining hydration and particle interactions during the setting of silicate cements." *Solid State Ionics*, 101-103 part (2), 923-930.

Odler, I. (2003). "Hydration, setting and hardening of Portland cement." *Lea's chemistry of cement and concrete*, P. C. Hewlett, editor, 4th ed., Elsevier Ltd, London, 241-297.

Pang, X., Bentz, D.P., Meyer, C., Funkhouser, G.P., Darbe, R. (2013). "A comparison study of Portland cement hydration kinetics as measured by chemical shrinkage and isothermal calorimetry." *Cement and Concrete Composites*, 39, 23-32.

PCA (Portland Cement Association) (1998). "Design and control of concrete mixtures." Skokie, IL.

Peethamparan, S., Olek, J., Lovell, J. (2008). "Influence of chemical and physical characteristic of cement kiln dusts (CKDs) on their hydration behavior and potential suitability for soil stabilization." *Cement and Concrete Research*, 38(6), 803-815.

Princeton Instruments (2012). "Raman spectroscopy basics." <http://content.piacton.com/Uploads/Princeton/Documents/Library/UpdatedLibrary/Raman_Spectroscopy_Basics.pdf> (June, 2012)

Renaudin, G., Segni, R., Mentel, D., Nedelec, J., Leroux, F., Taviot-Gueho, C. (2007). "A Raman study of the sulfated cement hydrates: ettringite and monosulfate." *Journal of Advanced Concrete Technology*, 5(3), 299-312.

Richardson, I.G. (1999). "The nature of C-S-H in hardened cements." *Cement and Concrete Research*, 29(8), 1131-1147.

Richardson, I.G., Groves, G.W. (1993). "The incorporation of minor and trace elements into calcium silicate hydrate (C-S-H) gel in hardened cement pastes." *Cement and Concrete Research*, 23(1), 131-138.

Rietveld, H.M. (1969). "A profile refinement method for nuclear and magnetic structure." *Journal of Applied Crystallography*, 2(2), 65– 71.

Rodger, S.A., Groves, G.W. (1989). "Electron microscopy study of ordinary Portland cement and Ordinary Portland cement-pulverized fuel ash blended pastes." *Journal of the American Ceramic Society*, 72(6), 1037-1039.

- Sahu, S., Exline, D.L., Nelson, M.P. (2002). "Identification of thaumasite in concrete by Raman chemical imaging." *Cement and Concrete Composites*, 24(3-4), 347-350.
- Scrivener, K.L. (2004) "Backscattered electron imaging of cementitious microstructures: understanding and quantification." *Cement and Concrete Research*, 26(8), 935-45.
- Saoût, G.L., Kocaba, V., Scrivener K. (2011). "Application of the Rietveld method to the analysis of anhydrous cement." *Cement and Concrete Research*, 41(2), 133-148.
- Scrivener, K.L. (1989). "The microstructure of concrete." *Materials Science of Concrete*, J. Skalny, editor, American Ceramic Society, Westerville, 127-161.
- Scrivener, K.L. (2004). "Backscattered electron imaging of cementitious microstructures: understanding and quantification." *Cement and Concrete Composites*, 26(8), 935-945.
- Scrivener, K.L., Fullmann, T., Gallucci, E., Walenta, G., Bermejo, E. (2004). "Quantitative study of Portland cement hydration by X-ray diffraction/Rietveld analysis and independent methods." *Cement and Concrete Research*, 34(9), 1541-1547.
- Scrivener, K.L., Nonat, A. (2011). "Hydration of cementitious materials, present and future." *Cement and Concrete Research*, 41(7), 651-665.
- Simone, E., Saleemi, A.N., Nagy, Z.K., (2014). "Application of quantitative Raman spectroscopy for the monitoring of polymorphic transformation in crystallization processes using a good calibration practice procedure." *Chemical Engineering Research and Design*, 92(4), 594-611.

Skorda, D., Kontoyannis, C.G. (2008). "Identification and quantitative determination of atorvastatin calcium polymorph in tablets using FT-Raman spectroscopy." *Talanta*, 74(4), 1066-1070.

Snellings, R., Salze, A., Scrivener, K.L. (2014). "Use of X-ray diffraction to quantify amorphous supplementary cementitious materials in anhydrous and hydrated blended cements." *Cement and Concrete Research*, 64, 89-98.

Snelson, D.G., Wild, S., O'Farrell, M. (2008). "Heat of hydration of Portland cement – metakaolin – fly ash (PC-MK-PFA) blends." *Cement and Concrete Research*, 38(6), 832-40.

Strommen, D., Nakamoto, K. (1984). *Laboratory Raman Spectroscopy*, John Wiley & Son, New York.

Stutzman, P.E. (2001). "Scanning Electron Microscopy in Concrete Petrography." *Calcium Hydroxide in Concrete*, J. Skalny, J. Gebauer, I. Odler, editor, American Ceramic Society, Westerville, 59-72.

Tarrida, M., Madon, M., Rolland, B.L., Colombet, P. (1995). "An in-situ Raman spectroscopy study of the hydration of Tricalcium silicate." *Advanced Cement Based Materials*, 2(1), 15-20.

Taylor, H.F.W. (1997). *Cement chemistry*, 2nd ed., Thomas Telford, London.

Taylor, R., Richardson, I.G., Brydson, R.M.D. (2010). "Composition and microstructure of 20-year-old ordinary Portland cement-ground granulated blast-furnace slag blends containing 0 to 100% slag." *Cement and Concrete Research*, 40(7), 971-983.

Thomas, J.J., Jennings, H.M., Allen, A.J. (1998). ‘The surface area of cement paste as measured by neutron scattering: evidence for two C-S-H morphologies.’ *Cement and Concrete Research*, 28 (6), 897-905.

Torréns-Martín, D., Fernández-Carrasco, L., Martínez-Ramírez, S. (2013). ‘Hydration of calcium aluminates and calcium sulfoaluminate studied by Raman Spectroscopy.’ *Cement and Concrete Research*, 47, 43-50.

Trezza, M.A. (2007). ‘Hydration study of ordinary Portland cement in the presence of zinc ions.’ *Materials Research*, 10(4), 331-334

Vagenas, N.V., Kontoyannis, C.G. (2003). ‘A methodology for quantitative determination of minor components in minerals based on FT-Raman spectroscopy: The case of calcite in dolomitic marble.’ *Vibrational Spectroscopy*, 32(2), 261-264.

Venkiteela, G., Sun, Z. (2010). ‘In-situ observation of cement particle growth during setting.’ *Cement and Concrete Composites*, 32(3), 211-218.

Williams, E.M., Graham, S.S., Reed, P.A., Rushing, T.S. (2009). ‘Laboratory characterization of Cor-Tuf concrete with and without steel fibers’. ERDC/GSL TR-09-22, US Army Corps of Engineers, Louisville, KY.

WiRE 3.3 [Computer software]. Renishaw, IL, Renishaw plc.

Ylmen, R., Jaglid, U., Steenari, B.M., Panas, I. (2009). ‘Early hydration and setting of Portland cement monitored by IR, SEM, and Vicat technique.’ *Cement and Concrete Research*, 39(5), 433-39.

Ylmen, R., Wadso, L., Panas, I. (2010). "Insights into early age hydration of Portland limestone cement from infrared spectroscopy and isothermal calorimetry." *Cement and Concrete Research*, 40(10), 1541-1546.

Zhang, L., Henson, M.J., Sekulic, S.S. (2005). "Multivariate data analysis for Raman imaging of a model pharmaceutical tablet." *Analytica Chimica Acta*, 545(2), 262-278.

Zingg, A., Holzer L., Kaech, A., Winnefeld, F., Pakusch, J., Becker, S., Gauckler, L. (2008). "The microstructure of dispersed and non-dispersed fresh cement paste – New insight by cryo-microscopy." *Cement and Concrete Research*, 38(4), 522 – 529.

CURRICULUM VITA

FENGJUAN LIU

University of Louisville Department of Civil Engineering 111 W.S. Speed Hall Louisville, KY40292	Office: (502) 852-2307 Cell: (502) 510-4760 Fax: (502) 852-8851 f0liu003@louisville.edu
---	--

Education

<i>University of Louisville</i> , Louisville, KY Ph.D. Candidate, Structural Engineering, Dept. of Civil and Environmental Engineering Advisor: Dr. Zhihui Sun Research Project Funded by National Science Foundation GPA: 3.94/4	Expected Nov. 2014
---	--------------------

<i>Dundee University</i> , Dundee, Scotland, United Kingdom M.S., Concrete Engineering and Environmental Management, Dept. of Civil Engineering Advisor: Dr. Moray D. Newlands GPA: A3 (Academic Distinction)	Aug. 2010
--	-----------

<i>Hohai University</i> , Nanjing, China B.S., Material Science and Engineering, Dept. of Civil Engineering Concentrated on Construction Materials GPA: 4.64/5	June. 2009
---	------------

Research Experience

<i>Graduate Research and Teaching Assistant</i> University of Louisville, Louisville, KY	Jan. 2011 – Present
<ul style="list-style-type: none">• Explored Hydration and Microstructure of Portland Cement Pastes during Setting• Characterized Dehydration Mechanism of Different Gypsums	

<i>M.S. Research</i> Dundee University, Dundee, Scotland, United Kingdom	Sept. 2009 – Aug. 2010
<ul style="list-style-type: none">• Investigating Consistency, Water Demand, and Setting Time of Ternary Cementitious System• Exploring Relationship between Constituents, Compressive Strength, Hydration Degree, and Porosity of Ternary Cementitious Paste and Mortar	

Research Interests

Hydration of Cementitious Materials; Concrete Microstructure; Early-age Material Properties; New Type Cement and Concrete; Numerical Modelling of Concrete Properties

Journal Publications

5. **Liu, F.**, Sun, Z., and Qi, C., “Raman Spectroscopic Study on the Hydration Behaviors of Portland Cement Pastes during Setting,” *ASCE Journal of Materials in Civil Engineering* (In Press), 2014.
4. **Liu, F.**, Sun, Z., and Qi, C., “Raman Spectroscopy Study on Dehydration of Commercial Gypsum at Various Temperatures,” *Cement and Concrete Research* (Under Review), 2014.
3. **Liu, F.**, and Sun, Z. (2013), “Feasibility Study of Using Raman Spectroscopy to Detect Hydration in Wet Paste,” *ACI Materials Journal*, Vol. 110, No. 6, pp. 611-618.
2. **Liu, F.**, and Sun, Z., “Investigating Chemical Distribution and Connection in Paste Microstructure by Raman Mapping,” In Preparation.
1. **Liu, F.**, and Sun, Z., “Using Raman Spectroscopy to Characterize Hydration Process in Different Types of Cement Pastes,” In Preparation.

Technical Presentations

2. “Using Raman Spectroscopy to Characterize Hydration Process in Different Types of Cement Pastes,” (2014), *The Fifth Advances in Cement-based Materials: Characterization, Processing, Modelling and Sensing*, Cookeville, TN, July.
1. “Using Raman Spectroscopy to Characterize the Early-age Behavior of Cement Paste,” (2013), *Conference of the ASCE Engineering Mechanics Institute*, Evanston, IL, Aug.

Other Professional Development Opportunities

5. “Raman Spectroscopy Study on the Early-age Hydration of Cement Pastes,” (2014), Presented in the GEM Grad Lab, University of Louisville, Louisville, KY, Sept.
4. “Using Raman Spectroscopy to Study Early-age Behavior of Cement Pastes,” (2014), Presented to the Industrial Board of Advisor, University of Louisville, Louisville, KY, May.
3. Participant, ACI Convention, 2013, Phoenix, AZ, Oct.
2. Grant Writing Academy Workshop, Spring Semester, 2013
1. Graduate Teaching Academy Workshop, 2012-2013

Teaching Experience

Graduate Teaching Assistant	Jan. 2011
University of Louisville, Louisville, KY	– Dec. 2013
<ul style="list-style-type: none">• Assisted in Teaching Four Undergraduate Courses in Size of 30 – 40 Students. Topics included: Construction Materials, Structural Analysis, Steel Design, and Statics• Prepared Course Materials including Laboratory Experiments, Lectures, Exams, and Homework• Supervised Students in Exams. Graded Exams, Quizzes, and Weekly Homework	

Graduate Courses

Construction Materials, Concrete: Sustainable use and Environmental Impact Assessment, Advanced Thermodynamics (Chemical Engineering), Advanced Mechanics of Solids, Green Engineering and Sustainable Design, Non-destructive Testing, Concrete: Design for Durability, Assessment and Repair, Concrete Construction I and II, Pavement Design, Health and Safety and Environmental Management, Experimental Stress Analysis (Mechanical Engineering), Fiber Reinforced Composites Materials (Mechanical Engineering), Data Acquisition and Analysis (Mechanical Engineering), Material Characterization (Chemical Engineering, Sit-in), Engineering Project Fundamentals I (Chemical Engineering, Sit-in)

Scholarship and Honors

6. Graduate School Diversity Research Grant for Graduate Students, University of Louisville, KY, 2013
 5. Excellent Grant, University of Dundee, Dundee, Scotland, United Kingdom, 2010
 4. National Endeavor Fellowship, Hohai University, Nanjing, China, 2008
 3. Outstanding Academic Scholarship, Hohai University, Nanjing, China, 2005 – 2009
 2. Spiritual Civilization Scholarship, Hohai University, Nanjing, China, 2005 – 2007
 1. Third Place in the *National English Contest for College Students*, Hohai University, Nanjing, China, 2006.
-

Current Membership

4. American Society of Civil Engineers (ASCE)
 3. American Concrete Institute (ACI)
 2. The American Ceramic Society (ACerS)
 1. Kentucky Academic of Science (KAS)
-